ADVANCED LECTURES 1986

PARAMETRIZATION OF PHYSICAL

PROCESSES IN ATMOSPHERE

AND

OCEAN MODELS

VOL 2

DR H CATTLE

Acknowledgements

I am grateful to a number of individuals for assistance in preparing these lectures and in particular to David Carson for taking on lectures 2 and 3. I am also grateful to Rod Smith for suggestions and material for lecture 4; to Chris Gordon for allowing me to use material from his unpublished paper on mixed layer modelling for lectures 5 and 6 and to David Gregory for suggestions for material for lecture 8, as well as to the various referenced authors from whom material has been taken.

H. Cattle

Met O 20

.nj

Advanced Lecture 6

Parametrization of the oceanic mixed layer

6.1 Introduction

It was noted previously that, to date, large scale models of the ocean employ only the simplest approach to parametrization of the oceanic boundary layer, often treating the uppermost layer of the model ocean as a constant depth mixed layer into which the fluxes of heat, moisture and momentum pass directly to increment the layer temperature, θ, salinity, S, and velocity, $\underset{\sim}{V}$ by:

$$\left.\frac{\Delta\theta}{\Delta t}\right|_{SF} = \frac{Q_N}{\rho c_p \Delta z_1} \quad ; \quad \left.\frac{\Delta S}{\Delta t}\right|_{SF} \approx \frac{(P-E)S}{\Delta z_1} \quad ; \quad \left.\frac{\Delta \underset{\sim}{V}}{\Delta t}\right|_{SF} + f\underset{\sim}{k}\times\Delta\underset{\sim}{V}\bigg|_{SF} = \frac{\tau_0}{\rho\Delta z_1} \quad (6.1)$$

where ρ is the water density and c_p the specific heat for the layer, Δz_1 is its thickness (usually of order 50m). Q_N represents the net heating of the ocean surface i.e. the sum of the sensible and latent heat fluxes and the net radiative flux there. E is evaporation and P the precipitation, so P–E is the net water flux at the surface. From this layer the fluxes are communicated to the deeper layers of the model ocean via convective adjustment (through instability between layers) or (relatively slowly) through vertical diffusion and advection. As described in Lecture 4, improvements to the representation of the oceanic boundary layer via turbulence closure schemes with Richardson number dependent diffusion coefficients are beginning to be implemented. However, the application of explicit mixed layer models embedded into ocean GCM structures is, as yet, only a slowly evolving field of research. To date such embedded models have been run by Adamec et al. (1981) in the context of the simulation of the ocean's response to forcing from a hurricane, and globally by Kim and Gates (1980).In addition, mixed layer models have, themselves, been run in coupled mode with atmospheric models (e.g. Wells, 1979). That is not to say, however, that a variety of ocean mixed layer models is not available and we shall discuss some aspects of these below. Before doing so, it is of some interest to look at the response of the near surface ocean currents to changes in the imposed wind stress and the generation of vertical motion at the base of the mixed layer associated with horizontal variations in the wind stress field. We do this in the context of the vertically integrated momentum equation.

6.2 A bulk model of the Ekman layer of the ocean

We have previously derived the vertically integrated momentum equation as (lecture 5, equation (5.12)):

$$h\frac{D\underset{\sim}{V_M}}{Dt} + hf\underset{\sim}{k}\times\underset{\sim}{V_M} + \frac{h}{\rho}\nabla p_M = \frac{\tau_0}{\rho} - w_e\Delta\underset{\sim}{V} \quad (6.2)$$

where $\underset{\sim}{V_M}$ is the mean current through the layer. This equation can also be applied to the oceanic mixed layer, taking depth as the vertical coordinate (positive downwards). If we now assume that the horizontal advection terms can be neglected (probably a good approximation over large horizontal scales in the open ocean) and write $\underset{\sim}{V_M} = \underset{\sim}{V_G} + \underset{\sim}{V_E}$ where $\underset{\sim}{V_G}$ satisfies:

$$\frac{\partial V_G}{\partial t} + F \underset{\sim}{k} \times \underset{\sim}{V_G} = -\frac{1}{\rho} \nabla P_M \qquad (6.3)$$

and assume $\underset{\sim}{V} = V_G$ below the mixed layer, then it follows that the vertically integrated "Ekman part" of the mean current satisfies:

$$h \frac{\partial V_E}{\partial t} + h f \underset{\sim}{k} \times \underset{\sim}{V_E} = \frac{\tau_0}{\rho} + w_e \underset{\sim}{V_E} = \frac{\tau_0}{\rho} + \left(w_h - \frac{\partial h}{\partial t} \right) \underset{\sim}{V_E} \qquad (6.4)$$

Scale analysis indicates the term $w_h \underset{\sim}{V_e}$ to be an order of magnitude or so smaller than τ_0/ρ. If we neglect this term, therefore, then:

$$\frac{\partial (h V_E)}{\partial t} + f \underset{\sim}{k} \times (h \underset{\sim}{V_E}) = \frac{\tau_0}{\rho} \qquad (6.5)$$

Thus, at equilibrium ($\partial /\partial t = 0$):

$$\underset{\sim}{V_E} = \frac{1}{\rho f h} \underset{\sim}{k} \times \tau_0 \qquad (6.6)$$

The direction of $\underset{\sim}{V_E}$ in relation to τ_0 is dependent on the sign of the Coriolis parameter, f, so that there is a net integrated transport to the right of the wind in the northern hemisphere and to the left in the southern hemisphere. Substitution of the expression for $\underset{\sim}{V_E}$ into the vertically integrated continuity equation:

$$w_h = h \nabla \cdot \underset{\sim}{V_M} \qquad (6.7)$$

then gives, if horizontal gradients of h and ρ are neglected:

$$w_h = \frac{1}{\rho f} \text{curl } \tau_0 + \frac{\beta}{\rho f^2} \tau_{0x} \qquad (6.8)$$

where β is the variation of Coriolis parameter with latitude and τ_{0x} is the west-east component of the surface stress. The last term makes the largest contribution close to the equator, so that for higher latitudes, a component of the vertical motion at the base of the mixed layer is generated by the curl of the wind stress. These results are illustrated by results from a barotropic integration of the Bryan/Semtner ocean model, forced by the annual mean wind stress, in Figure 6.1.

Note that derivation of the profile of the current through the layer, by integration of the stationary, horizontally homogeneous form of the basic momentum equation with a flux-gradient relationship used to parametrize the turbulent flux through the layer, leads, if constant diffusion coefficients are used, to the familiar "Ekman spiral" solution in which the surface current is at 45° to the direction of the wind stress. The model results shown in Figure 6.1 essentially represent the integrated Ekman current, which lies at 90° to the wind stress. Care must be taken in comparison of such model results with observed surface current data, therefore.

For general, time dependent, wind forcing, it is necessary to solve equation (6.5) in full. As a simple illustration we consider the

solution for a constant wind stress which is switched on at time t = 0. In a crude sense this may be taken to represent the onset of a storm. The solution in this case is found to be:

$$u_E = \frac{\tau_o}{\rho f h} \sin ft$$

$$v_E = -\frac{\tau_o}{\rho f h} (1 - \cos ft)$$

(6.9)

where u_E and v_E are the components of the Ekman current $\underset{\sim}{V}_E$. The response, therefore consists of an Ekman transport at right angles to the wind, plus an inertial oscillation of amplitude equal to the constant transport (Figure 6.2). Once the inertial oscillation has been generated by the sudden wind change, the solution (6.9) implies that it remains for all time. In the real ocean, these oscillations decay in time. The precise mechanism by which this takes place is uncertain, although the most likely process is removal of energy from the mixed layer by the radiation of internal waves (Bell, 1978). In large scale ocean models, it is the presence of large scale horizontal diffusion terms in the model equations which act to damp the oscillations (Figure 6.3). Pollard and Millard (1970) have compared the response of a model, based on modifying (6.5) by addition of a damping term $-\mu \underset{\sim}{V}_E$ to its rhs, when forced by observed winds, with the response of the real ocean. Figure 6.4 shows their results for a damping coefficient, μ, of 4 days^{-1}. Wind forcing, observed currents at 12m and modelled currents are shown in the diagram. The model works particularly well just after sudden wind changes. Such motions provide a means whereby shear generated turbulence, and hence entrainment, may be induced at the base of the mixed layer.

6.3 Bulk models of the ocean mixed layer: general discussion

In the last lecture, we derived a set of equations for the mixed layer of the atmosphere. With minor adjustment, these can be adapted to apply to the oceanic case also, much as we have done above for the Ekman layer. Thus with depth, again, as the z coordinate (increasing downwards) and assuming a linear equation of state of the form $\rho = \rho_o(1 - \alpha\theta)$, where α is the coefficient of thermal expansion of sea water, then, for the profiles of Figure 6.5, the oceanic mixed layer equations can be written as:

$$h \frac{D\theta_m}{Dt} = \frac{Q}{\rho c_p} - w_e \Delta\theta + \frac{S(o) - S(h)}{\rho c_p}$$

(6.10)

$$h \frac{D\underset{\sim}{V}_m}{Dt} + hf\underset{\sim}{k} \times \underset{\sim}{V}_m + \frac{h}{\rho}\nabla p_m = \frac{\tau_o}{\rho} - w_e \Delta\underset{\sim}{V}$$

(6.11)

$$w_h = h(\nabla \cdot \underset{\sim}{V}_m)$$

(6.12)

$$\frac{Dh}{Dt} = w_h - w_e$$

(6.13)

$$w_e \Delta e = -\tfrac{1}{2} h \alpha \rho_o g \left(\frac{Q}{\rho c_p} + w_e \Delta \theta \right) + \lambda \rho u_*^3 - \tfrac{1}{2} \rho w_e \left| \Delta \underset{\sim}{V} \right|^2 - D - P_s \qquad (6.14)$$

where:

$$\Delta e = e_B - e_M$$
$$\Delta \theta = \theta_B - \theta_M \qquad\qquad\qquad (6.15)$$
$$\Delta \underset{\sim}{V} = \underset{\sim}{V_B} - V_M$$

For simplicity, the equation for salinity changes has been omitted.
Parameters with subscript B represent values below the oceanic mixed
layer. In the above, Q now represents the net heating of the sea
surface. That is it is the sum of the net longwave radiation and the
sensible and latent heat fluxes there. The layer is also heated
differentially by the penetration of solar radiation and its
absorption with depth. This introduces the term involving S(0)-S(h)
into the heat conservation equation and a term P_s into the TKE
equation where:

$$P_s = \tfrac{1}{2} h \frac{(S(0) + S(h))}{\rho c_p} + \frac{1}{\rho c_p} \int_0^h S(z)\,dz \qquad (6.16)$$

S(0) is the downwards shortwave flux entering the ocean surface and
S(z) its value at level z . $(\tau_o = \rho u_*^2$ is the stress of the air on the sea
surface. Because of the choice of coordinate system, vertical motion
is negative towards the surface. Thus w_e negative means that the layer
is entraining fluid from below, contributing to deepening. Note also
that the buoyancy term has a negative sign in front. Surface heating
leads to the stabilization of the layer and loss of TKE, as does
entrainment of the cooler water from below at the thermocline. The
characteristics of several mixed layer models can be illustrated by
further simplification of these equations. To do this we first ignore
the effects of horizontal advection and large scale vertical motion
and replace the momentum equation by (6.5). We also, neglect the $w_e \Delta e$
term in the TKE equation and, for the present, the absorption of
solar radiation with depth, replacing Q by Q_N, therefore. If we also
consider the stabilising case only, and set the dissipation term in
the TKE equation proportional to the shear production terms, we obtain
the simplified set of equations:

$$h \frac{\partial \theta_M}{\partial t} = \frac{Q_N}{\rho c_p} - w_e \Delta \theta \qquad\qquad (6.17)$$

$$h \frac{\partial V_E}{\partial t} + h f \underset{\sim}{k} \times \underset{\sim}{V_E} = \frac{\tau_o}{\rho} + w_e \underset{\sim}{V_e} \qquad\qquad (6.18)$$

$$\frac{\partial h}{\partial t} = - w_e \qquad\qquad (6.19)$$

$$\tfrac{1}{2} h \alpha \rho_o g \left(\frac{Q}{\rho c_p} + w_e \Delta \theta \right) = \tfrac{1}{2} \lambda_s \rho w_e \underset{\sim}{V_E}^2 + \lambda_m \rho u_*^3 \qquad (6.20)$$

where:

$$\Delta \theta = \theta_B - \theta_M \qquad\qquad (6.21)$$

Equations (6.17) to (6.20) must be solved for the prognostic variables V_E, θ, w_e and h. Numerical methods are necessary to solve this system for realistic wind and heat flux forcing. The model outlined above is, in essence, that of Niiler (1975) in all its important aspects. Earlier models are obtained by giving particular emphasis to either of the two production terms in (6.20). Thus Kraus and Turner (1967) ignored the shear production term, only retaining the surface generation of TKE via the windmixing $\lambda_m \rho u_*^3$. Pollard, Rhines and Thompson (1973) on the other hand included only the shear production term, $\frac{1}{2}\lambda_s \rho w_e V_E^2$. Niiler (1975) and de Szoeke and Rhines (1976) showed that each of these models can adequately describe the physical process of mixed layer deepening only for restricted timescales.

6.4 Model behaviour for idealised forcing

Figure 6.6 shows results from a numerical integration of the above model equations for which the heat flux, Q_N, was set to zero and a small value of the friction velocity of 1 cm s^{-1} was applied at time t = 0. $\Delta\theta$ was initially set to 2C and the initial depth of the mixed layer to 5m. Figure 6.6a shows the contribution to the energy generation from the shear production and windmixing terms in the TKE equation. The windmixing contribution is constant since u_* is fixed. The shear contribution peaks after about 5 hours. Referring back to equation (6.9), it will be seen that a maximum is implied by the (1-cosft) term at t = π/f (which is about 12 hours for f = 10^{-4}). This simply illustrates how the shear generation falls of as the mixed layer depth increases. As noted by Niiler (1975) and de Szoeke and Rhines (1976), it is evident that the shear production term is only important for a time duration of order the inertial period after the occurence of a sudden change in the wind. Over longer timescales, this contribution falls to zero and the windmixing dominates.

Figure 6.6b shows the corresponding variation in mixed layer depth. The initial deepening due to shear production is rapid but subsequently the depth increases linearly. The latter reflects the influence of the windmixing, once the shear production at the base of the mixed layer has become negligible. The dotted line in Figure 6.6b illustrates the mixed layer evolution if shear production of turbulence is totally neglected. When starting from a shallow mixed layer depth, therefore, a Kraus-Turner type model (which only takes the windmixing into account) underestimates the mixed layer depth at all times. However, if the initial mixed layer depth is sufficiently large, the contribution from the shear production will also be negligible at all times. This is because the currents generated in the mixed layer, and therefore the shear at the mixed layer base, are inversly proportional to the depth of the layer. Figure 6.6c illustrates the mixed layer depth as a function of time starting from an initial depth of 20m, still with both turbulent production mechanisms included. It shows that the shear production is indeed negligible in this case. However, a word of warning should be given regarding the general applicability of this last result in that the value of u_* used here is rather small. It can be shown that the mixing associated with shear production alone reaches to depths proportional to u_*/f, so that during storm mixing this process can be important to much greater depths than those demonstrated above.

In the above, the effects of surface heating were omitted from the numerical solution and the result of the windmixing was to

continually deepen the layer. If a constant surface heat flux is imposed on the layer, the windmixing energy must go into mixing this heat downwards. In this case it follows from the turbulent energy equation (with $w_e = -\partial h/\partial t$) that, omitting the shear production terms at the mixed layer base from consideration, $\partial h/\partial t = 0$ when:

$$h \simeq \frac{2\lambda_M c_p \rho u_*^3}{\alpha g Q_N} \qquad (6.22)$$

i.e. the effect of the surface heating is to restrict the depth to which the layer can penetrate.

6.5 Mixed layer shallowing

It is, of course possible that there is insufficient mixing energy available for a given positive heat flux to mix the heat input at the top of the layer throughout the existing mixed layer. When this is so, the TKE equation (6.20) implies a negative rate of entrainment (w_e positive) into the layer. In this case, most existing ocean mixed layer models set $\partial h/\partial t = 0$ and assume that the layer will shallow to a depth of the form of (6.22) above. Note that this expression is akin to that for the Monin-Obukhov depth for the atmosphere. This is in contrast to the assumptions sometimes made in treating the shallowing case for the atmospheric mixed layer, for which, for example, an appropriate equilibrium depth is suggested to be (Driedonks, 1986):

$$h_A \sim 0.4 \left(\frac{u_* L}{f} \right) \qquad (6.23)$$

where L is the Monin-Obukhov length.

6.6 Deepening due to surface cooling

In the applications above, a zero or positive heat flux was assumed at the sea surface, so that any deepening of the mixed layer must be wind induced. Consider now the situation in which the wind is zero, but there is a net cooling at the surface (e.g. a clear, calm night). In this case, the integrated TKE equation becomes:

$$\frac{1}{2} h \alpha \rho_o g \left(\frac{Q_N}{\rho c_p} + w_e \Delta\theta \right) = -D \qquad (6.24)$$

where we have reintroduced the dissipation term, D. Q_N is negative when there is cooling from the surface, which means that there is a production of turbulent kinetic energy due to convective overturning. If D=0, then the reduction of the potential energy of the water column due to cooling is equal to the increase in potential energy due to penetrative mixing. In other words, the effect of the cooling is to deepen the layer at a rate given by:

$$w_e = -\frac{\partial h}{\partial t} = -\frac{Q_N}{\rho c_p \Delta\theta} \qquad (6.25)$$

In this case, the convection is said to be fully penetrative. In general, some of the energy generated by convective overturning will be dissipated. Following Gill and Turner (1975), and setting the dissipation term proportional to the generation term allows the D

term in (6.24) to be combined with the "Q" term to give:

$$W_e \Delta\theta = -\frac{\sigma_3 Q_N}{\rho q \Delta\theta} \qquad (6.26)$$

From field experiments under sea ice, Farmer (1975) found σ_3 to be of order 0.15, which implies that most of the convectively generated turbulent energy is dissipated within the mixed layer.

6.7 The effects of penetrative short wave radiation

Up to now, the effects of penetrative short wave radiation have been neglected. We shall now consider some aspects of this. In general, the surface heat flux, Q, (equation (6.10) will be negative since it is the sum of the latent, sensible and net infra-red fluxes at the surface. The short wave flux is always positive, and, since it is absorbed below the surface, convective overturning must occur at the top · of the mixed layer due to the destabilising effect of a surface heat loss. This will even be the case when there is a net heat input into the mixed layer. The depth over which convection will occur can be found by equating the surface heat loss with the integrated heating over this depth due to the penetrative radiation. For depths less than this, the water will be cooling and hence unstable. Paulson and Simpson (1977) have published double exponential fits of the decay of solar radiation with depth for various water types. For example for "type II" water masses, appropriate to the northeast Pacific (near OWS P) the decay function is given by:

$$S(z) = S(0)\left(R e^{z/d_1} + (1-R) e^{z/d_2}\right) \qquad (6.27)$$

where R=0.77, d_1=1.5m and d_2=14m. In this area typical July values of the heat flux components are S(0)=120Wm^{-2} and Q=-50Wm^{-2}(Esbensen and Kushnir, 1981). Since $d_2 \gg d_1$ it is reasonable to drop the second term in (6.27) in which case the penetration depth for convective overturning is given by:

$$D_s = d_1 \ln \frac{1}{R}\left(1 + \frac{Q}{S(0)}\right) \qquad (6.28)$$

and, with values for the various parameters as above is found to equal some 0.5m. This value is much smaller than the value for the minimum depth of the mixed layer used in climate studies (Mitchell, 1977). Note that, if the detailed effect of the penetration of solar radiation with depth is required to be modelled, as well as the effects when deepening takes place of the structure of the profile left behind during shallowing of a previously deeper mixed layer, it is necessary to depart somewhat from the "bulk" approach above and to go to multilayer mixed layer models in which the heating is progressively mixed down from layer to layer until there is no more turbulent energy left to carry it further down (see Thompson, 1976), or to a multilayer model which uses the "turbulence closure" approach.

It has been emphasised by Woods (1980) that the depth D_s has a strong diurnal signal since S(0) varies markedly throughout the day. Thus at night, (6.28) implies an infinite value of D_s. This is, in fact, unrealistic since at night the diurnal thermocline built up during daylight hours must first be eroded before deepening into the seasonal thermocline can take place. Detailed studies with high resolution versions of the layer type models still need to be carried

out to investigate the importance of the diurnal cycle in more detail.

6.8 Simulation of the oceanic response during MILE

We conclude by briefly describing a model simulation of mixed layer characteristics, compared to those observed during the so-called MIxed Layer Experiment (MILE). The simulation was carried out by Davis, de Szoeke and Niiler (1981) using a mixed layer model of essentially the same form as that described above. Figure 6.7 shows a series of simulations of sea surface temperature and mixed layer depths using forcing fluxes derived from detailed observations during the experiment. Figure 6.7a is their "best fit" simulation in which $\lambda_m = 0.39$ and $\lambda_s = 0.48$. The model reproduces well both the sea surface temperatures and the mixed layer depths.

Figures 6.7b and 6.7c show their two extreme sensitivity simulations with, in 6.7b, $\lambda_s = 0.67$, $\lambda_M = 0.13$ and, in 6.7c, $\lambda_s = 0$, $\lambda_M = 0.69$. When λ_s is increased at the expense of λ_M, which is equivalent to putting more emphasis on shear production rather than surface windmixing, the response immediately following the storm on 21-22 August is still reproduced well, whereas, during the period of light winds which follows, the mixed layer shallows unrealisically, leading to sea surface temperatures which are far too high. Conversely, increasing λ_M at the expense of λ_s (Figure 6.7c) also downgrades the simulation, particularly after sudden wind changes when the response is too slow. However, this latter case gives an overall better simulation than that shown in Figure 6.7b. These results are clearly consistent with the considerations discussed above in the context of idealised forcing.

****

.nj

Advanced Lecture 6-References

Adamec, D., R.L.Elsberry, R.W.Garwood,Jr. and R.L.Haney, 1981, An
embedded mixed layer-ocean circulation model. Dyn. Oceans and Atmos.,
6, pp 69-96.

Bell, T.H., 1978, Radiation damping of inertial oscillations in the
upper ocean. J.Fluid Mech., 88, pp 289-308.

Davis, R.E., R.de Szoeke and P.Niiler, 1981, Variability in the upper
ocean during MILE. Part II: Modelling the mixed layer response.
Deep-Sea Res. 28A, pp 1453-1475.

de Szoeke, R.A. and P.B.Rhines, 1976, Asymptotic regimes in mixed
layer deepening. J.Mar. Res. 34, pp 111-116.

Driedonks, A.G.M., 1986, Bulk boundary layer regimes. Vol. 1, Seminar
on physical parametrization for numerical models of the atmosphere,
ECMWF.

Esbensen, F.K. and Y Kushnir, 1981,The heat budget of the global
ocean: An atlas based on estimates from surface marine observations.
Report No. 29, Climatic Res. Inst., Oregon State Univ., Corvallis.

Farmer, D.M., 1975, Penetrative convection in the absence of mean
shear. Q.J.R.Met.Soc., 101, pp 869-891.

Gill, A.E. and J.S.Turner, 1976, A comparison of seasonal thermocline
models with observation. Deep-Sea Res., 23, pp 391-401.

Kim, J-W. and W.L.Gates, Simulation of the seasonal fluctuation of the
upper ocean by a global circulation model with an embedded mixed
layer. Report No. 11, Clim. Res. Inst., Oregon State Univ., Corvallis.

Kraus, E.B. and J.S.Turner, 1967, A one-dimensional model of the
seasonal thermocline, II: The general theory and its consequences.
Tellus, 19, pp 98-106.

Mitchell, J.F.B., 1977, An oceanic mixed layer model for use in
general circulation models. Met. O 20 Tech. Note. II/85.

Niiler, P.P., 1975, Deepening of the wind mixed layer. J.Mar. Res.,
33, pp 405-422.

Paulson, C.A. and J.J.Simpson, 1977, Irradiance measurements in the
upper ocean. J.Phys. Oceanog., 7, pp 952-956.

Pollard, R.T. and R.C.Millard, 1970, Comparison between observed and
simulated wind generated inertial oscillations. Deep-Sea Res., 17, pp
813-821.

Pollard, R.T., P.B.Rhines and R.O.R.Y.Thompson, 1973, The deepening of
the wind mixed layer. Geophys. Fluid Dyn., 3, pp 381-404.

Thompson, R.O.R.Y., 1976, Climatological numerical models of the
surface mixed layer of the ocean. J.Phys. Oceanog., 6, pp 496-503.

Wells, N.C., 1979, A coupled ocean-atmosphere experiment; the ocean
response. Q.J.R.Met. Soc., 105, pp 355-370.

Woods, J.D., 1980, Diurnal and seasonal variation of convection in the wind mixed layer of the ocean. Q.J.R.Met. Soc., 106, pp 379-394.

Woods, J.D., 1980, Diurnal and seasonal variation of convection in the wind mixed layer of the ocean. Q.J.R.Met. Soc., 106, pp 379-394.

(b)

(a)
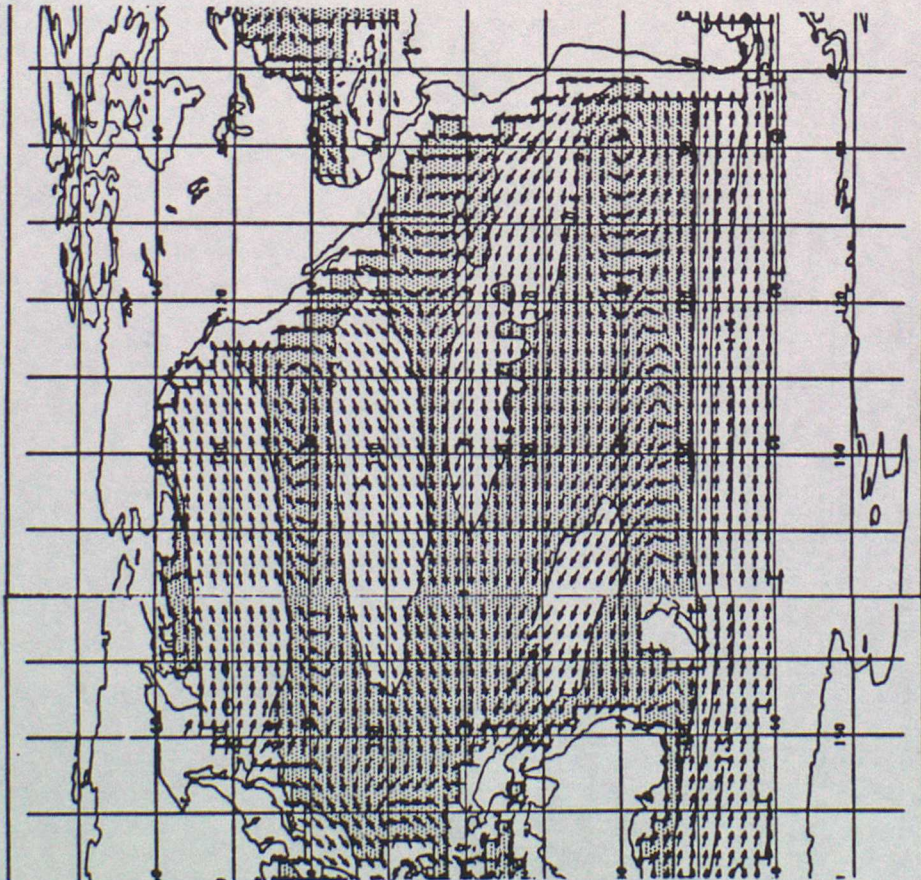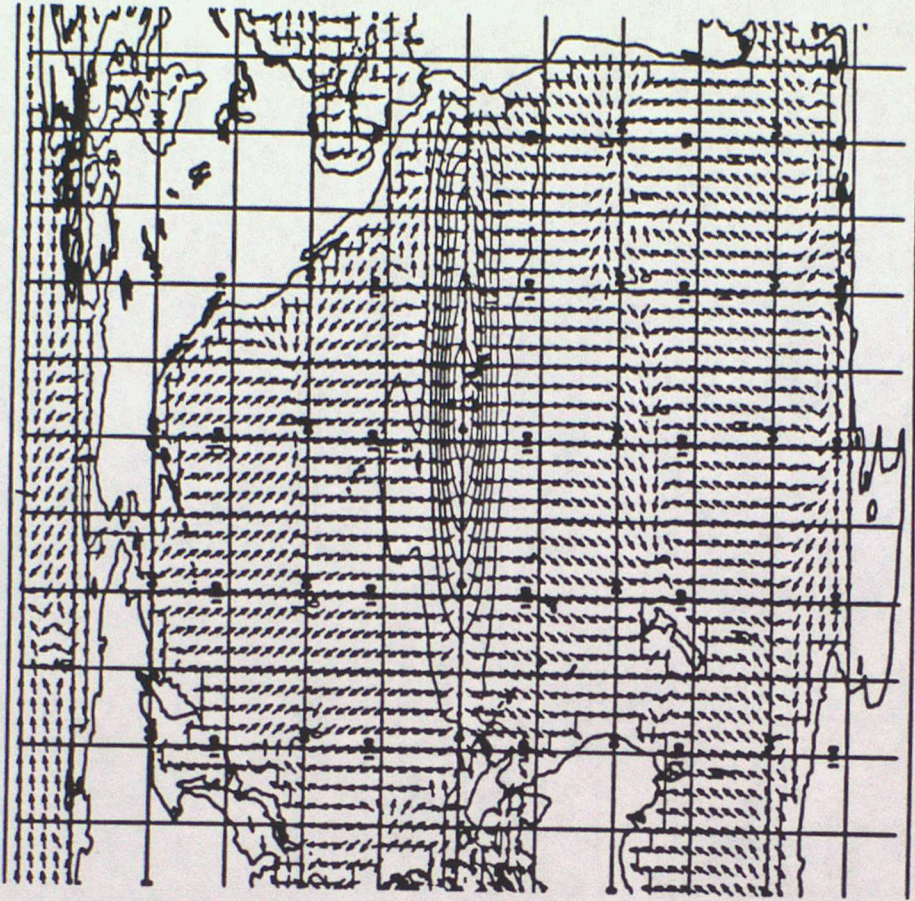
Figure 6.1 Results for the central Pacific from a 30 day barotropic
integration of the Bryan/Semtner ocean model showing (a) the imposed
annual mean wind stress; (b) the 50m deep surface layer velocity field
(isotachs and direction arrows); (c) the curl of the wind stress and
(d) the vertical motion at 50m depth: regions of downwelling are shown
shaded.

(d)
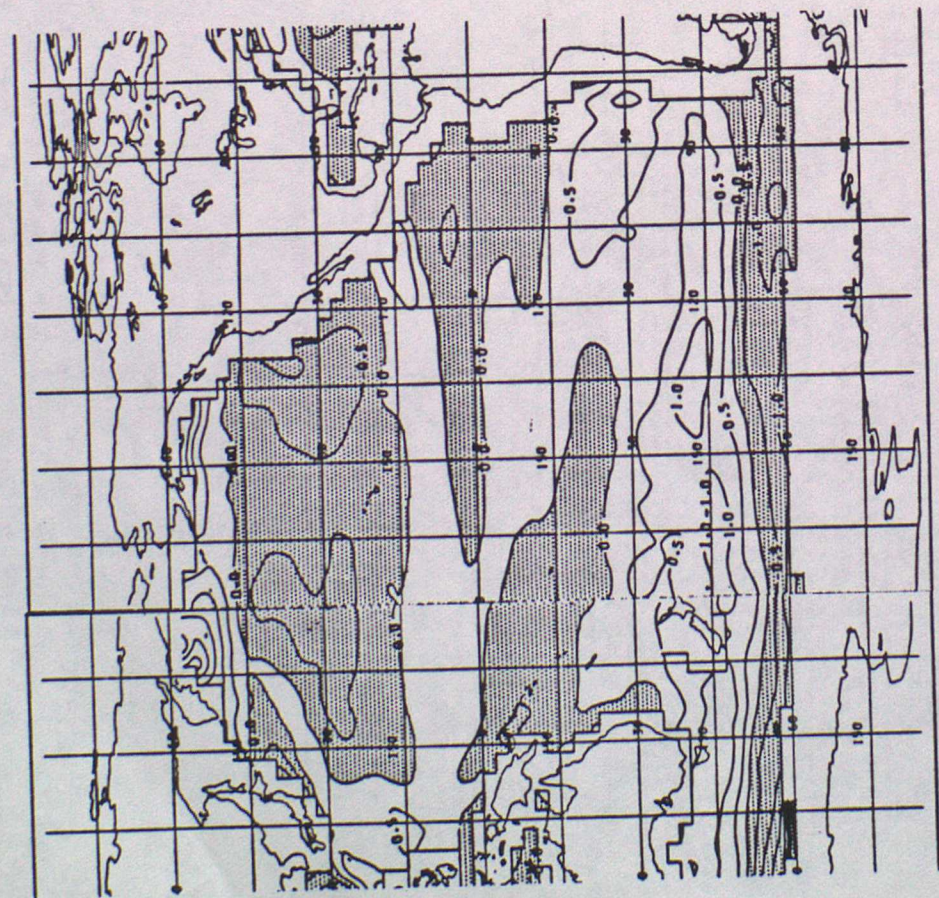
(c)

Figure 6.1 (continued)
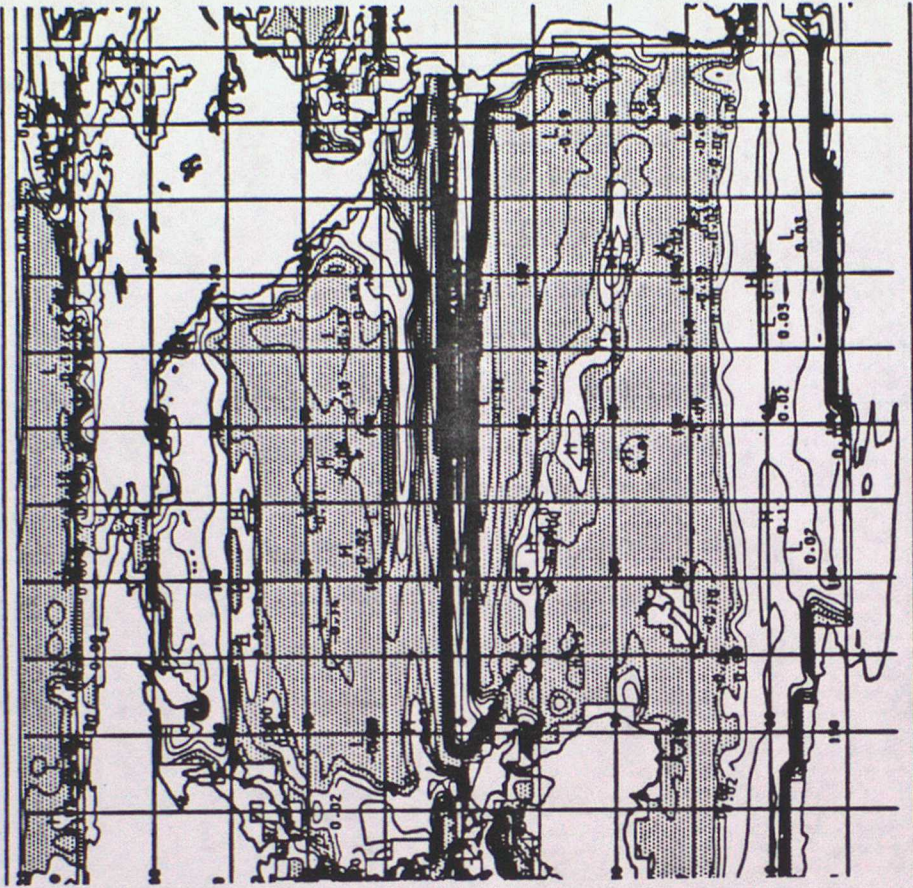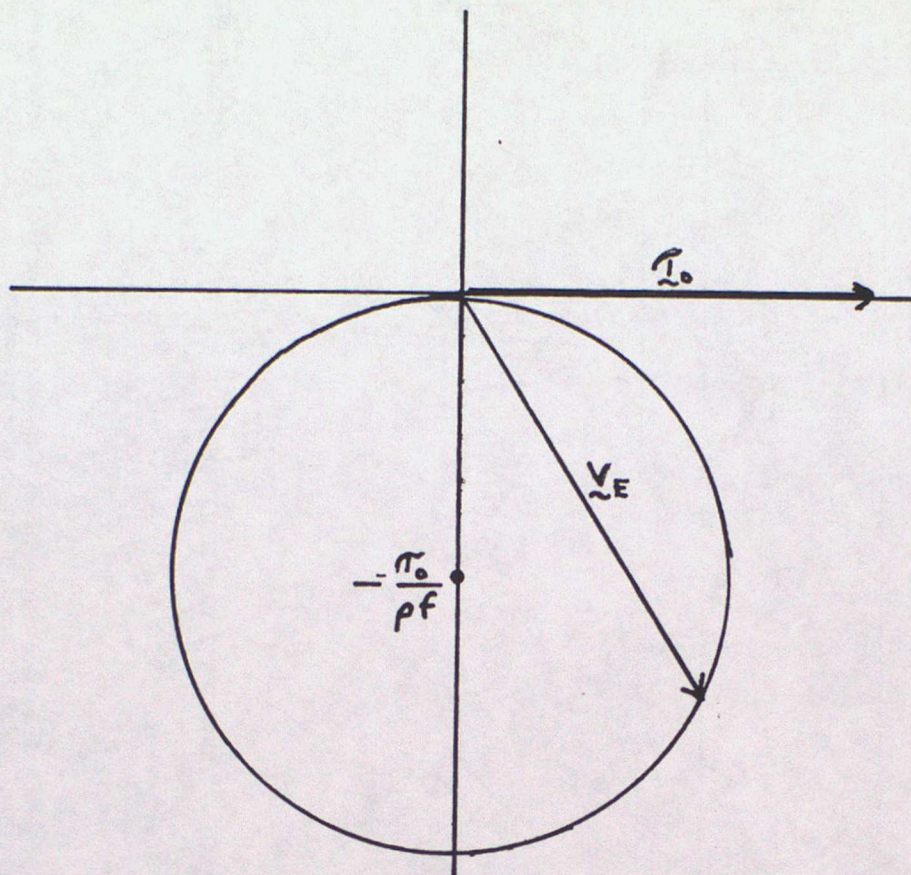
Figure 6.2 Locus traced out by the current vector, V_E, according to equation (6.9).
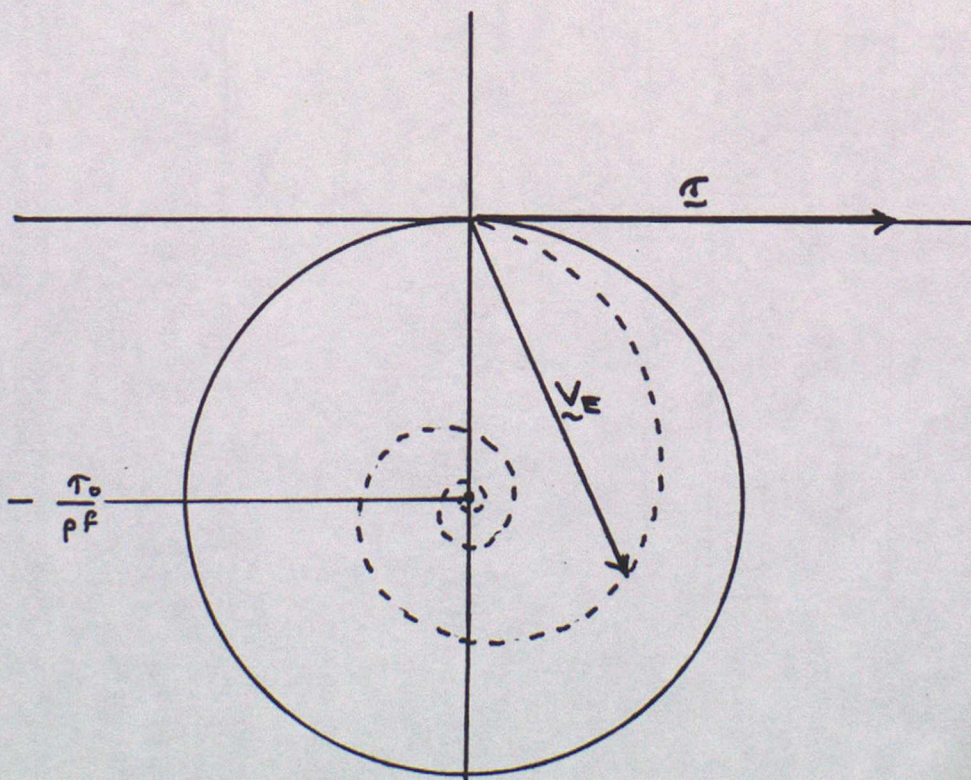

Figure 6.3 Locus traced out by the solution to equation (6.5) when a damping term, μV_E, is added. The dotted spiral indicates that the inertial oscillation decays with time.
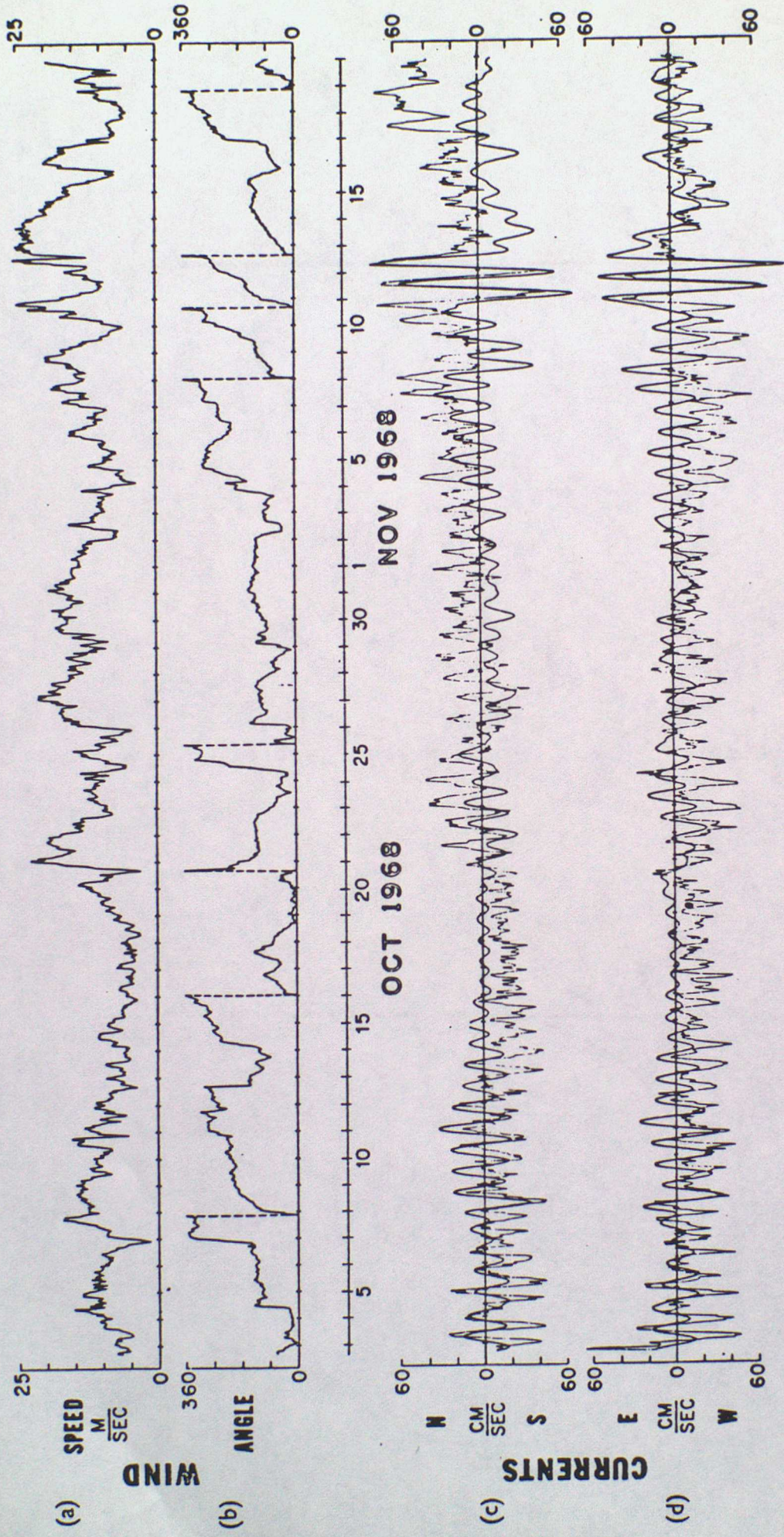
Mooring 280. One-hour averages of (a) wind speed; (b) direction towards which wind blows (measured clockwise from north); (c) North-south components of the model with a 4-day damping (smooth, thick curve) and the observed current 2803 at 12 m deep (jagged, thin curve); (d) East-west components.

Figure 6.4 From Pollard and Millard (1970)
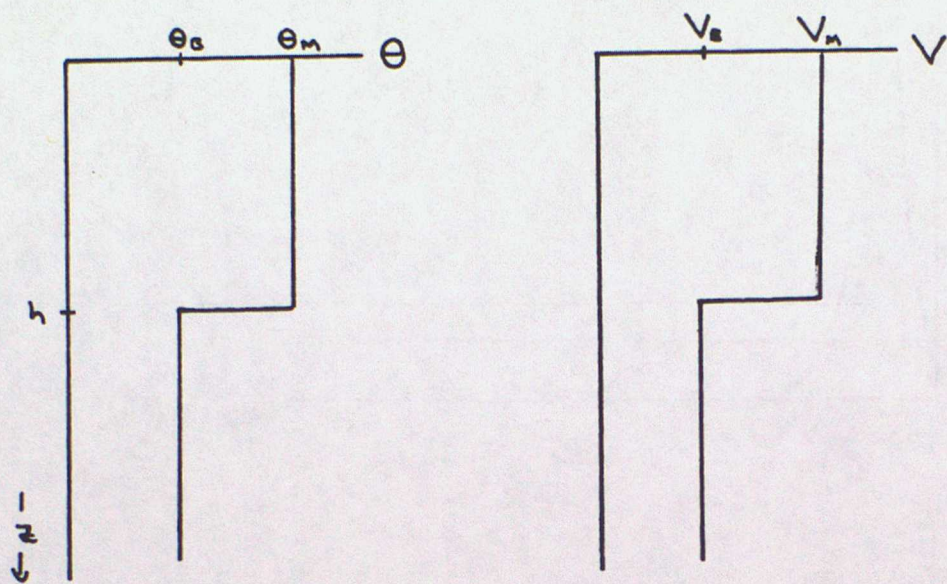
Figure 6.5 Idealised profiles for the oceanic mixed layer.
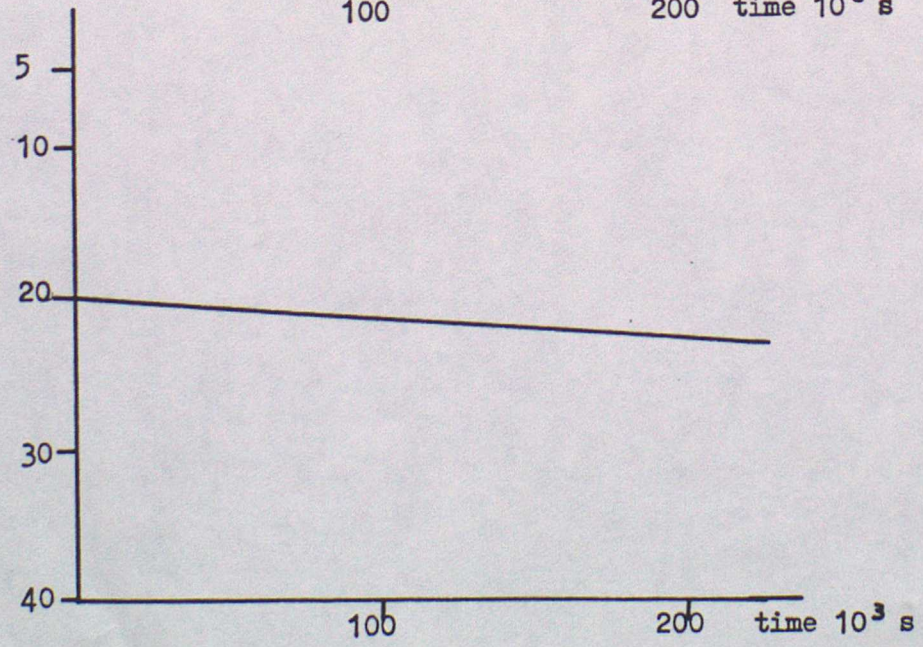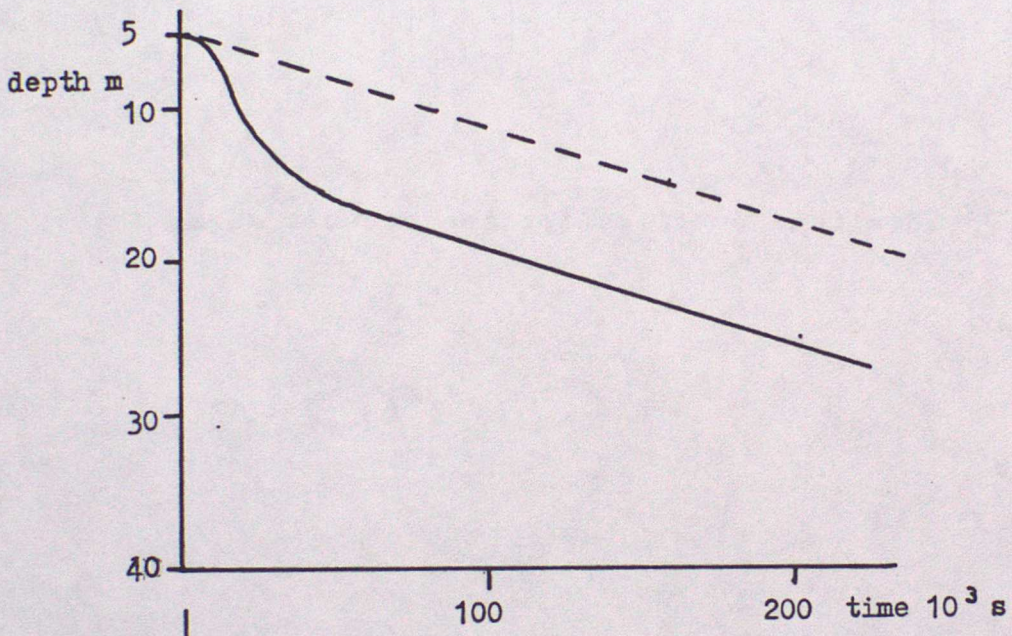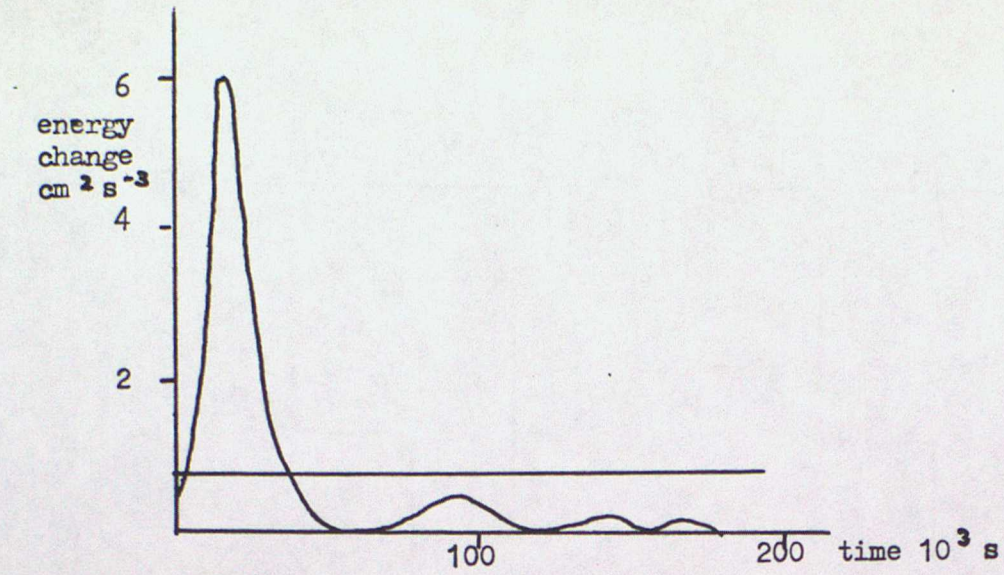
Figure 6.6 Results from an integration of the mixed layer equations.
For an explanation, see text (section 6.3).
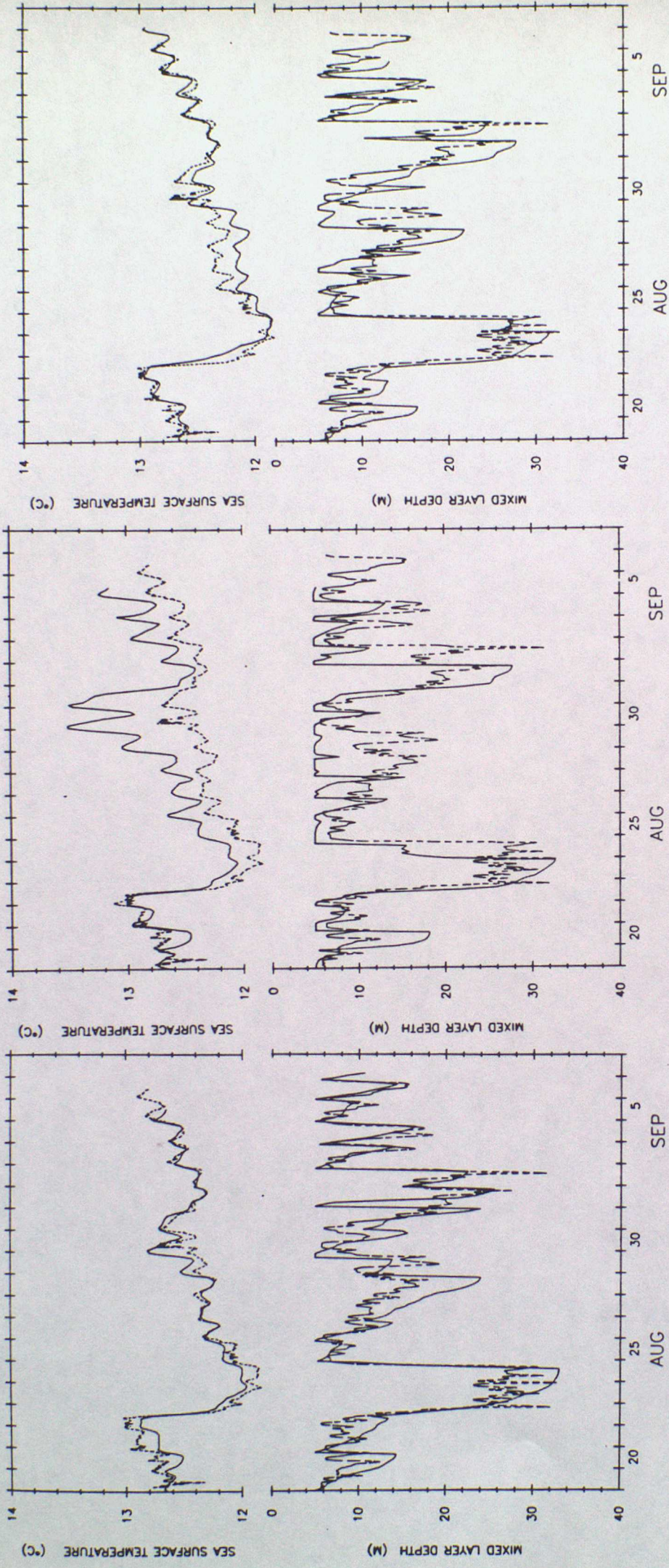
Figure 6.7 From Davis, de Szoeke and Niiler (1981). Comparison of modelled (solid lines) and observed results (dashed). For further explanation, see text (section 6.8).

.nj

Advanced Lecture 7

The Parametrization of Cloud and Liquid Water in Numerical Models

7.1 Introduction

The parametrization of cloud in atmospheric models is important for a number of reasons. Cloudiness is, in itself, a meteorological product of practical importance, especially for the general public, for whom cloudiness and sunshine forecasts are of considerable interest, whilst prediction of low level cloud is important for low level flying operations, for example. There is also some evidence that the impact of cloud cover on the quality of the forecast through its interaction with the radiative fluxes may not be negligible, at least for medium range forecasting (Geleyn, 1981; Slingo,J.M., 1984) In this context also, the representation of the diurnal variation of tropical cloudiness, particularly over land, may also have an impact, not least because it may have an influence on the mid-latitude flow on timescales as short as 10 days or so (Slingo,J.M., 1985). In the climate modelling context, correct representation of cloudiness is particularly important because of the various feedbacks which can occur in the climate system. Here, the need is not only for a reasonable representation of cloudiness in relation to individual synoptic features, but also for a good simulation of the features of cloudiness important for climate. Thus (Arakawa, 1975) , clouds, and associated physical processes, influence the climate in the following ways:

(i) By coupling dynamical and hydrological processes in the atmosphere through the heat of condensation and evaporation and redisribution of sensible and latent heat and momentum. Thus latent heat is converted to sensible heat (or vice-versa) when clouds form (or dissipate). This sensible heating, through buoyancy forces, alters the stability of the air and thus the mixing and redistribution of various properties.

(ii) By coupling radiative and dynamical-hydrological processes in the atmosphere through the reflection, absorption and emission of radiation. Thus clouds are very important regulators of the radiation balance. They absorb and scatter incoming radiation and emit infra-red radiation.

(iii) By coupling hydrological processes in the atmosphere and in the ground through precipitation, which forms within the clouds.

(iv) By influencing the coupling between the atmosphere and the ground through modification of the radiation and the turbulent transfers at the surface, which is particularly important from the point view of the coupling between the atmospheric and oceanic circulations.

The first climate general circulation models specified cloud amount from climatology, which made them of only limited use for climate change experiments. Indeed, because of the problems associated with trying to generate realistic global cloud distributions with "interactive" cloud schemes, many climate integrations are still performed with prescibed, zonally-meaned cloud. Thus in the Met.O 20 11-layer AGCM, for example, the facility still exists to specify cloud amounts and heights , classified according to whether the cloud is "low", "medium", "high" or "convective", interpolated from values

defined at every 10 degrees of latitude for mid-January, April, July and October. In annual cycle integrations, the amounts are held constant for 15 days on either side of the middle of each of the above months and are linearly interpolated inbetween. The cloud heights are assigned the value from the month which is closest to the model date.

The prediction of cloudiness in models, in fact, presents major problems, because, firstly, the formation and dissipation processes are poorly understood and, secondly, most clouds are sub-grid scale, both horizontally and vertically. At present there are two basic approaches to predicting cloudiness. These are (ECMWF, 1985):

(i) Diagnostic or statistical schemes, in which the cloudiness is derived from other variables in the model such as the relative humidity, vertical velocity, atmospheric stability or lifting condensation level.

(ii) Prognostic schemes which include an extra model variable or variables to represent clouds and to model their formation and dissipation. In particular, they involve explicit calculation of cloud liquid water, which in some cases may be advected through the model. though numerically this is conceptually difficult to handle.

Each of these schemes has a number of advantages and disadvantages (ECMWF, 1985; Slingo,J.M., 1986). For the diagnostic schemes, these are:

*** Simplicity-they are usually easy to program, economic and relatively easy to tune to give viable predictions;

*** Because they are relatively independent of the rest of the model, they may remain relatively unaffected by other model changes (e.g. substitution of different convection schemes), though some retuning may be necessary. Their independence of the rest of the model may also be seen as a disadvantage, however, since they can only interact with other processes through the radiatively induced changes in the temperature field.

Other disadvantages of diagnostic schemes are:

*** There is often a large degree of arbitrariness in their formulation.It may be very difficult to justify the physical basis of such schemes, or the values of the tunable constants employed (reasonable looking cloud fields do not necessarily mean that a scheme makes physical sense).

*** The radiative properties of the clouds have to be prescribed, or calculated separately, sometimes on the basis of a liquid water path calculated on the basis of some ad hoc assumption. This has particular disadvantages for climate change experiments - changing cloud optical properties resulting from changes to liquid water content due to temperature rises associated with increased levels of CO_2 in the atmosphere have been suggested by Somerville and Remer (1984) to provide an important feedback process for the climate system, for example. A sound physical basis for the representation of such effects may be crucial to the success of such investigations.

There are several reasons why prognostic schemes are attractive:
*** They allow/representation of the thermodynamic effects of sub-grid scale condensation (precipitating and non-precipitating) and also

provide a more direct link between the radiative, dynamical and hydrological processes within the model.

*** Since they predict cloud liquid water content required by the radiation scheme, they therefore, in principle, allow the prediction of cloud radiative properties as well as cloud cover. This should have distinct advantages for climate change experiments.

However, there are also a number of disadvantages:

*** They are computationally more expensive than the diagnostic methods

*** Verification and interpretation currently present problems. Whilst such schemes predict variables which are, in principle, measurable, data on cloud liquid water content are very limited, either from satellites or from aircraft. Also the radiative properties of clouds are not uniquely defined by the liquid/ice water path as the cloud geometry is also important. It is necessary, then, to include additional assumptions to retrieve the cloud cover required by the radiation scheme in addition to the liquid water path.

7.2 Diagnostic cloud schemes

As an illustration of the diagnostic approach, the schemes currently employed in the Meteorological Office operational and climate models will be briefly described as well as that used at ECMWF, though it must be recognised that Sasamori (1975) has proposed a quite different scheme for the diagnostic determination of cloud cover and liquid water content. This is a statistically based scheme which takes into account the field of vertical velocity in addition to the relative humidity and temperature fields. This scheme has been tested in a GCM by, for example, Heise (1985).

The scheme currently employed in the Meteorological Office models is almost entirely humidity based, with the exception of the method for specifying the convective cloud cover, Cc and, in the operati onal models, that of marine stratocumulus. Thus in the operational models, Cc is related linearly to the maximum in the moist convective mass flux as modelled by the penetrative convection scheme (lecture 8). Different constants of proportionality are used over sea and land such that the convective cloud amount is given by:

$$Cc = 83.3 M_{max} \text{ over sea points}$$

$$Cc = 62.5 M_{max} \text{ over land points} \qquad (7.1)$$

The different constants of proportionality are intended to reflect the different characteristics of oceanic and continental condensation nucleii in determining Cc. The Met O 20 11 layer model in fact relates Cc to the "total convective parcel liquid water content", P_c, i.e. to all water above supersaturation integrated over the depth from moist convective base to the top of the convection (as determined within the convection scheme) so that:

$$Cc = 0.5 + 0.06 \ln(P_c), \qquad (7.2)$$

whilst the ECMWF model diagnoses Cc to the related time averaged precipitation rate, P, taking (J.M. Slingo, 1986):

$$Cc = a + b \ln(P) \qquad (7.3)$$

where a and b are constants.

As noted above, layer cloud is generally predicted from consideration of the large scale humidity fields in the models. In the Meteorological Office models, these clouds are assumed to be one model layer thick, with amounts parametrized by a quadratic in relative humidity such that:

$$Ch, Cm, Cl, = \frac{r - r^*}{1.0 - r^*} \qquad \text{for } r > r^* \qquad (7.4)$$

$$Ch, Cm, Cl, = 0.0 \qquad \text{for } r < r^* \qquad (7.5)$$

where Ch, Cm, and Cl stand for high, medium and low cloud amounts, free to occur in appropriately specified model layers. r^* is a critical relative humidity, taken in the operational model, for example, to have a value of 0.85. In both operational and climate models, the maximum value taken by (7.4) at a particular grid point over the range of layers appropriate to a particular class of cloud dictates the cloud amount and that layer is the one occupied by the cloud. However, in the operational model, if deep convection (convection occuring over more than 5 layers) is predicted then the cloud base is assumed to be at the base of the convective tower, and the quadratic in (7.4) is evaluated at that level only. Only 10% of convective cloud is assumed to occupy the full depth, the remainder being added to the layer cloud amount.

In essence, the ECMWF scheme (J.M. Slingo, 1986) also employs an equation of the type given by (7.4), but also has some additional features. Thus their scheme distinguishes between two different types of cirrus (Ch), that associated with high level outflow of deep convection, in which case:

$$Ch = 2.0(Cc - 0.3) \qquad (7.5)$$

provided convection extends above 400 mb and Cc exceeds 40%. Otherwise, for frontal cirrus, (7.4) is used, with $r^* = 0.8$. (7.4) is also used to specify the medium cloud amounts with r replaced by r_c the relative humidity after adjustment for the presence of convective clouds:

$$r_c = r (1.0 - Cc) \qquad (7.6)$$

This assumes that the cloudy part, Cc, is saturated. Low clouds are assumed to fall into two classes; those associated with extratropical fronts and tropical disturbances and those that occur in relatively quiescent conditions and are associated directly with the inversion-capped boundary layer. For the first class, an amount, Cl', is determined as for medium cloud, with the final amount, Cl, determined by reference to the vertical motion in the layer, ω, as illustrated in Figure 7.1a. For the second class, an initial value Cl" is determined via:

$$Cl" = -6.67 \left(\frac{\Delta \theta}{\Delta P} \right)_{min} - 0.667 \qquad (7.7)$$

where $\left(\Delta \theta / \Delta P \right)_{min}$ is the lapse rate in the most stable layer below

7.4

750mb. There is an additional dependence on relative humidity at the base of the inversion of the form shown in Figure 7.1b. The form of equation (7.7) was suggested by reference to GATE data (J.M. Slingo, 1980). A similar parametrization, based on the same reference, is also used to represent marine stratocumulus in the Meteorological Office operational model.

An example of the cloudiness field as determined within the Met O 20 11 layer model is shown in Figures 7.2 and 7.3, taken from J.M. Slingo (1986). Figure 7.2 shows the modelled mean total cloudiness, for a 90 day period, September through November. This can be compared with the observed total cloudiness for the same period (Figure 7.3) from the atlas of satellite images compiled by Miller and Feddes (1971). Note that there is no adjustment in the image for the high surface reflectivities over the deserts. The modelled total cloudiness is seen to compare quite well with the observed; the amounts are slightly high, but the minima in the subtropics are well represented as are the maxima over Central Africa and along the ITCZ. The break in the cloudiness over the Arabian Sea is also well represented.

7.3 Formation of precipitation with diagnostic cloud schemes

In general, with diagnostic cloud schemes, formation of precipitation is said occur when the air at model gridpoints becomes supersaturated as a result, for example, of convergence, radiative cooling or large-scale ascent. This excess moisture is then allowed to fall as rain or snow. The effects of evaporation and the melting of snow on the falling precipitation may also be taken into account. As an example, we describe here the scheme used in the Met O 20 11 layer model, taken from A. Slingo (1985).

Dealing first with the formation of precipitation through condensation, the contribution to the precipitation provided by condensation occurring in any layer, k, say, is derived by comparing the specific humidity, q_k, with the saturation specific humidity, $q_s(T_k)$, corresponding to the temperature, T_k, at that gridpoint. If $q_k < q_s(T_k)$ then there is no contribution to the total precipitation from that layer. If $q_k > q_s(T_k)$, however, then the excess moisture is removed and the temperature is increased through release of latent heat. Defining adjusted values of q_k and T_k by $q_s(T'_k)$ and $T'_k = (T_k + \Delta T_k)$, we have:

$$\Delta T_k = \frac{L}{c_p}(q_k - q_s(T'_k)) \qquad (7.8)$$

where L is the latent heat of condensation and c_p the specific heat of dry air at constant pressure. The adjustment is made so that the gridpoint is just saturated at the new temperature. On using the Clausius-Clapeyron relation, we have:

$$q_s(T'_k) = q_s(T_k) + \left.\frac{\partial q_s}{\partial T}\right|_{T_k} \Delta T_k = q_s(T_k)\left[1 + \frac{L \Delta T_k}{R_v T_k^2}\right] \quad (7.9)$$

where R_v is the gas constant for water vapour. Equations (7.8) and (7.9) can be solved simultaneously for ΔT_k and $q_s(T'_k)$. If the temperature is below freezing, the precipitation formed is assumed to freeze. A further contribution to the temperature increment is then derived from the additional latent heat released. The precipitation per unit mass resulting from the adjustment at this level, given by:

$$P_k = q_k - q_s(T^\bullet_k) \qquad (7.10)$$

is added to any precipitation reaching this level from above.

A number of numerical models also include the effects of evaporation on precipitation falling through unsaturated layers. This is included in both the 11 layer and operational models by specifying the evaporation per unit mass as:

$$E_k = \min(\beta(q_s(T_k) - q_k)\Delta t , Ppn) \qquad (7.11)$$

where $\beta = 0.00002$ s^{-1}, Δt is the timestep and Ppn is the precipitation falling through the layer. The formula is designed to give evaporation rates which are typically of the order of 7 mm per day per 100mb. New values of q_k and T_k, say q''_k and T''_k, as a result of the above evaporation are given by:

$$q'' = q_k + E_k \quad \text{and} \quad T''_k = T_k - LE_k/c_p \qquad (7.12)$$

where L is here the latent heat appropriate to the phase of the precipitation.

Many models also include melting of precipitation falling as snow when it enters a layer whose temperature is greater than 273K. In the 11 layer model, all the precipitation is then assumed to melt immediately, the accompanying change of temperature being given by:

$$\Delta T_k = - \frac{L_f}{c_p} \sum_{n=k+1}^{top} (P_n - E_n) \qquad (7.13)$$

A similar adjustment is made to the temperature field if the precipitation changes from rain to snow.

From the above, the amount of "large scale" precipitation reaching the surface, P* in one timestep may be calculated. Expressed in mm per unit area, this is:

$$P* = \frac{10^2}{g} P_* \sum_{n=1}^{top} (P_n - E_n) \qquad (7.14)$$

where p_* is the surface pressure.

7.4 Prognostic cloud schemes

As noted above, the so-called prognostic schemes require the introduction of an additional variable (or variables) - in particular the specific cloud liquid water content - to represent clouds, which enables a number of physical processes to be tied together and represented in a more consistent way. In such schemes, therefore, the cloud liquid water/ice variable has its own conservation equation with appropriate sources and sinks and there is additional allowance for the fact that, in general over a grid square, clouds (not only cumulus clouds, but also stratiform clouds) are often observed to form in a non-saturated environment, depending on the intensity of small- scale processes; i.e. the occurrence of sub grid-scale condensation (fractional cloud cover) is allowed for. Recently, Roeckner and Schlese (1985) have developed a scheme based on Sundqvist's (1978) approach for use in the Hamburg University GCM, which, in summary, appears to have the following form.

Firstly, it is assumed that cloud exists when the relative humidity, r, over a grid volume exceeds a constant threshold value r_0 (of order 0.8) and further, that the humidity of the the clear area is maintained at r_0 when cloud is present. In this case, the cloud is assumed to have a fractional cover, a, which, from the definition of the grid square mean humidity, $\bar{q}$, i.e.

$$\bar{q} = (1-a)r_0\bar{q}_s(\bar{T}) + a\bar{q}_s(\bar{T}) \qquad (7.15)$$

is given by:

$$a = \frac{\bar{q} - q_0}{\bar{q}_s - q_0} \qquad (7.16)$$

where $q_0 = r_0\bar{q}_s(\bar{T})$. Note the temperature is assumed to be the same and equal to the grid square mean value, $\bar{T}$, for both clear and cloudy regions.

The basic variables of the model, $\bar{T}$, $\bar{q}$, and the cloud liquid water content, m, are then governed by the following equations:

$$\frac{\partial \bar{q}}{\partial t} = A(\bar{q}) + \bar{C} + (1 - a)E \qquad (7.17)$$

$$\frac{\partial m}{\partial t} = A(m) + \bar{C} - P \qquad (7.18)$$

$$\frac{\partial \bar{T}}{\partial t} = A(\bar{T}) + \frac{L}{C_p} (\bar{C} + (1-a)E) \qquad (7.19)$$

Here, $A(x)$ represents the changes due to advection, turbulent diffusion, and, where relevant, moist and dry convection and radiation. Condensation, C is allowed to occur in clear or cloudy areas if the result of these processes is to raise the humidity if the cloudy part above 100% or that of the clear part above r_0, in a manner similar to that described for the diagnostic schemes above. C is also presumed to include evaporation of cloud liquid water, if the humidity in these regions falls below these values. Evaporation of precipitation, E, is presumed only to occur in the clear air and to be given by an equation of the form:

$$E \quad -(\bar{q} - \bar{q}_s)(Ppn)^{1/2} \qquad (7.20)$$

where $(\bar{q}-\bar{q}_s)$ represents the saturation deficit and Ppn the precipitation rate at the respective level. This parametrization, according to Kessler (1969), follows from the assumption of a "Marshall-Palmer raindrop spectrum". The parametrization of precipitation formation follows Sundqvist (1978), who related the intensity of raindrop production to liquid water content according to:

$$P = m\, C_0(1 - \exp-(m/m_r)^2) \qquad (7.21)$$

7.7

where $1/C_0$ is the e-folding time for the decrease of cloud liquid water by precipitation in the limit $m \gg m_r$. For $m \ll m_r$ clouds are essentially in the non-precipitating stage so that $m = m_r$ is said to approximately define the limit between the non-precipitating clouds and those that are in a mature, precipitating stage. C_0 is taken to have a value of 5×10^{-4} s^{-1} and m_r to have values of 0.001 g/kg for high clouds and 0.1 g/kg for middle and low clouds.

A rather different approach to the representation of cloud liquid water and grid-square fractional cloudiness has been taken by Smith (1985) in a parametrization currently under test in the Met O 20 11 layer model. In this case, a statistical cloud model is used to determine cloud cover and water content, following a model of Sommeria and Deardorff (1977) in which it is assumed that within the grid-square, there is a statistical spread of variables conserved during phase changes; i.e. of

$$T_\ell = T - Lq_\ell/c \quad \text{and} \quad q_t = q + q_\ell \quad (7.22)$$

where, for simplicity, we have ignored the ice phase, also included in the model. Here, q_ℓ is a total water content and q_t the liquid water content. Sommeria and Deardorff assume the difference, s, of the specific total water content and the saturation specific humidity to have a Gaussian spread about the grid-box mean, whilst Smith uses a triangular distribution. The details are complicated, but the use of this distribution enables a consistent cloud amount and liquid water (or ice) content to be derived. The parametrization of precipitation in the model is essentially that of Sundqvist outlined above (equation 7.21). The parametrization of boundary layer turbulent mixing is also modified by the scheme. Thus the Richard's boundary layer scheme (lecture 4) uses a local Richardson number which does not take any effects of latent heat release into account. Smith modifies the Richardson number, basing it on gradients of T_ℓ and q_t, which enable this to be allowed for in a consistent way.

As already stated, verification of results from such prognostic cloud models is, as yet, a difficult problem since direct measurements of cloud water by aircraft are not very numerous and may not be representative, whilst the, as yet, limited amount of remotely sensed data for this parameter gives estimates of the vertically integrated cloud liquid water but not ice and then over the oceans only. Further, all such measurements are, as yet, somewhat inexact. However, Figure 7.4 shows an example of the results of using Smith's scheme in the Met O 20 11 layer AGCM against SMMR data. The maximum shown in the observed data in tropical regions is not seen in the model results since, as yet, the scheme is applied to large-scale (i.e. not convective) rainfall only.

****

.nj

Advanced Lecture 7 - References

Arakawa, A., 1975, Modelling clouds and cloud processes for use in climate models. GARP Publication Series No. 16, ICSU/WMO, pp 183-197.

Clapp, P.F., 1964, Global cloud cover for seasons using TIROS nephanalyses. Mon. Weath. Rev., 92, pp. 495-507.

ECMWF, 1985, Proceedings of the workshop on cloud cover parametrization in numerical models, 26-28 November 1984.

Geleyn, J-F., 1981, Some diagnostics of the cloud/radiation interaction in the ECMWF forecasting model. ECMWF workshop on radiation and cloud-radiation interaction in numerical modelling, 15-17 October 1980, ECMWF, pp. 135-162.

Heise, E., 1985, Experiments with the Sasamori and the ECMWF cloud cover and liquid water content parametrizations. In ECMWF (1985), pp. 109-131.

Miller, D.B. and R.G. Feddes, 1971, Global analysis of relative cloud cover, 1967-1970, based on data from meteorological satellites, Washington NOAA/NESS, Washington Air Weather Service.

Njoku, E.G. and L. Swanson, 1983, Global measurements of sea surface temperature, wind speed and atmospheric water content from satellite microwave radiometry. Mon. Weath. Rev., 111, pp. 1977-1987.

Roeckner, E. and U. Schlese, 1985, January simulation of clouds with a prognostic cloud cover scheme. In ECMWF (1985), pp. 87-108.

Sasamori, T., 1975, A statistical model for stationary atmospheric cloudiness, liquid water content and rate of precipitation. Mon. Weath. Rev., 103, pp.1037-1049.

Slingo, A., 1985, Editor: Handbook of the Meteorological Office 11-layer atmospheric general circulation model. Vol. 1: Model description. Met O 20 Tech Note, DCTN 29.

Slingo, J.M., 1980, A cloud parametrization scheme derived from GATE data for use with a numerical model. Quart. J.R.Met. Soc., 106, pp. 747-770.

Slingo, J.M., 1984, Studies of cloud-radiation interaction in the ECMWF medium range forecast model. Proc. of the IAMAP international radiation symposium, 21-29 August 1984, Italy, (in press).

Slingo, J.M., 1985, Cloud cover experimentation with the ECMWF model. In ECMWF (1985) pp. 163-212.

Slingo, J.M., 1986, Parametrization of cloud cover. Proceedings of the ECMWF seminar on physical parametrization for numerical models of the atmosphere, 9-13 September 1985, Volume II. ECMWF, pp. 17-46.

Smith, R.N.B., 1985, An integrated approach to the representation of cloud processes. In ECMWF (1985), pp. 233-248.

Somerville, R.C.J. and L.A. Remer, 1984, Cloud optical thickness

feedbacks in the CO_2 climate problem. J.Geophys. Res., 89, No. D6, pp. 9668-9672.

Sundqvist, H., 1978, A parametrization scheme for non-convective condensation including prediction of cloud water content. Quart. J.R. Met. Soc., 104, pp. 677-690.

(a)

(b)
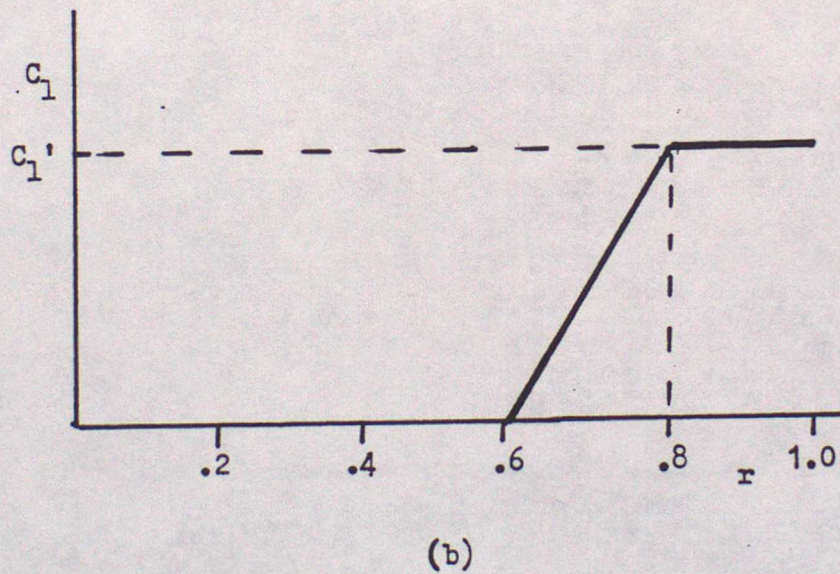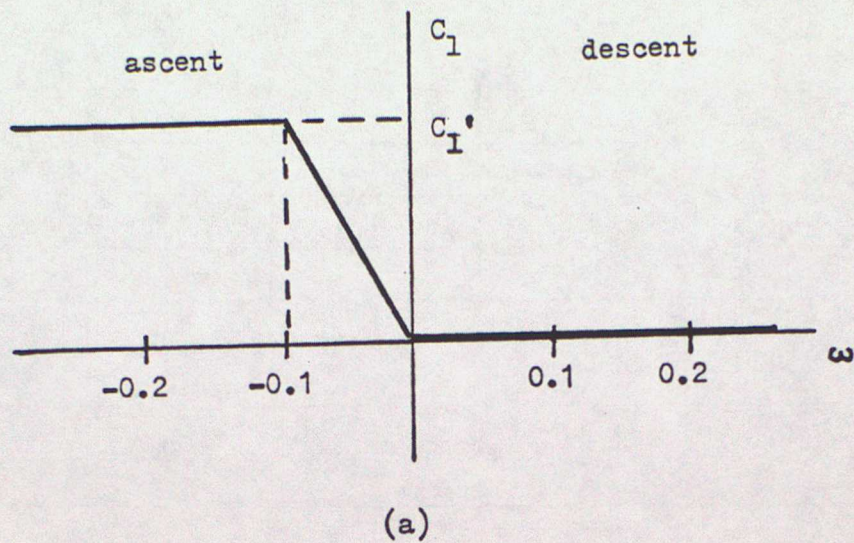
Figure 7.1 (a) Relationship between low level cloud amounts in disturbed conditions and vertical motion in the ECMWF model and (b) between relative humidity at the base of the inversion and low level cloud in quiescent conditions, again for the ECMWF model. For definition of symbols, see text.
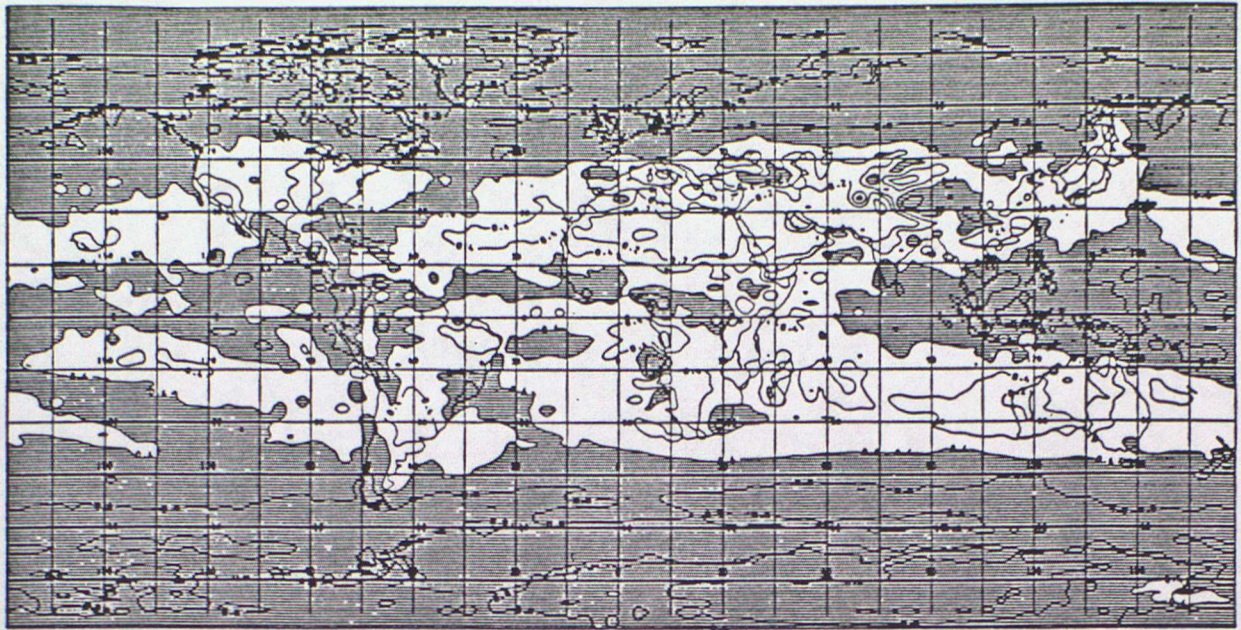
Figure 7.2   Mean distribution of total cloud for 90-day period, September
   through November, from the UK Meteorological Office climate
              model.
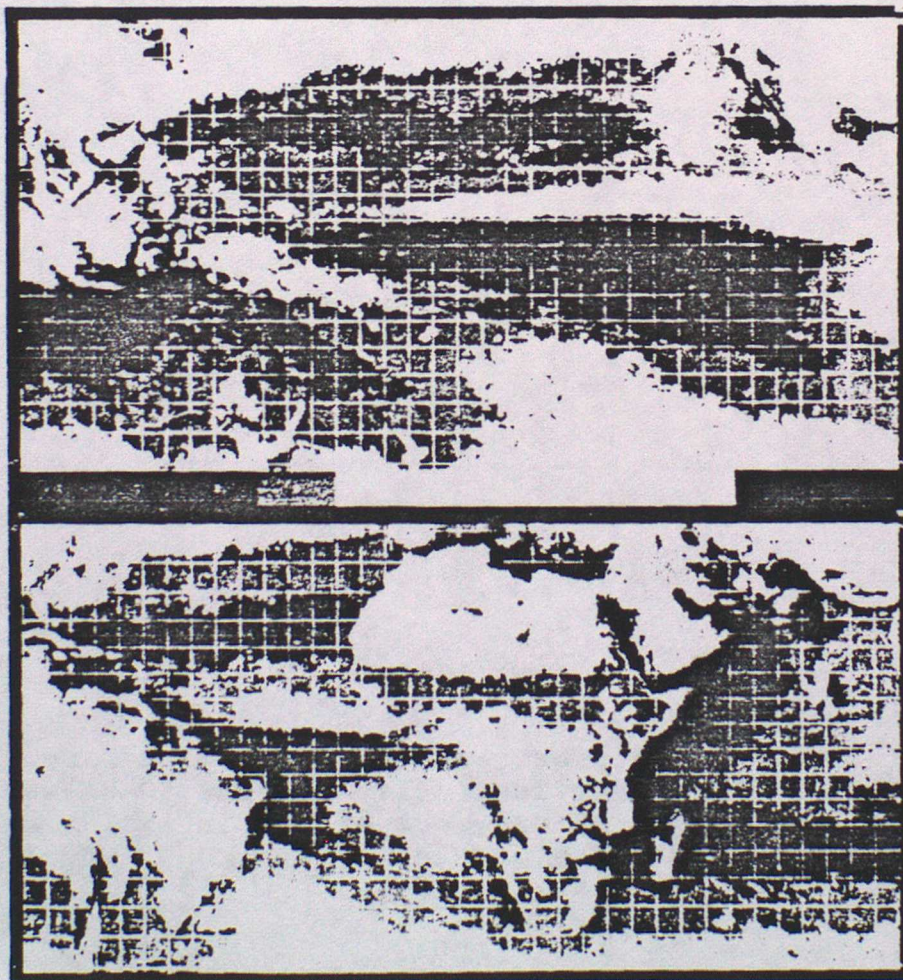
Figure 7.3   Satellite observed total cloudiness for 40°N-40°S, September
              through November 1967-1970, from Miller and Feddes (1971).
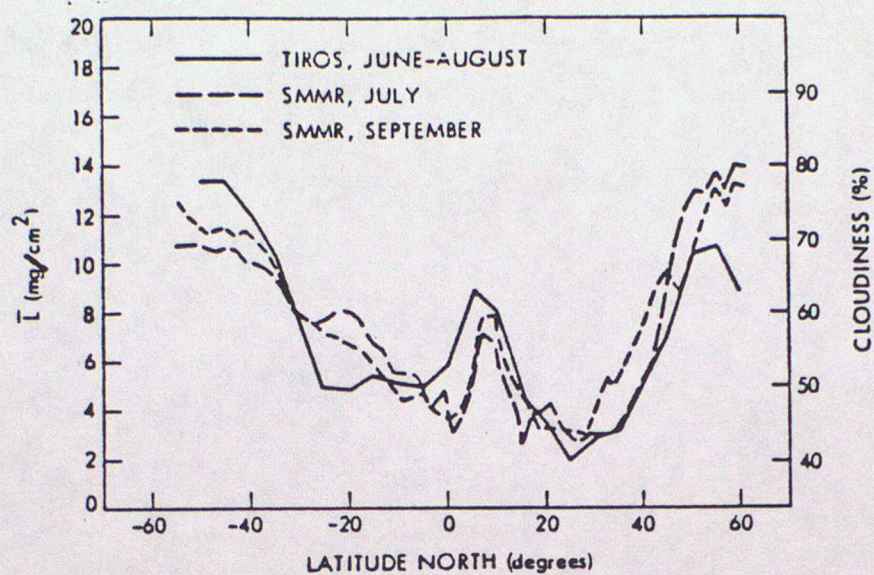
(a)
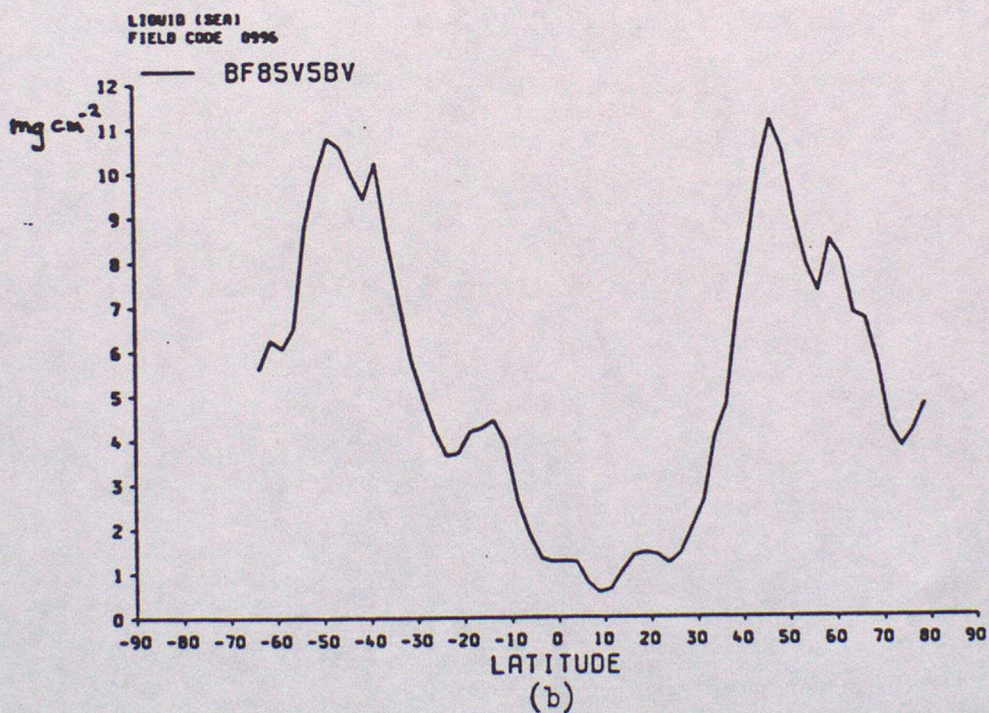
(b)

Figure 7.4 (a) Zonally averaged cloud liquid water for the periods 11
July-10 August 1978 and 11 September-10 October 1978 derived from
data from the Scanning Multichannel Microwave Radiometer (SMMR). Also
shown is fractional cloud cover as deduced from TIROS observations by
Clapp (1964) (from Njoku and Swanson, 1983). (b) The September to
November (3 monthly) mean of the vertical integral of the zonally
averaged cloud liquid water over sea points from an integration of the
Met O 20 model.

.nj

Advanced Lecture 8

Parametrization of convection

8.1 Introduction

　　　　　Cumulus convection in the atmosphere is one of the
main energy producing mechanisms which occur at scales unresolvable by
large-scale numerical models and which strongly interact with
large-scale processes. As noted in ECMWF (1984) the accuracy of its
parametrization has become more crucial due to the rapid development
and sophistication of numerical weather forecasting and climate
modelling. Moreover, it is now evident that the large-scale
circulation of the tropical areas have a strong influence on
mid-latitude systems and on the general circulation as a whole. The
fact that tropical weather systems are largely driven by convective
processes emphasises the importance of the quality of convective
parametrizations.

　　　　Convection is an important process in the oceans also since it
provides the means whereby the surface layers may more rapidly
communicate with the deeper layers below. Oceanic convection is
essentially driven by surface cooling, though it may also be brought
about by enhancing the salinity of the upper waters, by extrusion of
salt during freezing of sea ice, for example. Deep oceanic convection
is therefore essentially a high latitude process. As yet
large-scale ocean models have only included representation of
convective overturning via very simple "convective adjustment"
schemes. Thus in the Bryan ocean model (see Lecture 1), at each
timestep each layer of water is given the opportunity to mix with the
layer immediately above and/or below it. Mixing of two layers, k and
k+1, say, is carried out only when the upper layer is found, upon
adiabatic displacement to the lower layer, to have a greater density
than that layer, in which case the potential temperatures, Θ, in the
two layers are set to the same values according to:

$$\Theta = (\Theta(k)dz(k) + \Theta(k+1)dz(k+1))/(dz(k) + dz(k+1)) \quad (8.1)$$

and similarly for salinity. dz(k) and dz(k+1) are the layer
thicknesses. Adjusting the layers successively in pairs in this
fashion may, of course, still leave the final profile unstable, in
which case the process may have to be repeated a number of times to
achieve stability to a pre-specified tolerance. Such a scheme
essentially represents the state of the art as far as the
representation of convection in ocean models is concerned. Since, as
in the atmosphere, convection in the ocean is generally a localised
phenomenon, which occurs on horizontal scales much smaller than that
of an individual grid square, there is a need for substantially
improved representations of the processes involved, including
representation of the penetrative effects of convection, akin to
treatments currently available for the atmosphere, though, of course
without the added complications of release of latent heat.

　　　　For the rest of this lecture, we shall therefore concentrate on
a description of some of the ways in which convection is parametrized
in atmospheric models - broadly referred to as "cumulus
parametrization" - following, in part, the recent review of the
subject by Anthes (1984).

The problem of cumulus parametrization is to relate the convective condensation and transports of heat, moisture (and momentum) by cumulus clouds, which cannot be explicitly resolved by the large-scale model, to the variables predicted by the model. There are two important aspects of cumulus parametrization. One is the modulation of convection by the large-scale forcing. The other is to predict the effects of the convection upon the large-scale dynamic and thermodynamic variables, and thereby on the larger scale flow, which is related to the vertical distribution of condensation and evaporation in the clouds and the vertical transport of heat, moisture and momentum. Additional requirements of a such a parametrization for a large-scale model are those of relative simplicity and the need for the scheme to preserve a physically reasonable vertical structure with in the model atmosphere.

As summarized in ECMWF (1984), there are now a number of different parametrization schemes in existence and these can be classified into two types:

(a) Schemes having no explicit cloud model:

** Convective adjustment schemes

** Kuo-type schemes

(b) Schemes having explicit cloud models

** Arakawa-Schubert (1974) scheme, in which a cloud model is combined with the concept of an ensemble or spectrum of clouds being present over each grid-square. This is probably the most complex scheme currently existing and has been implemented in the UCLA GCM (see, e.g. Lord et al., 1982).

** Miller-Moncrieff (1984) scheme, in which different analytic cloud models can be incorporated, depending on grid-scale properties such as the "convective available potential energy" (CAPE) and vertical shear. A novelty of the scheme is that different types of momentum transport can be implemented, depending on the cloud model used.

** Other schemes, in which various other methods of specifying the convective mass flux have been implemented. These include the scheme due to Rowntree, currently employed in the Met O 20 AGCM and the operational model. In some respects, this scheme can be regarded as a simplified version of the Arakawa-Schubert scheme and of the explicit cloud schemes, if for no other than reasons than those of parochial interest, is the one which will be outlined below.

First, however, we shall give brief mathematical background to some of the concepts applicable to the cumulus parametrization problem.

8.2 Mathematical framework.
We shall concentrate attention on the thermodynamic and water vapour equations in the form:

$$\frac{\partial T}{\partial t} + \nabla \cdot \underset{\sim}{V}_h T + \frac{\partial \omega T}{\partial p} - \frac{\omega R T}{c_p p} = \frac{L}{c_p} C^* + Q_R \qquad (8.2)$$

$$\frac{\partial q}{\partial t} + \nabla \cdot \underset{\sim}{V}_h q + \frac{\partial \omega q}{\partial p} = -C^* \qquad (8.3)$$

Here, T is temperature, $\underset{\sim}{V}_h$ is the horizontal wind vector, ω is the vertical velocity in pressure coordinates (Dp/Dt), R is the gas constant for dry air, L is the latent heat of condensation, c_p the specific heat at constant pressure for dry air, q the humidity mixing ratio, Q_R the rate of temperature change due to radiative effects and C* is the net condensation (condensation minus evaporation, c-e). For simplicity, the ice phase is neglected. These equations are valid for only small parcels of air; to be made applicable to the scale of the variables appropriate to the grid area of a large-scale numerical model, they must be appropriately averaged. Separating any particular variable, X, into its grid square mean (denoted by a bar) and its fluctuation from that mean (denoted by a prime), yields, after some approximations:

$$\frac{\partial \bar{T}}{\partial t} + \nabla \cdot \bar{\underset{\sim}{V}}_h \bar{T} + \frac{\partial \bar{\omega}\bar{T}}{\partial p} - \frac{\bar{\omega}\bar{\alpha}}{c_p} = \frac{L}{c_p}\bar{C}^* + \bar{Q}_R - \frac{\partial \overline{\omega' T'}}{\partial p} - \frac{\overline{\omega'\alpha'}}{c_p} \qquad (8.4)$$

$$\frac{\partial \bar{q}}{\partial t} + \nabla \cdot \bar{\underset{\sim}{V}}_h \bar{q} + \frac{\partial \bar{\omega}\bar{q}}{\partial p} = -\bar{C}^* - \frac{\partial \overline{\omega' q'}}{\partial p} \qquad (8.5)$$

If potential temperature, θ, rather than temperature, is used, the thermodynamic equation becomes:

$$\frac{\partial \bar{\theta}}{\partial t} + \nabla \cdot \bar{\underset{\sim}{V}}_h \bar{\theta} + \frac{\partial \bar{\omega}\bar{\theta}}{\partial p} = \frac{L}{c_p}\left(\frac{p_o}{p}\right)^{R/c_p}\bar{C}^* + \left(\frac{p_o}{p}\right)^{R/c_p}\bar{Q}_R - \frac{\partial \overline{\omega'\theta'}}{\partial p} \qquad (8.6)$$

where p_o is a reference pressure (1000 mb). Another thermodynamic variable frequently used is the dry static energy $s = c_p T + gz$. The equation governing s is:

$$\frac{\partial \bar{s}}{\partial t} + \nabla \cdot \bar{\underset{\sim}{V}}_h \bar{s} + \frac{\partial \bar{\omega}\bar{s}}{\partial p} = L\bar{C}^* + c_p \bar{Q}_R - \frac{\partial \overline{\omega' s'}}{\partial p} \qquad (8.7)$$

Considering the terms in these equations ((8.5) and (8.6)), note that from the thermodynamic equation (8.6), cumulus convection modifies the large-scale temperature through diabatic heating (cooling) due to condensation (evaporation) (the C* term) and through vertical eddy fluxes associated with correlations between temperature and vertical velocity; the presence of the clouds also modifies the radiative field (Q_R term). The water vapour equation (8.5) shows cumulus convection to decrease (increase) the average mixing ratio when condensation (evaporation) prevails at a given level. The eddy flux term represents a net vertical transport of water vapour - upward in the typical case

when moist updraughts and dry environmental subsidence are present.

Quantities often met in the literature on cumulus convection in the context of both observational and modelling studies are the "apparent heat source", Q_1, given by:

$$c_p Q_1 = \frac{\partial s}{\partial t} + \nabla \cdot \underset{\sim}{V_h} s + \frac{\partial \omega s}{\partial p} \qquad (8.8)$$

and the "apparent moisture sink", Q_2:

$$Q_2 = -\frac{L}{c_p} \left(\frac{\partial q}{\partial t} + \nabla \cdot \underset{\sim}{V_h} q + \frac{\partial \omega q}{\partial p} \right) \qquad (8.9)$$

where the 'bars' over mean variables have been dropped for convenience. A further useful quantity is the moist static energy:

$$h = c_p T + gz + Lq = s + Lq \qquad (8.10)$$

From the definitions of Q_1 and Q_2 and equations (8.5) and (8.7), we have, therefore,

$$Q_1 = \frac{L}{c_p} C* + Q_R - \frac{1}{c_p} \frac{\partial \overline{\omega' s'}}{\partial p} \qquad (8.11)$$

$$Q_2 = \frac{L}{c_p} (C* + \frac{\partial \overline{\omega' q'}}{\partial p}) \qquad (8.12)$$

Vertical integration from a pressure p_t, the top of the highest clouds, to the surface yields, when averaged over the lifetime of convective systems within the large-scale area:

$$\frac{c_p}{g} \int_{p_t}^{p_s} (Q_1 - Q_R) dp = LP + H \qquad (8.13)$$

where P is the precipitation at the surface and H the surface sensible heat flux; and:

$$\frac{c_p}{g} \int_{p_t}^{p_s} Q_2 dp = L(P - E) \qquad (8.14)$$

where E is the rate of evaporation at the surface. These equations serve as independent checks on the vertical integrals of $Q_1 - Q_R$ and Q_2 as estimated from observations, assuming P, H, and E can be measured. Profiles of Q_1 and Q_2 deduced from observational studies can also be used to verify the characteristics of convective model results (see figure 8.1).

We conclude this section by briefly considering some aspects of the representation of the vertical eddy flux terms in the

thermodynamic and moisture equations. The most general cumulus parametrization schemes consider a spectrum or ensemble of clouds of different sizes and dynamic and thermodynamic properties and attempt to compute the net effect of the cloud ensemble by integrating over the whole spectrum of individual cloud effects. For simplicity, we consider here the effects of only one particular cloud type, recognising that the approach can be generalised to a whole ensemble of clouds by summation over all cloud types.

We first separate the large-scale vertical motion into the average vertical velocity in the cumulus clouds, ω_c, and the vertical velocity, $\tilde{\omega}$, in the environment of the clouds. If a is the area occupied by the clouds then:

$$-\overline{M} = \overline{\omega} = a\,\omega_c + (1-a)\tilde{\omega} = -M_c - \tilde{M} \qquad (8.15)$$

Likewise, we also have:

$$\overline{s} = as_c + (1-a)\tilde{s} \qquad (8.16)$$

$$\overline{q} = aq_c + (1-a)\tilde{q} \qquad (8.17)$$

and we can deduce that:

$$\overline{\omega's'} = a(1-a)(\omega_c-\tilde{\omega})(s_c-\tilde{s}) \qquad (8.18)$$

$$\overline{\omega'q'} = a(1-a)(\omega_c-\tilde{\omega})(q_c-\tilde{q}) \qquad (8.19)$$

Most cumulus parametrizations assume the area occupied by cloud to be a small fraction of the total area. In this case, if $a \ll 1$ and $|\tilde{\omega}| \ll |\omega_c|$, these approximate to

$$\overline{\omega's'} = a\omega_c(s_c-\tilde{s}) = -M_c(s_c-\tilde{s}) \qquad (8.20)$$

$$\overline{\omega'q'} = a\omega_c(q_c-\tilde{q}) = -M_c(q_c-\tilde{q}) \qquad (8.21)$$

since $s_c-\tilde{s} = c_p(T_c-\tilde{T})$, this shows that the vertical eddy fluxes of dry static energy (or heat) and water vapour are proportional to the cloud vertical velocity and the temperature or moisture excess of the cloud.

We now consider some particular aspects of cumulus parametrization schemes.

8.3 Convective adjustment schemes

Moist convective adjustment schemes are among the conceptually simplest methods of parametrizing the effects of cumulus convection on the environment. Such parametrizations essentially involve mixing of adjacent layers of the model atmosphere when certain criteria for conditional instability are satisfied. A variety of schemes have been proposed and used in models. thus, for example, Manabe et al (1965) assumed, for the GFDL model, a mixture of moist convective adjustment and large-scale condensation to occur when the lapse rate exceeds the moist adiabatic and the computed

relative humidity is greater than 100%. The adjustments dT and dq for each of the set of moist unstable layers, bounded by pressure levels p_B and p_T, are then computed by simultaneously solving finite difference versions of:

$$\frac{\partial}{\partial p} \, \theta_e(T+dT, \; q+dq, \; p) = 0 \qquad \text{(n-1) equations} \qquad (8.22)$$

$$q + dq = q_s(T+dT, p) \qquad \qquad \text{(n equations)} \qquad (8.23)$$

$$\frac{1}{\partial} \int_{p_B}^{p_T} (c_p dT + Ldq)dp = 0 \qquad \qquad (8.24)$$

The first of these equations specifies the equivalent wet bulb potential temperature of the final sounding to be constant with height over the layers adjusted. The second specifies the change in the mixing ratio necessary to bring the humidity down to 100% and the third is a requriement that the moist static energy be conserved between the initial and final profiles. This latter assumption is common to most, if not all convective adjustment schemes.

Krishnamurti and Moxim (1971) describe a convective adjustment scheme which is initiated when an initial large-scale sounding has a set of layers for which the equivalent wet bulb potential temperature decreases with height. The adjustment is then made such that θ_e, or equivalently the moist static energy is constant with height over an appropriate number of levels (Figure 8.2). The details of the scheme are somewhat obscure, but Krishnamurti et al. (1980) demonstrate that use of such a scheme severely overestimates the predicted rainfall. (Figure 8.3a). Such a scheme has therefore been termed "hard convective adjustment" in contrast to the so-called "soft adjustment" schemes in which "hard adjustment" is assumed to occur only over a limited area, A, of the grid square. The value of A has to be determined by a criterion based on the mean relative humidity of the column by which an iterative search is carried out for a value of A which makes the final value of the vertically integrated relative humidity equal to a prescribed value (~80%). That such schemes give more realistic rainfall amounts was also demonstrated by Krishnamurti et al. (Figure 8.3b), though they also noted that, because of the occurrence of maximum instability before the time of maximum convection in the tropics, the soft scheme that they tested shows a lag of some two days between the computed and observed rainfall. This lag makes such schemes undesirable for use in forecast models in which predicting the correct timing is as important as predicting the correct amount. However such schemes may still be suitable for use in climate models for which the timing of precipitation is less important.

8.4 Kuo schemes

In essence, in the Kuo scheme, an attempt is made to relate the rainfall rate to the large-scale moisture convergence. If we consider a column of the atmosphere extending from the surface to the top of the convective cloud layer, then it is evident (Figure 8.4) that:

$$M_t + M_{t\ell} + E = P + S_{q_v} + S_{q_\ell} \qquad (8.25)$$

where M_t is the integrated moisture convergence, $M_{t\ell}$ is the convergence of liquid water, E is the surface evaporation rate, S_{wv} is the rate of storage of water vapour and $S_{w\ell}$ is the rate of storage of liquid water. If the storage rates of vapour and liquid water, together with the liquid water convergence are small, then this equation reduces to:

$$M_t + E = P \qquad\qquad (8.26)$$

Whilst such an approximation may be applicable over large regions and long time scales, locally and on short temporal scales, there can be substantial changes in the storage of both water vapour and liquid water. In general there is a higher variability in mid-latitudes than over the tropics. Key issues of Kuo-type schemes are, therefore:

** to relate the storage term(s) to the large scale variables. i.e. to determine what portion of the moisture convergence, b, should go into storage and what portion, l-b, should be removed as precipitation. (Figure 8.5).

** to determine how the apparent heat source $(1-b)M_t$, which specifies also the amount of condensational heating is partitioned in the vertical.

** to determine the vertical partitioning of the apparent moisture sink, given by bM_t, in increasing the humidity of the column.

Details of how these problems have been approached are given in the summary by Anthes (1984). We simply note here, that in such schemes, the cloud properties (T_c and q_c) are usually determined by the wet adiabat associated with the equivalent potential temperature of a parcel of air originating close to the surface.

8.5 An example of an explicit cloud model scheme

As noted above we shall here describe the scheme currently in use in the Meteorological Office operational and climate models and which was developed, following on from that of Rowntree (1973), with reference to results from GATE (see Lyne and Rowntree (1976). These notes are taken from the description given in Slingo (1985) and the summary by Rowntree (1984). It is based on the concept of parcel theory modified by entrainment with a treatment of cloud detrainment based partly on Ceseleski (1972 p 102) and his discussion of the scheme of Arakawa (1969).

We imagine an ensemble of buoyant plumes of varying characteristics (temperature, humidity, cross-sectional area) starting at one level and extending upwards to different heights depending on their characteristics. The plumes entrain environmental air over their leading and side surfaces as they push into the environmental air; the less buoyant plumes terminate through lack of buoyancy and detrain at a lower level than more buoyant ones which, perhaps because their original large cross-section or the more favourable nature of the local environment into which they have risen, have led more protected lives and may even reach the heights accessible to an undilute parcel. Since detrainment is generally assumed to occur with zero buoyancy, the heating of the environment occurs, as in Arakawa's scheme, mainly through the mass descent which compensates the ascent of the buoyant plumes, although moistening by detrainment and re-evaporation of condensed moisture do mitigate the drying and warming effects of this

descent.

In more detail, for each grid column we work upwards until we find a level at which a parcel starting with an excess buoyancy (given by taking the parcel potential temperature to be that of the environment plus 0.2k) relative to the environment will still be buoyant after rising to the next level and entraining some environmental air en-route. If at this level it still has an excess buoyancy greater than a certain lower limit (equal to that given to the starting parcel) the convective process is initiated. Note that the initial mass flux, M_I, of the ensemble taken to be proportional to this excess buoyancy (E) according to:

$$M_I = (2\Delta t)(3.33 \times 10^{-7})(E/\Delta\sigma) \qquad (8.27)$$

where Δt is the timestep and $\Delta\sigma$ the depth of the layer in σ coordinates. The constant in this expression was chosen on the basis of experience. M_I is not allowed to exceed the thickness of the shallowest model layer, whilst convection is not initiated if $M_I < (2 \times \Delta t)(3.33 \times 10^{-7})$.

The finite difference treatment of the "ensemble" is indicated in Figure 8.6. Here, δ_k is is a fractional rate of "forced detrainment" (see below) at level k, η_k is the fractional rate of detrainment due to mixing and $\epsilon_{k+1/4}$, $\epsilon_{k+3/4}$ are the fractional entrainment rates at levels k+1/4 and k+3/4. The entrainment and mixing rates are specified empirically, whilst the forced detrainment rate is determined as follows. At each level the ensemble reaches, we calculate whether, after allowing for entrainment and detrainment due to mixing between that level and the next, the mean ensemble will still be buoyant. If it is not we find what proportion of the less buoyant part of the ensemble needs to be detrained, at a density equal to that of the environment, at the lower level to allow the residue of the ensemble to continue to be buoyant at the next level at which the new mass flux is determined as in Figure 8.6. Note the corresponding compensating mass flux in the environment which itself is modified by evaporation of detrained cloud water. Note that the effects of moisture on density are allowed for both in detrainment and in the buoyancy test. Because the detrainment allows an infinite extrapolation towards greater buoyancy it is necessary to limit it. A simple restriction is that even the most buoyant plumes should not rise higher than an undilute parcel would. A lower limit is also placed on the mass flux on the assumption that an ensemble of small total cross-section will be destroyed by entrainment. Where these restrictions bring the convective process to an end, the residual air is detrained between the highest layer reached and the layer above (split final detrainment). The search for further mutually unstable layers is resumed in the layer above that in which this final detrainment occurs.

Within the cloud, cloud water is assumed to form, with a mixing ratio at level k+1 given by:

$$X^P_{k+1} = \frac{X^P_k}{(1 + \epsilon_{k+\frac{1}{4}})(1 + \epsilon_{k+\frac{3}{4}})} + \gamma_{k+1}(q^P_{k+1} - q_s(\theta^P_{k+1})) \qquad (8.28)$$

where the superscript p denotes a parcel value and $\gamma_{k+1} = 1$ if $q^p_{k+1} > q_s(\theta^p_{k+1})$; otherwise $\gamma_k = 0$.

Observations of summer convection suggest that precipitation does not occur until clouds attain a substantial depth. This depends on the aerosol size spectrum and is much greater for nucleus-rich continental air than for maritime air which has fewer but typically larger nucleii. At low temperatures on the other hand, ice crystal growth allows precipitation to form more readily and winter showers often result from quite shallow clouds. The convection scheme takes account of these effects by inhibiting precipitation unless the cloud depth, D_k, measured from the bottom of the first convective layer with a saturated parcel to the top of layer k, exceeds a critical value Dmin. The values used for Dmin are based on observational data (Ludlam, 1980). They are: 4km over land points; 1.5km over sea points; 1km if $T_{k+1} < 263K$.

After fall-out of precipitation commences, some water is retained in the cloud by specifying a minimum cloud water content, Xmin, below which no precipitation can fall out from the layer. The amount produced, in mm per unit area by taking the ensemble from level k to k+1 is given by:

$$P_k = (X^p_{k+1} - Xmin) \, M_{k+1} \frac{10^2 \, p_s}{g} \qquad (8.29)$$

The falling precipitation is allowed to change state as it crosses the freezing level (273k), with the model temperature fields changed accordingly, whilst the precipitation falling below cloud base is evaporated when it is diagnosed as rain.

Further details, including those on energy budget checks, are to be found in Slingo (1985).

.nj

Advanced Lecture 8 - References

Anthes, R.A., 1977, A cumulus parametrisation scheme utilising a one-dimensional cloud model. Mon. Wea. Rev., 105, pp 270-286.

Anthes, R.A., Cumulus parametrization. Draft of a contribution to the dynamics of clouds and mesoscale meteorological systems. Volume I. The dynamics of clouds by W.R. Cotton and R.A. Anthes.

Arakawa, A., 1969, Representation of cumulus convection. Proceedings of the WMO/IUGG Symposium on Numerical Weather Prediction, Tokyo. Japan Met. Agency Tech. Report 67, pp IV - 8-1 to IV - 8-6.

Arakawa, A., and W.H. Schubert, 1974, Interaction of a cumulus cloud ensemble with the large-scale environment. Part I. J.Atmos. Sci., 31, pp 674-701.

Ceseleski, B.F., 1972, A comparison of cumulus parametrization techniques in numerical integrations of an easterly wave. Report 72-1 (Part 4), Dept. Met. Florida State University, Tallahassee, U.S.A.

ECMWF, 1984, Workshop on convection in large-scale numerical models 28 November-1 December 1983.

Kuo, H.L., 1974, Further studies of the parametrization of the influence of cumulus convection on large-scale flow. J.Atmos Sci., 31, pp 1232-1240.

Krishnamurti, T.N. and W.J. Moxim, 1971, On parametrization of convective and non-convective latent heat release. J.Appl. Meteor., 10, pp3-13.

Krishnamurti, T.N., Y. Ramanathan, H.-L. Pan, R.J. Pasch and J. Molinari, 1980, Cumulus parametrization and rainfall rates I. Mon. Wea. Rev., 108, pp 465-472.

Lord, S.J., W.C. Chao and A Arakawa, 1982, Interaction of a cumulus cloud ensemble with the large-scale environment. Part IV: The discrete model. J.Atmos. Sci., 39, pp 104-113.

Lyne, W.H. and P.R. Rowntree, 1976, Development of a convective parametrization using GATE data. Met. O 20 Tech. Note II/70.

Manabe, S., J. Smagorinsky and R.F. Strickler, 1965, Simulated climatology of a general circulation model with a hydrological cycle. Mon. Wea. Rev., 93, pp 769-798.

Miller, M.J. and M Moncrieff, 1984, The use and implementation of dynamical cloud models in a parametrization scheme for deep convection. In ECMWF (1984).

Ogura, Y., 1984, Response of cumulus clouds to large-scale forcing and cumulus parametrization. Paper presented at the FGGE workshop, 9-20 July 1984, Woods Hole, MA, National Research Council.

Rowntree, P.R., 1973, Proposed convection scheme for the 11-layer tropical model. Unpublished typescript, Met O 20.

Rowntree, P.R., 1984, Sensitivity of global simulations to the formulation of the evaporation of convective condensates. In ECMWF (1984).

Slingo, A., 1985, Editor, Handbook of the Meteorological Office 11-layer atmospheric general circulation model. Volume 1: General description. Met. O 20 Tech. Note DCTN 29.
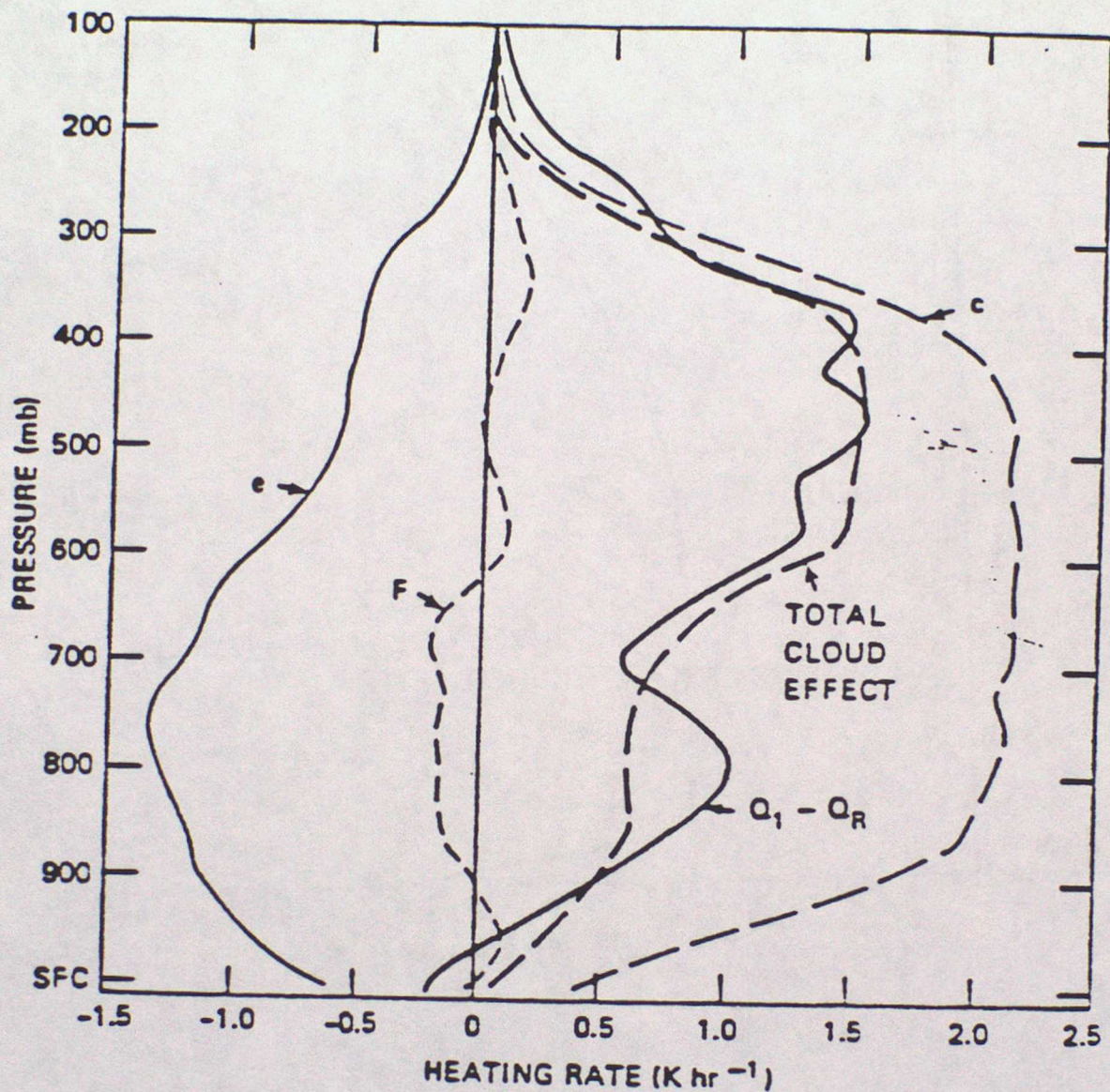
Figure 8.1 Time-averaged heating rate by condensation (c), evaporation (e), and the vertical transport of sensible heat by clouds (F) predicted by a two-dimensional cumulus ensemble model. Sum of the three terms represents the total cloud heating effect. Cloud heating effect estimated from a large-scale heat budget over the period 06-12 GMT 12 August 1974 is denoted by $Q_1 - Q_R$ (Ogura, 1984).
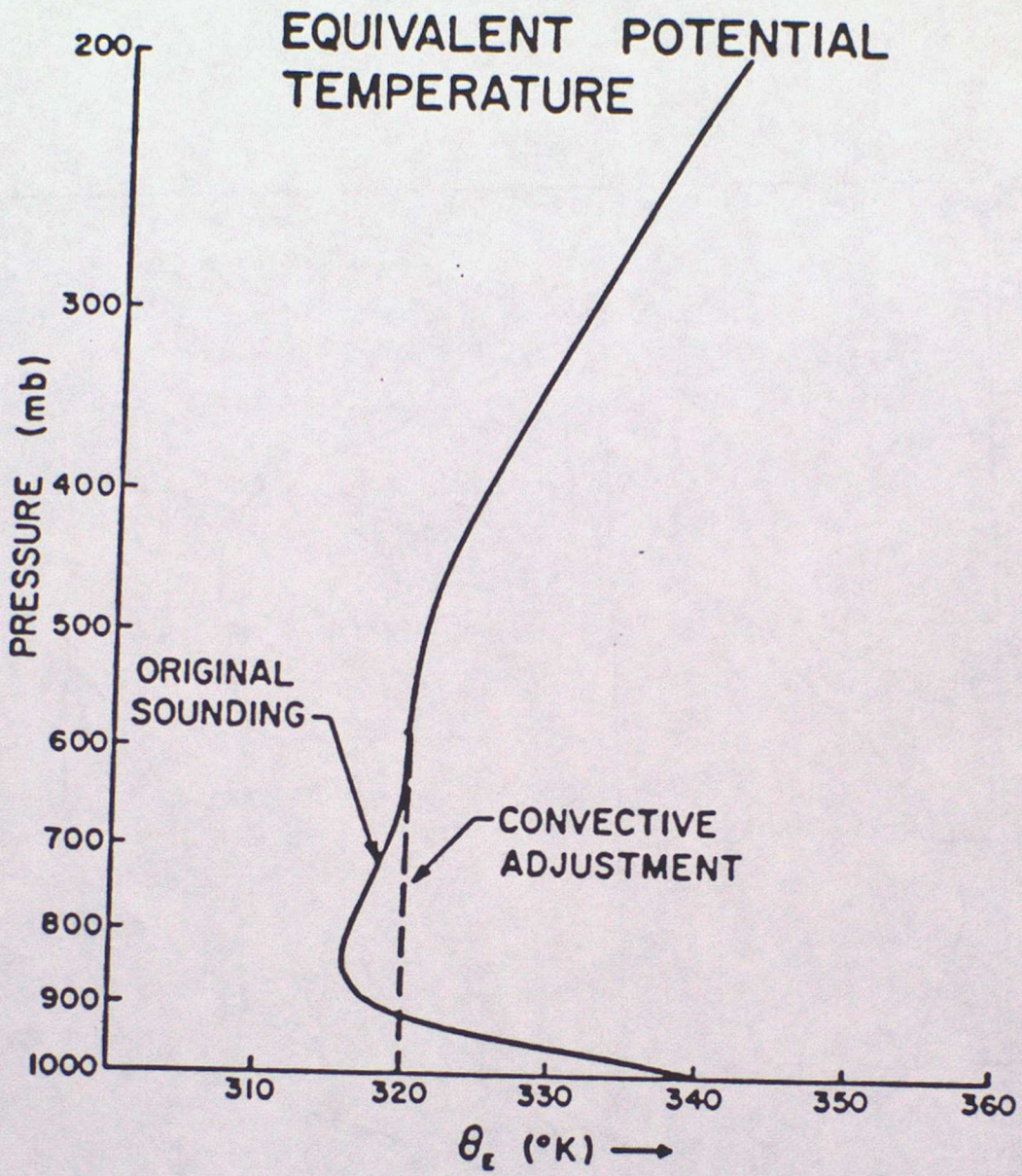
Figure 8.2 Example of a convectively unstable profile of equivalent wet bulb potential temperature. Dashed line represents the sounding after convective adjustment (see Krishnamurti and Moxim (1971)).
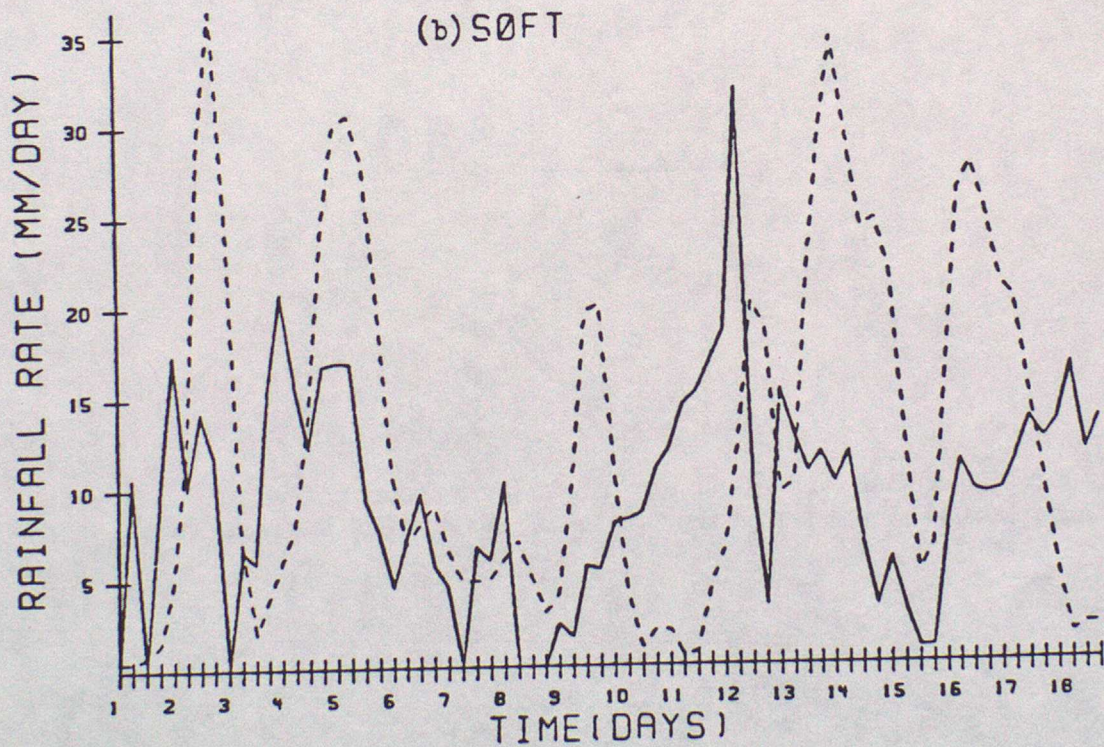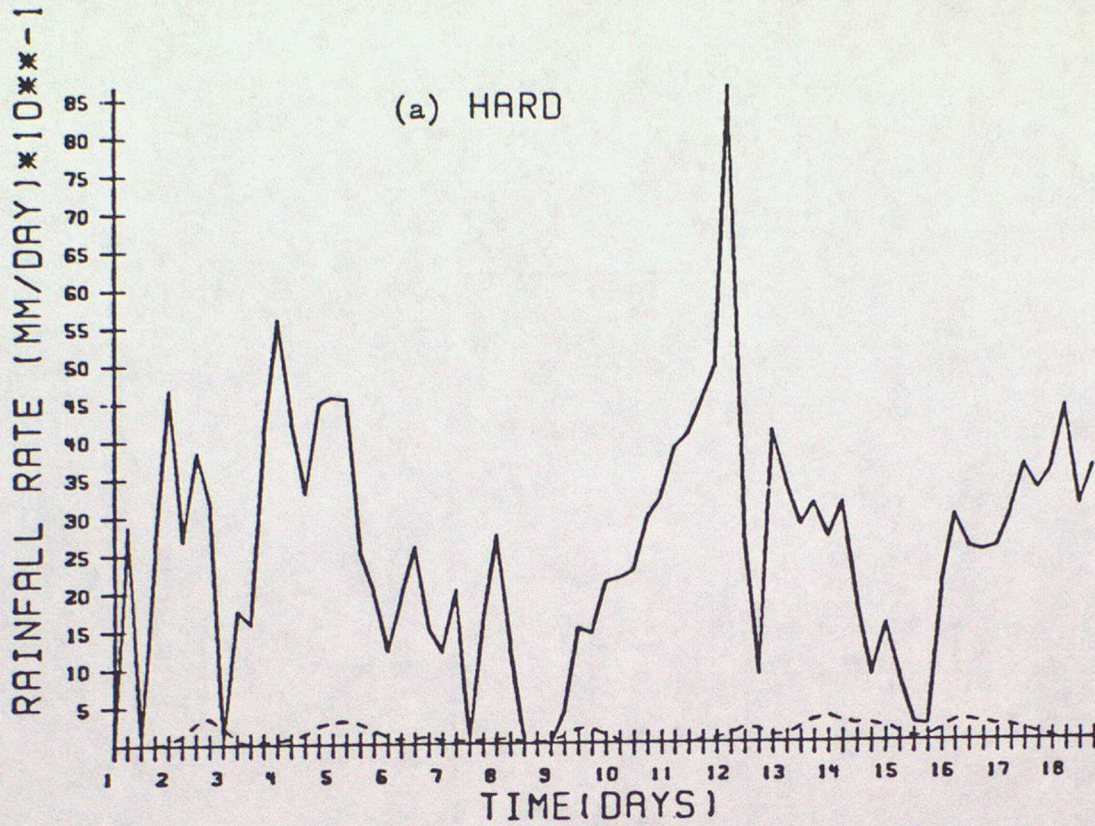
Figure 8.3 Comparison of observed (dashed line) and predicted (solid line) rainfall rates (mm day^{-1}) using (a) hard convective adjustment and (b) soft convective adjustment. Days 1 to 18 correspond to the third phase of GATE between 1 Sept. and 18 Sept 1974. Data are for 6 h intervals beginning with 00 GMT 1 Sept. (from Krishnamurti et al., 1980).
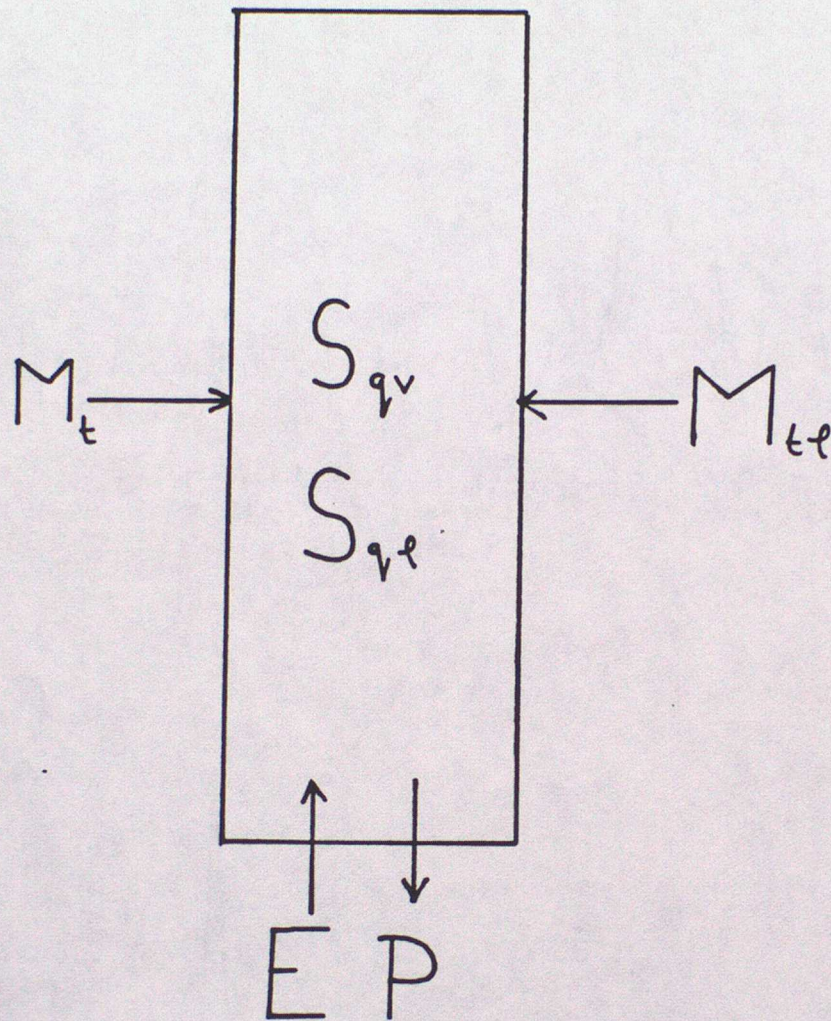
Figure 8.4 Schematic of fluxes of water vapour and liquid water into..an atmospheric column, together with corresponding storage terms.
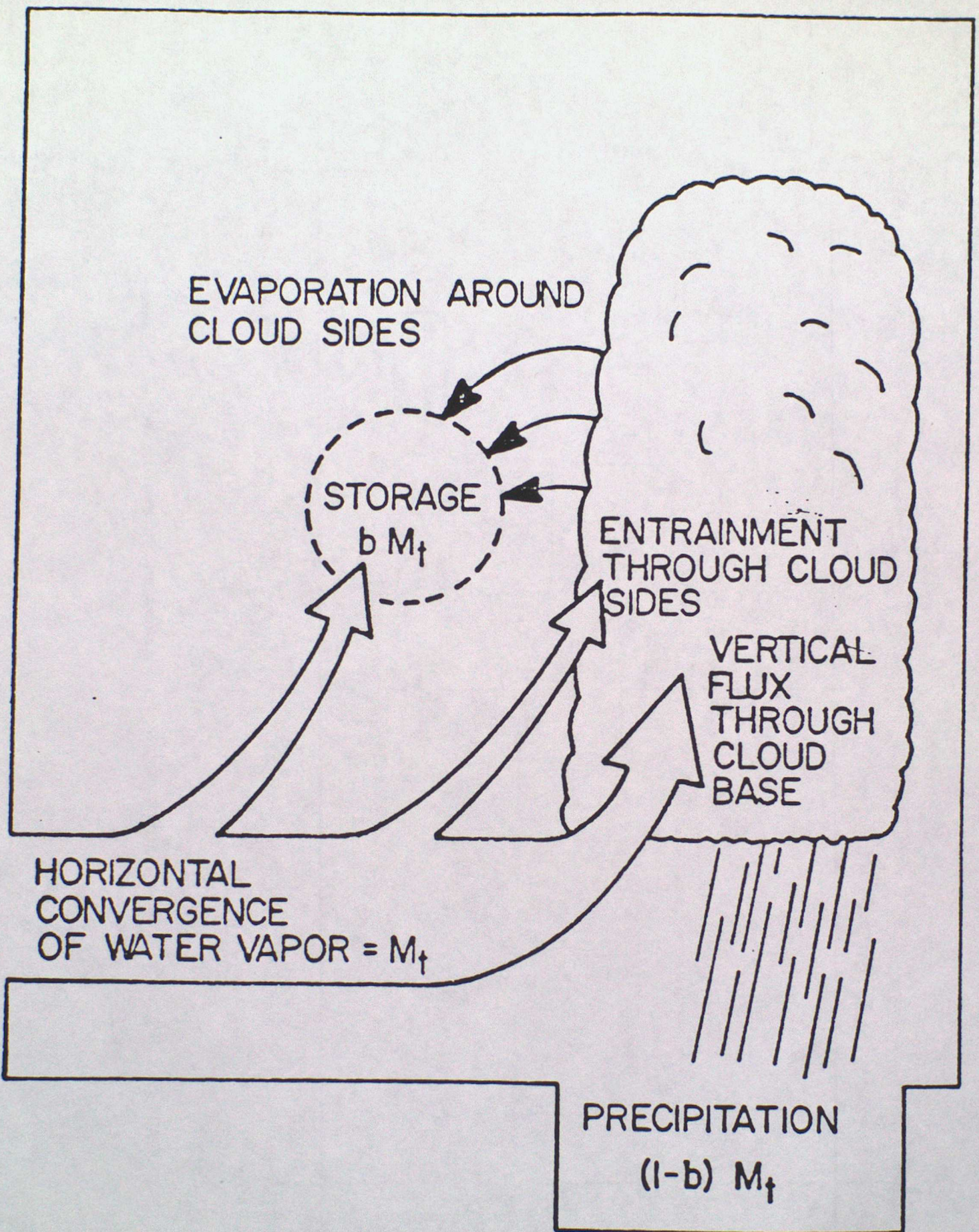
Figure 8.5 Schematic diagram showing moisture cycle in a column which contains convection (Anthes, 1977).
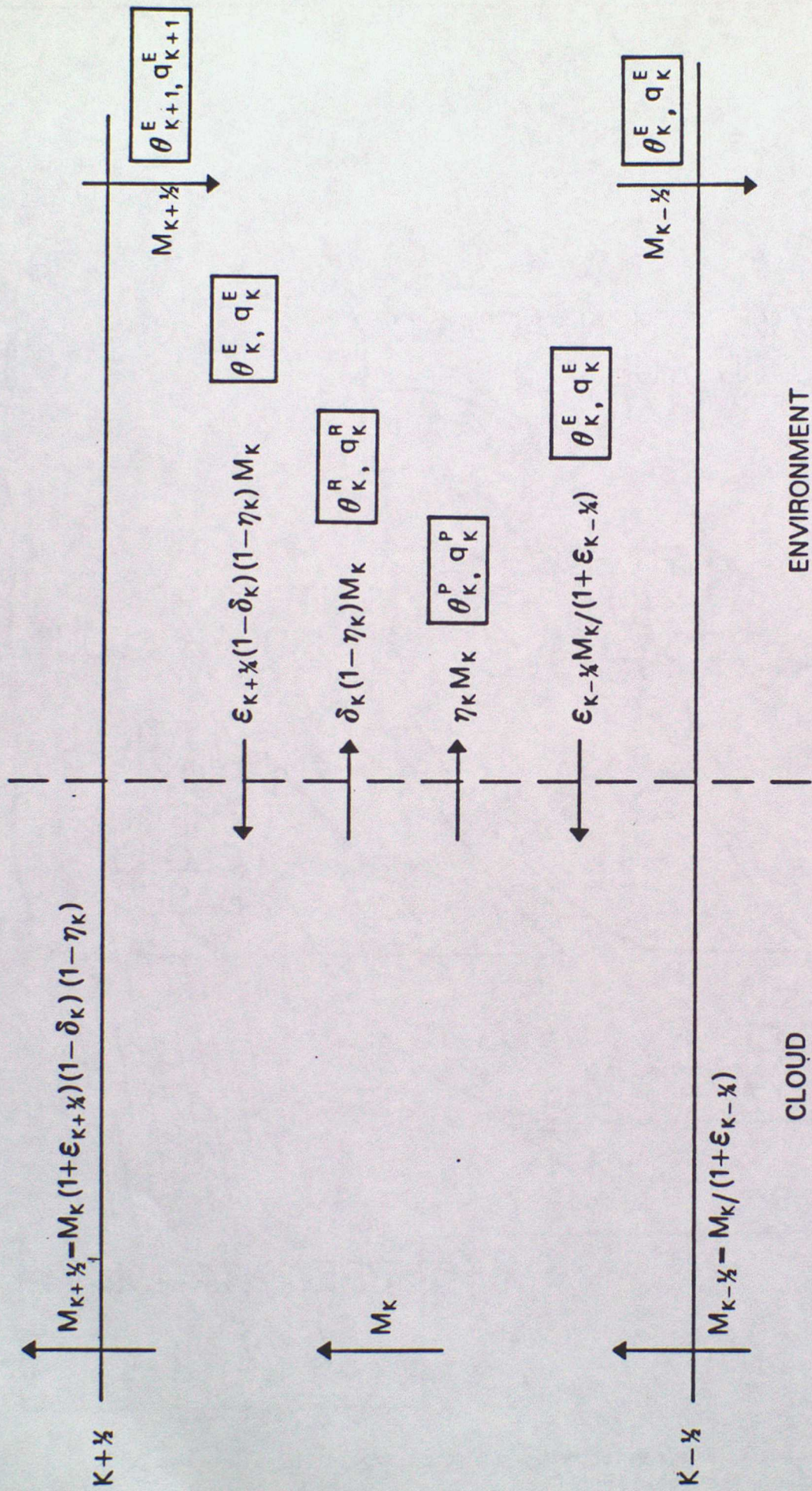
Figure 8.6 Vertical fluxes, entrainment and detrainment in the convection scheme.

.nj

Advanced Lecture 9

Parametrization of radiation in the atmosphere

Preface

     In this lecture, we shall illustrate the approach to the
parametrization of radiation in atmospheric models by describing the
scheme currently used in the Met O 20 11 layer model. Early versions
of the model used a so-called climatological radiation scheme, based
on that used in the Met O 20 5 layer model as described by Rowntree
(1975) In this scheme, atmospheric solar heating rates are
interpolated from values tabulated at 200 mb intervals as a function
of latitude (at 10 degree intervals) and season, as are surface solar
heating rates. Longwave fluxes are derived from the modelled
temperatures and appropriate long wave cooling coefficients (specified
as a function of season, latitude and height), total column
emissivities (specified as a function of season and latitude) and
surface radiative exchange coefficients which are a function of
latitude only. This scheme continues to be used in the course mesh
operational forecasting model.

     Although such climatological schemes are computationally
efficient, they do, however have several drawbacks for the reasons
outlined below and the Met O 20 11 layer model now incorporates an
"interactive" radiation scheme, as does the fine-mesh operational
model. The notes which follow are directly drawn from the 11 layer
model handbook (Slingo, 1985), and were compiled by A. Slingo, A.
Darlington, J.M. Slingo and R.C. Wilderspin. Note that equation,
heading and figure numbers have been left as in the handbook and are
therefore inconsistent with the rest of the set of lecture notes here.

4.1 Introduction

Although climatological radiation schemes (such as that described by Rowntree (1975)) are computationally economical, they have several drawbacks. Firstly, they assume the specific humidities and cloud amounts to be fixed in time and are thus unsatisfactory for simulating a climate substantially different from that for which the assumed humidities and clouds are valid. For monthly or seasonal predictions this may not be a serious criticism, although how important time variations are on this scale is still unknown since there may be important feedback mechanisms involving clouds. Secondly, climatological radiation schemes are unsuitable for assessing the effects of environmental changes, whether natural or man-made, since they are unable to respond to such things as changes in humidity and cloud distributions caused by changes in the circulation patterns.

It is thus clear that there is a need for an interactive radiation scheme which is not constrained by parameters based on present day climate. Another important feature of interactive schemes, lacking in climatological schemes, is their ability to interact with humidity and cloud distributions and thus predict the form of the feedback mechanisms involved. Experiments to assess the effects of increasing CO_2, for example, require an accurate radiation scheme to incorporate its effect on the fluxes, quite apart from the effect of radiation on the simulations.

The most important advantage of interactive schemes over climatological schemes is probably their capacity to interact with clouds predicted from model variables. For climatic change studies this feedback mechanism is of the highest importance since any long term increase or decrease in cloud cover, resulting in an enhancement or reduction of global

albedo, can substantially alter the energy balance of the earth-atmosphere
system and thereby the climate. Interactive clouds may also play a
significant role in forecasting for periods of a few days or weeks since
they affect not only the atmospheric heating through reflection, absorption
and emission of radiation but also the surface balance through modification
of the shortwave and longwave fluxes reaching the surface. Changes in the
horizontal and vertical distribution of cloudiness can therefore alter
horizontal temperature gradients and atmospheric stability and thus affect
circulation patterns.

4.2 Basic features of the scheme

One of the main factors determining the complexity of a radiation
scheme is the number of cloud layers. If random overlap of clouds is
assumed then the number of possible paths of the solar beam from the top of
the atmosphere to the ground is given by 2^n where n is the number of cloud
layers. Results from GATE suggested that even to begin to describe a cloud
field adequately it would be necessary to divide clouds into four groups
-low level, medium level, high level and convective. Bearing in mind that
the complexity of the scheme increases rapidly with the number of clouds, a
scheme was designed (Walker 1977) which would allow for three layer clouds
and a convective tower (Figure 1.1). The layer clouds are assumed to be
one sigma layer in thickness, but the convective cloud may occupy more than
one sigma layer. The clouds overlap randomly in the vertical, except that
where layer and convective clouds are present at the same level then the
overlap of the layer clouds occurs only in the clear air, after allowing
for the convective cloud. As a first approximation, convective cloud is
pictured as a vertical column with no reflection or interaction by the

sides with the surrounding cloud or air. Any shortwave radiation entering the cloud is assumed to pass straight through, after attenuation by the cloud, and emerge at the cloud base.

Three radiatively-active gases (water vapour, ozone and carbon dioxide) are considered in calculating the radiative heating rates. The water vapour mass mixing ratio (q) is of course a basic model variable, but amounts of the other two gases are prescribed. Ozone mixing ratios above 200 mb are obtained by linear interpolation from climatological zonally-meaned values for 40 mb layers (Bolton 1977) and are updated monthly when the model is run in annual-cycle mode. A minimum ozone mass mixing ratio of 10^{-8} g/g is imposed for each of the 11 layers. The mass mixing ratio of carbon dioxide (CO_2) is taken to be 4.9×10^{-4} throughout the model, corresponding to 323 parts per million by volume (ppmv).

The radiation scheme is essentially divided into two parts; short-wave and longwave. It is possible to do this since there is very little overlap in terms of wavelength between the incoming solar radiation and the outgoing terrestrial radiation. In each part, the fluxes are calculated at the layer boundaries (Figure 1.1) and at the end of the subroutine the two contributions are added. The downward flux is subtracted from the upward flux to give the net flux F. The heating rate of layer k is then given by;

$$\frac{\partial T_k}{\partial t} = -\frac{g}{C_p} \frac{\Delta F}{\Delta p} = \frac{g}{C_p} \frac{(F_{k+1/2} - F_{k-1/2})}{P_* (\sigma_{k+1/2} - \sigma_{k-1/2})} \qquad (4.1)$$

and at the surface the heating rate is

$$\frac{\partial T_*}{\partial t} = \frac{F_*}{H} \qquad (4.2)$$

where H is the thermal capacity of the surface (as in equation 3.5).

4.3 Treatment of Shortwave Radiation

4.3.1 Incoming radiation

The solar constant (the energy received from the sun on unit area exposed normally to the sun's rays in the absence of the earth's atmosphere at the mean sun–earth distance $\bar{r}$) is taken to be 1373 Wm^{-2} (Neckel and Labs 1981). For computational efficiency, the model uses a 360–day year, in which each month is 30 days in length (Slingo 1982). The earth's orbit is illustrated in Figure 4.1, where various quantities are defined. Let time ITD be measured in days from the beginning of the year (which is 0000 GMT on 1 January). Perihelion occurs when ITD = τ. The Mean anomaly M is given by;

$$M \quad = \quad \frac{2\pi}{T} \ (ITD - \tau) \tag{4.3}$$

where T is the number of days in the year, here taken to be 360. The True Anomaly v is given by the Equation of the Centre;

$$v = M + (2e - \frac{e^3}{4}) \sin M + \frac{5}{4} e^2 \sin 2M + \frac{13}{12} e^3 \sin 3M + \ldots \tag{4.4}$$

where e is the eccentricity of the earth's orbit. The incoming solar radiation at the top of the atmosphere on day ITD is then approximated by;

$$S \ (ITD) = S_O \left[\frac{1 + e \ (\cos v)}{(1 - e^2)} \right]^2 \tag{4.5}$$

To determine the incoming radiation at any given location the solar zenith angle must be found. Firstly, the solar declination δ is calculated;

$$\sin \delta = -\sin \epsilon \sin (v + w) \tag{4.6}$$

where ϵ is the obliquity of the ecliptic, which is the angle between the earth's spin axis and the axis of its orbit around the sun. In the above equations the orbital constants have the values $\tau = 3.2$ days, $e = 0.0167$, $\epsilon = 23.44°$ and $w = 102.5°$. The solar zenith angle ζ at latitude θ, longitude λ (increasing eastwards) and at model time t (measured in hours from 0000 GMT) is given by;

$$\cos \zeta = \cos\theta \cos\delta \cos\Omega - \sin\theta \sin\delta \qquad (4.7)$$

where $\Omega = \lambda + \pi \dfrac{(t-12)}{12}$ is the hour angle of the sun (e.g. Paltridge and Platt 1976). This formulation assumes that on the Greenwich meridian the sun is due south each day at 1200 GMT (i.e. the equation of time is always zero, which is a reasonable approximation).

Since the radiation scheme is called only every few hours rather than every timestep, a mean value of $\cos \zeta$ is required in order to obtain an accurate estimate of the incoming solar radiation over these hours. The hour angles for sunrise and sunset are needed for this calculation since $\cos \zeta$ cannot take negative values. The hour angle for sunset (Ω_S) is given by:

$$\Omega_S = \cos^{-1} (\tan\theta \, \tan\delta) \qquad (4.8)$$

and the mean cosine of the zenith angle between hour angles Ω_1 and Ω_2 by:

$$\overline{\cos\zeta} = \int_{\Omega_1}^{\Omega_2} \frac{(\cos\theta \cos\delta \cos\Omega - \sin\theta \sin\delta)d\Omega}{\Omega_2 - \Omega_1}$$

$$= \frac{\cos\theta \cos\delta (\sin\Omega_2 - \sin\Omega_1) - \sin\theta \sin\delta (\Omega_2 - \Omega_1)}{\Omega_2 - \Omega_1} \qquad (4.9)$$

provided that $\cos \zeta$ is always positive. If the time period in question spans the hour of sunset, for example, then $\overline{\cos \zeta}$ is given by:

$$\overline{\cos\zeta} = \int_{\Omega_1}^{\Omega_S} \frac{(\cos\theta \cos\delta \cos\Omega - \sin\theta \sin\delta)d\Omega}{\Omega_2 - \Omega_1} \qquad (4.10)$$

9.5

Similar integral limits are required to deal with sunrise.

The incoming radiation used by the scheme at any location is thus $\overline{S(ITD)}$ times $\overline{\cos\zeta}$.

Rayleigh scattering from the air molecules is parametrized very simply by reducing the incoming radiation by 3%. It is important to note that as a consequence this contributes about 10% to the globally-averaged flux reflected back to space by the model.

4.3.2 Gaseous absorption

The absorption by the radiatively-active gases and the absorption and reflection by clouds and the surface are treated in a single spectral band. The absorptivity curves for water vapour, ozone and carbon dioxide were taken from Manabe and Möller (1961) and are illustrated in Figure 4.2. In reality, the absorptions take place in different spectral regions, so the total absorption in such a scheme is simply the sum of that from each gas. The absorption of the incoming radiation down to layer boundary $j+1/2$, say, is calculated as a function of the total effective amount of absorber $u_s(o, j+1/2)$ from the top of the atmosphere to that level;

$$u_s(o, j+1/2) = \int_{o}^{u_{j+1/2}} \left[\frac{p}{P_o} \right]^\alpha du \approx \sum_{k=1}^{j} u'_k \qquad (4.11)$$

where $du = \rho_{gas} dz = m\rho_{air} dz = m\, dp/g$ and m is the mass mixing ratio of the gas. The term in brackets is the pressure scaling factor which takes account of the dependence of the absorption on pressure (e.g. Houghton

1977, page 140), p_0 is standard pressure (1013.25 mb). The scaling is only applied for water vapour, for which $\alpha = 0.9$. No temperature dependence is included.

$$u'_k = \frac{m_k}{g} \int_{P_{k-1/2}}^{P_{k+1/2}} \left[\frac{p}{p_0} \right]^\alpha dp = \frac{m_k}{g} p_* \left[\frac{p_*}{p_0} \right]^\alpha \int_{\sigma_{k-1/2}}^{\sigma_{k+1/2}} \sigma^\alpha d\sigma \quad (4.12)$$

$$= m_k \ p_* \left[\frac{p_*}{p_0} \right]^\alpha \frac{10}{g} \frac{1}{(1+\alpha)} \left[\sigma_{k+1/2}^{(1+\alpha)} - \sigma_{k-1/2}^{(1+\alpha)} \right] \quad (4.13)$$

Where u'_k is in gcm^{-2}. Note that the mass mixing ratio m_k is taken to be constant within layer k. The term $(p_*/p_0)^\alpha$ is approximated as 1.01325, but this is clearly incorrect over high topography. This will be corrected in future versions of the scheme.

For the direct beam, the scaled pathlength u_s is multiplied by a magnification factor M, to allow for the greater amount of atmosphere traversed when the zenith angle ζ increases. Houghton (1963) has expressed M in the following way;

$$M = \left[1 + \frac{h}{a} \right] \left[\frac{2h}{a} + \cos^2 \zeta \right]^{-1/2} \quad (4.14)$$

where a is the radius of the earth and h is a height which is representative for ozone absorption (taken to be 25 km). This formula takes account of the curvature of the atmosphere; for a plane-parallel atmosphere M would simply be sec ζ.

For diffuse radiation, defined as any radiation reflected by the surface and clouds or transmitted through clouds, the scaled pathlength is multiplied by a diffusivity factor (taken to be 1.67, see Liou 1980). This

allows the absorption of isotropic radiation to be calculated to a good
approximation without the need for an explicit integration over zenith
angle.

4.3.3 Clouds

The effect of clouds on the solar beam is shown in Figure 4.3 for a
typical cloud configuration. During its passage through the atmosphere the
beam is progressively split into five components; the direct beam (D)
through the clear air and the four diffuse beams (B1, B2, B3 and B4), one
from each cloud. The calculation of the contributions to the flux at any
level is somewhat involved as it is necessary to consider all possible
configurations of the convective tower with respect to the layer clouds.
The basic building block is simple, however, and may be understood by
considering the following example. The downward flux of solar radiation at
level $k+1/2$, below a single cloud layer occupying layer j is given by;

$$S_{k+1/2} = (1-c_j) \left[S(ITD) - A_{k+1/2}^{clear} \right] \cos \zeta + c_j T_j \left[S(ITD) - A_{k+1/2}^{cloudy} \right] \cos \zeta \quad (4.15)$$

where c_j is the cloud amount and T_j the cloud transmissivity. The
absorption of the clear (i.e. direct) beam and of the cloudy (i.e.
diffuse after encountering cloud top) beam are;

$$A_{k+1/2}^{clear} = S(ITD). a \{ M. u_s (o, k+1/2)\} \quad (4.16)$$

$$A_{k+1/2}^{cloudy} = S(ITD). a \{ M.u_s (o, j-1/2) + 1.67 u_s (j-1/2, k+1/2) \} \quad (4.17)$$

where a represents the combined absorption from the radiatively-active
gases.

The treatment of reflection at the earth's surface is also simple with the assumption that reflected radiation is isotropically scattered. The increased absorption at the surface as a result of multiple reflections between clouds and the surface has also been included. The mean reflectivity $\bar{R}$ of the clouds as seen from the surface is calculated by weighting each cloud reflectivity R_i by the amount of solar flux S_i reaching the surface from that cloud. Figure 4.4 shows how the terms build up as the number of reflections increases. The infinite series obtained can be expressed in the following way;

$$\alpha_{eff} = \alpha \, (1 - \bar{c} \, \bar{R}) \, / \, (1 - \alpha \, \bar{c} \, \bar{R}) \qquad (4.18)$$

where α_{eff} is the effective surface albedo, α the value for clear skies and $\bar{c}$ and $\bar{R}$ are given by;

$$\bar{c} = 1 - \prod_{i=1}^{4} (1 - c_i) \qquad\qquad \bar{R} = \sum_{i=1}^{4} R_i \, c_i \, / \, \sum_{i=1}^{4} c_i \qquad (4.19)$$

where c_i is the amount of cloud type i.

This decrease in surface albedo can be important in cases with large amounts of low cloud which has a high reflectivity. For example, consider the extreme case of a full cover of stratus with reflectivity of 70% over snow-covered ground with an albedo of 80%. Consideration of multiple reflections decreases the albedo to an effective value of 55%. No allowance has been made for the additional absorption occurring in the atmosphere and the cloud due to multiple reflections nor for multiple reflections between two cloud layers.

The scheme includes the additional atmospheric absorption of the beams reflected from cloud and the earth's surface. As a first approximation, the reflected beams are assumed to pass to space with no further interactions with other clouds. Even with this assumption the treatment of

the reflected beam is fairly complex. Since absorption is a cumulative process and dependent on the amount of energy already extracted from that part of the spectrum, it is necessary to know the total pathlength travelled by the beam before and after reflection at the cloud or surface. This requires knowledge of what fraction of the beam, incident on the reflecting surface, has come from clouds above, i.e. at what stage in its passage through the atmosphere the beam had become diffuse.

The shortwave radiative properties of clouds are dependent on a large number of cloud parameters such as thickness and shape, liquid water content and drop size distribution, as well as on external parameters such as the wavelength of the incident radiation and the solar zenith angle (e.g. Welch et al. 1980). It is theoretically possible to determine the gross parameters of total reflectivity, transmissivity and absorptivity by using results from Mie theory and multiple-scattering calculations. However, it is difficult enough to predict the cloud amount from the model variables without additionally trying to model the above cloud parameters. The simplest approach was therefore followed when the radiation scheme was developed, in which the radiative properties are pre-set for each cloud type using typical observed values, as listed in Table 4.1.

TABLE 4.1 CLOUD SHORTWAVE PROPERTIES ASSUMED IN THE SCHEME

CLOUD TYPE	REFLECTIVITY	TRANSMISSIVITY	ABSORPTIVITY
HIGH	0.2	0.75	0.05
MEDIUM	0.6	0.3	0.1
LOW	0.6	0.3	0.1
CONVECTIVE	0.6	0.3	0.1

Given the importance of cloud-radiation interaction in modelling studies, the use of fixed cloud radiative properties is probably too crude an approximation (e.g. see Somerville and Remer (1984) and references therein). Three important effects should be considered. Firstly, the cloud radiative properties are strong functions of the total liquid water path (for a given cloud thickness and shape). The liquid water path could be parametrized from the temperature and humidity fields or held as an additional model variable (see chapter 1). Secondly, the properties depend on the solar zenith angle with, for example, the reflectivity increasing as the zenith angle increases (Liou 1976). Thirdly, the properties depend strongly on the incident wavelength, as do the surface properties (e.g. see Figure 1b of Shine et al (1984)). It is probably impractical to include the spectral detail in schemes such as that of Slingo and Schrecker (1982), but it should be possible to use, say, up to four sub-intervals (Stephens 1984). Further development of the present scheme along the above lines is not planned, however, as the intention is to replace it with a version of the scheme used in the ECMWF model (Louis 1984), which lends itself more easily to these and other improvements.

4.3.4 Surface albedos

In the original version of the scheme, the shortwave surface albedos for clear skies were 0.06 (sea), 0.2 (land), 0.5 (snow-covered land) and 0.8 (sea-ice and land-ice. Antarctica and Greenland are in the latter category). With the exception of sea and land-ice, these have been changed to incorporate more realistic values.

Firstly, the global dataset of land cover and soils data compiled by M. F. Wilson and Henderson-Sellers (1985) was used to create a geographical distribution of the snow-free land albedo α_L. This dataset has formed the

basis of a series of experiments to determine the sensitivity of the model
to the land surface albedo (M. F. Wilson 1984). Secondly, the albedo of
snow-covered land α_S is now a function of the snow-depth, through a
formulation similar to that employed in the 5-layer model (J. M. Slingo
1982);

$$\alpha_S = \alpha_L + 0.38 \, (\text{Snowdepth})^{1/2} \qquad\qquad (4.20)$$

where the snowdepth is measured in mm of the equivalent depth of water and
α_S is limited to a maximum value of 0.6. This is designed to take account
of the fact that as the mean snow-depth increases, not only does the snow
more completely cover any surface irregularities but also the area of the
grid box which is snow-free is likely to decrease. Finally, the sea-ice
albedo is now a function of the ice temperature, such that above 268K the
albedo drops linearly from 0.8 to a value of 0.5 at 273K. This crudely
represents the tendency for leads to open through the ice and for melt
ponds to form on the surface as the temperature increases.

Figures 4.5 and 4.6 show maps of the resulting surface albedo
distributions used for the 2.5 x 3.75 and 5 x 7.5 degree grids,
respectively.

4.4 Treatment of Longwave Radiation

Longwave radiation is absorbed and emitted by atmospheric gases,
clouds and the earth's surface. The absorption by water drops is so strong
that most clouds in the lower troposphere absorb essentially all the
incident flux and emit a flux which is similar to that for a black-body at
the cloud boundary temperature. Cloud radiative properties in the longwave
region are thus independent of wavelength for practical purposes. In
contrast, the wavelength-dependence of the absorption and emission by the
radiatively-active gases is enormously complex. This is because they have

many vibrational and rotational energy transitions which may be excited by longwave radiation. As a result, there are tens of thousands of spectral lines, grouped into a much smaller number of bands. The design of a longwave radiation scheme thus requires a judicious division of the spectrum, such that these bands and the main regions of overlap between the contributions from the various gases are represented as accurately as possible, whilst keeping the computational expense to a minimum. The original version of the scheme used in the 11-Layer Model was described by Walker (1977) and the new (i.e. the present) version by Slingo and Wilderspin (1984b).

4.4.1 Spectral intervals

Seven spectral divisions are used to represent the complex wavelength dependence of atmospheric absorption and emission. These divisions are grouped into six distinct intervals (or bands), as shown by the circled numbers 1-6 on the bottom frame of Figure 4.7. The first interval treats the far-infrared rotation band of water vapour (0-400 cm^{-1}) and the second deals with the overlap between the weaker line absorption around the 20μm window and absorption by the water vapour continuum (400-560 cm^{-1}). The continuum is so-called because the absorption coefficient varies only slowly with wavelength, as opposed to the rapid fluctuations for line absorption (Paltridge and Platt 1976). The third interval represents the triple overlap between water vapour line and continuum absorption and the well-known 15μm band of CO_2 (560-800 cm^{-1}). The fourth (900-1100 cm^{-1}) and fifth (800-900 plus 1100-1200 cm^{-1}) intervals cover the contributions in the 10μm atmospheric window from weak water vapour lines, the water vapour continuum and the 9.6 μm band of ozone, which is important in the stratosphere. The sixth and final interval represents the 6.3 μm

vibration/rotation band of water vapour (1200 cm^{-1} upwards). Note that the weak 10 μm CO_2 band is ignored, although in principle it could easily be included as an additional term in the fourth interval.

4.4.2 Radiative Transfer Equation

The contributions to the longwave flux are calculated separately for each spectral band. Within each band, the equations for the downward and upward longwave fluxes at pressure p are;

$$F^{\downarrow}(p) = B(o).\epsilon(o,p) - \int_{p}^{o} a(p',p) \frac{dB(p')}{dp'} dp' \qquad (4.21)$$

$$F^{\uparrow}(p) = B(p_s) + \int_{p_s}^{p} a(p',p) \frac{dB(p')}{dp'} dp' \qquad (4.22)$$

where $B(p)$ is the PLanck flux for the temperature of the air at pressure p, $B(o)$ is thus the Planck flux for the top of the atmosphere, which is assumed to be the same as that for the top model level, and $B(p_s)$ is that for the surface. This formulation assumes that the air close to the surface is at the same temperature as the surface itself, which is a reasonable approximation in calculating the fluxes. The Planck fluxes are calculated from a third-order polynomial fit to the flux in each band as a function of temperature, which was obtained by numerical integration of the Planck function using 1 cm^{-1} spectral resolution for 5K intervals from 180K to 320K. $\epsilon(o,p)$ is the slab emissivity of the atmosphere from the top down to pressure p and $a(p',p)$ is the slab absorptivity from the dummy pressure p' to p. Equations 4.21 and 4.22 are essentially the same as equations 2 and 3 of Ramanathan et al (1983), except for slight differences in nomenclature.

Equations 4.21 and 4.22 are solved numerically by a trapezoidal
rule to calculate the fluxes at the layer boundaries. The terms which
contribute to the upward and downward clear-sky fluxes at any level are
illustrated on the left-hand-side of Figure 4.8. The notation is explained
by the small diagram on the bottom right. The Planck fluxes are calculated
at the 11 atmospheric levels and the surface and are assumed to vary
linearly between these levels. The emissivities and absorptivities are
calculated for each layer on the assumption that the mass mixing ratio of
each gas is constant within the layer.

Evaluation of the integrals in these equations is complicated by the
"half-layers", denoted by asterisks on Figure 4.8, which are found at both
the upper and lower limits. The half-layers allow a more accurate
calculation of the contribution to the integrals from the layer adjacent to
the level at which the flux is required. This contribution can be large in
regions of strong absorption. The contributions from the half-layers are
calculated in a simple way to avoid excessive computation. For the
half-layers closest to the level at which the fluxes are required, the dB
term is one half that for the corresponding full layer (e.g. in the example
shown it is $0.5(B_7 - B_6)$). The absorptivity should be calculated to the
centre of the half-layer (as shown), but the version of the scheme on the
Cyber 205 approximates this as one half the absorptivity to the edge of the
half-layer. A factor of 0.25 thus appears in the program. This is
obviously incorrect in calculating the downward flux at the surface (as the
dB term does not need to be halved, so the factor should be 0.5), but the
error may be ignored as the lowest sigma layer is very thin. Similar
problems are posed by the half layers furthest from the level at which the
fluxes are required. For the half-layer adjacent to the surface, the

9.15

absorptivity should be calculated to the centre of the half layer (as denoted by the cross), but it is taken to be that to the surface itself so that this term may be calculated in the same way as those from the higher layers. Note that the half layer at the top of the model makes no contribution to the fluxes as the atmosphere is taken to be isothermal above the top sigma level.

4.4.3 Gaseous absorption

a. Overlaps

The gaseous absorptivity in equations 4.21 and 4.22 is calculated from the transmissivity $\bar{\tau}$;

$$a(p',p) = 1 - \bar{\tau}(p',p) \tag{4.23}$$

For a band in which water vapour is the only gaseous absorber (i.e. band 1 or 6), the emissivities and transmissivities are simply those for water vapour. For bands with two or more absorbers, the emissivities and transmissivities for each gas are combined by making the usual assumption that the transmissivities may be multiplied together to give the overlapped values. The first three bands of the scheme demonstrate the method. The subscripts on the following represent the separate contributions shown on Figure 4.7;

$$
\begin{aligned}
\text{Band 1:} \quad & \bar{\tau} = \bar{\tau}_1 \\
\text{Band 2:} \quad & \bar{\tau} = \bar{\tau}_2 \, \bar{\tau}_9 \\
\text{Band 3:} \quad & \bar{\tau} = \bar{\tau}_3 \, \bar{\tau}_7 \, \bar{\tau}_{10}
\end{aligned}
\tag{4.24}
$$

Now $\epsilon \approx 1 - \bar{\tau}$, so the rules for combining emissivities are;

Band 1: $(1-\epsilon) = (1-\epsilon_1)$ hence $\epsilon = \epsilon_1$

Band 2: $(1-\epsilon) = (1-\epsilon_2)(1-\epsilon_9)$ hence $\epsilon = \epsilon_2 + \epsilon_9 - \epsilon_2\epsilon_9$ (4.25)

Band 3: $(1-\epsilon) = (1-\epsilon_3)(1-\epsilon_7)(1-\epsilon_{10})$

hence $\epsilon = \epsilon_3 + \epsilon_7 + \epsilon_{10} - \epsilon_3\epsilon_7 - \epsilon_3\epsilon_{10} - \epsilon_7\epsilon_{10} + \epsilon_3\epsilon_7\epsilon_{10}$

b. Line absorption

The emissivities and transmissivities for the line absorption by water vapour, carbon dioxide and ozone are calculated from scaled absorber amounts for the given path by interpolation from look-up tables stored in the program. Pressure scaling is applied to the absorber amounts in the same way as described in section 4.3.2, the coefficient α having the value 0.9 for water vapour and carbon dioxide and 0.4 for ozone. Temperature scaling is applied only to the CO_2 data, as described layer.

The look-up tables were constructed by applying the version of the Goody (1952) random band model described by Hunt and Mattingly (1976) to the latest AFGL data tape (Rothman 1981). This gives, among other quantities, the line strength s_i and line width α_i for over 100,000 lines of various gases from a wavelength of less than 1 μm to the far infrared. A computer program was used to extract the data for each gas in each spectral interval. The line strengths and widths, listed on the tape for 296 K, were converted to values at 20 K intervals from 180 to 320 K using equations 4-7 of Hunt and Mattingly (1976). The quantities Σ s_i and Σ $\sqrt{s_i \alpha_i}$ were then calculated in sub-intervals (typically 50 cm^{-1}) within which the Planck function may be taken to be constant. In the band model program, the transmission τ in each sub-interval at 30 K intervals from 203 to 323 K and at a pressure of 1000 mb was calculated for a range of absorber amounts u from 10^{-10} to 10^2 g cm^{-2} in half-decade intervals. The band model approximation to τ in a direction $\cos^{-1} \mu$ to the normal is;

$$\tau = \exp \left\{ - \frac{c_1 \, u}{\mu} \left(1 + \frac{c_2 u}{\mu}\right)^{-1/2} \right\} \tag{4.26}$$

where $C_1 = \sum_{i=1}^{M} s_i / \Delta\nu$ and $C_2 = \left[\frac{1}{2} \sum_{i=1}^{M} s_i \sum_{i=1}^{M} (s_i \, \alpha_i)^{1/2} \right]^2$

M is the number of lines in the sub-interval of width $\Delta \nu$. These
transmissions were integrated over zenith angle by Gaussian quadrature to
give the slab transmission τ', thus avoiding the need for a diffusivity
factor in the radiation scheme.

The slab transmissions for each gas were weighted with the Planck
function $B(w,T)$ for wavenumber w and temperature T and integrated over w to
give the mean transmissivity $\bar{\tau}_j$ and emissivity ϵ_j in each band j;

$$\bar{\tau}_j(u,T) = \int_j \tau'(w,u,T) . \frac{dB(w,T)}{dT} \, dw \bigg/ \int_j \frac{dB(w,T)}{dT} \, dw \qquad (4.27)$$

$$\epsilon_j(u,T) = \int_j (1 - \tau'(w,u,T)) . B(w,T) dw \bigg/ \int_j B(w,T) dw \qquad (4.28)$$

In the look-up tables, the emissivities and transmissivities given by
4.27 and 4.28 are stored for each term labelled 1-8 on Figure 4.7, for T =
263K only. The temperature dependence of the water vapour and ozone data
is ignored but that of the CO_2 data is included by scaling the absorber
amounts (Slingo and Wilderspin 1984b). Figure 4.9 shows curves of the
emissivity of CO_2 in the 560-800 cm^{-1} band as a function of the absorber
amount u for various temperatures T, as given by the band model (at 40 cm^{-1}
resolution). The shape of the curves, which diverge steadily with
increasing u, suggested that a reasonable approximation to the emissivity
at any temperature could be obtained by using the curve for 263 K, but in
addition scaling the absorber amounts with a temperature-dependent factor
which is itself a function of absorber amount. After some experimentation,
it was found that the following scaling of the absorber amount in each
layer, Δu, was adequate;

$$\Delta u_{SCALED} = \Delta u \cdot (T/263)^{POWER} \qquad (4.29)$$

where $POWER = 8.5 + 2 \log_{10}(\Delta u)$

where T is the layer temperature. At small Δu, POWER is forced to be zero rather than become negative. The dots on Figure 4.9 show the effective emissivities at the layer boundaries for a CO_2 concentration of 320 ppmv, obtained by using this scaling for temperatures of 203 and 323 K, which demonstrates the excellent fit to the data. Note that the dependence of the scaling on the absorber amount results in a shift of the effective emissivity curves as the CO_2 concentration is increased, but the effect on the sensitivity of the scheme to changing CO_2 amounts is very small.

c. Water vapour continuum absorption

In the original version of the longwave scheme (Walker 1977), the slab transmission for the water vapour continuum absorption was calculated from the data of Bignell (1970), taking into account the so-called e-type absorption but ignoring the dependence on temperature. The program included a large number of look-up tables of the emissivities and transmissitivies as a function of absorber amount for each of six values of the water vapour partial pressure. In the new version of the scheme these were removed and a simpler formulation substituted, which includes the strong temperature-dependence of the e-type absorption (Slingo and Wilderspin 1984b).

The distinction between emissivity and absorptivity is ignored and the transmissivity is taken to follow an exponential law, which is usually written as;

$$\bar{\tau} = \exp \left[- (k_1 u \, p + k_2 \, u \, e) \right] \qquad (4.30)$$

where u is the water vapour absorber amount (gcm^{-2}), p is pressure (atmospheres, i.e. 1013 mb) and e the water vapour partial pressure (atmospheres). The foreign broadening coefficient k_1 arises from broadening of water vapour lines by collisions with other gases. The e-type coefficient k_2 is often attributed to the dimer molecule $(H_2O)_2$. Equation 4.30 can be re-arranged to give;

$$\bar{\tau} = \exp\left[-k_1up\left(1 + \frac{k_2}{k_1} \cdot \frac{q}{0.622}\right)\right] \qquad (4.31)$$

Note that the humidity mixing ratio $q \approx 0.622\ e/p$. It is convenient to define a scaled absorber amount u_s so that we may write;

$$1 - \epsilon(p',p) = \bar{\tau}(p',p) = \exp[-k_1 u_s(p',p)] \qquad (4.32)$$

The contribution to u_s from layer k may then be written (same notation as in section 4.3.2);

$$u_k' = 1.66\ u_k\ \frac{P_k}{1013}\left(1 + \frac{k_2}{k_1}\frac{q_k}{0.622}\right) \qquad (4.33)$$

where the diffusivity factor (here taken to be 1.66) is required to calculate the slab transmissivity. Hence

$$u_k' = 1.66\ q_k\ \Delta\sigma_k\ P_*\ \frac{10}{g}\ \frac{\sigma_k P_*}{1013}\left(1 + \frac{k_2}{k_1}\frac{q_k}{0.622}\right) \qquad (4.34)$$

Now k_1/k_2 is taken to be 0.005 in all four bands which include the continuum. In addition, the treatment of the temperature dependence of k_2 given by Roberts et al (1976) is included, using their best estimate of T_0 = 1800 K for the temperature dependence parameter;

$$k_2(T) = k_2(296K)\ \exp[T_0/T - T_0/296] \qquad (4.35)$$

$$= k_2(296K)\ f_2(T) \qquad (4.36)$$

$$\text{where } f_2(T) = \exp\left[\frac{1800}{T} - 6.081\right] \qquad (4.37)$$

Hence equation (4.34) may be written;

$$u'_k = 1.671.10^{-3} \, q_k \, p_*^2 \, \Delta\sigma_k \, \sigma_k \, (1 + 321.54 \, f_2(T) \, q_k) \qquad (4.38)$$

The values of k_1 in bands 2–5 (terms 9–11 in Figure 4.7) are taken to be 0.35, 0.15 and 0.05 $g^{-1} \, cm^2 \, atm^{-1}$.

4.4.4 Clouds

Just as they do for solar radiation, clouds can have a dominating effect on thermal emission. When they are present the longwave flux to space is reduced since they block the surface flux and emit at a lower temperature. Similarly, the downward surface flux is increased since the cloud radiates at a higher temperature than the equivalent black–body temperature of the radiation from clear air. Thus from the longwave standpoint both the planet and the surface tend to warm.

The effect of a typical cloud configuration on the infrared fluxes is shown in Fig 4.10. As in the solar scheme, the upward and downward fluxes each divide into five components, one from each cloud and that through the clear air either from space or the surface. The surface is assumed to act as a black–body so that the downward flux at the ground is completely absorbed. With the exception of high cloud which has an emissivity of 0.75, all clouds are treated as perfect absorbers and emitters of infrared radiation. In the scheme a cloud is assumed to be 'active' with respect to thermal radiation only near its edges, so that as a first approximation the thermal radiation leaving through the cloud surface can be identified with the black body emission at the temperature of the cloud boundary. This assumption is clearly not valid when a cloud is no longer 'black'. Then the radiation leaving the cloud will be part transmitted and part emitted. The emitted radiation will not be representative of the black body emission

at the cloud boundary temperature since it will comprise radiation from all parts of the cloud. At present the 'greyness' of high clouds is included in the scheme merely by reducing the cloud amount and then treating the cloud as a black body. When a cloud is modelled by the scheme it is assumed to occupy a whole layer or number of layers and the temperatures of the base and top of the cloud determined by taking a mean of the temperatures of the adjacent model levels.

The terms contributing to the downward fluxes at any level below a cloud layer are illustrated on the right hand side of Figure 4.8. Note that a factor 0.5 appears in the program for the half-layer adjacent to the cloud, because for convenience the dB term is calculated for the full layer (i.e. in this example to the centre of the cloudy layer). As with the half-layer adjacent to the surface, the absorptivity is calculated to the edge of the cloud. The terms contributing to the upward flux at any level above a cloud layer are calculated in the same way.

Bignell, K.J., 1970: The water-vapour infra-red continuum. Quart. J.R.

Met. Soc., 96, 390-403.

Bolton, J.A., 1977: Monthly estimates of the mean distribution of ozone in

the atmosphere as a function of latitude. Met O 20 Technical Note No.

II/117, Meteorological Office, Bracknell.

Goody, R.M., 1952: A statistical model for water vapour absorption.

Quart. J.R. Met. Soc., 78, 165-169.

Houghton, J.T., 1963: The absorption of solar infra-red radiation by the

lower stratosphere. Quart. J.R. Met. Soc., 89, 319-331.

Houghton, J.T., 1977, The physics of atmospheres. Cambridge University

Press.

Hunt G.E. and Mattingly S.R. 1976 Infrared radiative transfer in

planetary atmospheres - I Effects of computational and spectroscopic

economies on thermal heating/cooling rates. J. Quant. Spectrosc,

Radiat. Transfer., 16, 505-520.

Liou, K.-N., 1976: On the absorption, reflection and transmission of solar

radiation in cloudy atmospheres. J. Atmos. Sci., 33, 798-805.

Liou, K.-N. 1980 An introduction to atmospheric radiation. International

Geophysics Series, 26, Academic Press.

Louis, J.-F. (editor), 1984: Research Manual 3: ECMWF Forecast Model

Physical Parametrization, ECMWF.

Manabe S. and Möller F. 1961 On the radiative equilibrium and heat

balance of the atmosphere. Mon. Weath. Rev., 89, 503-532.

Neckel H. and Labs D. 1981 Improved data of solar spectral irradiance

from 0.33 to 1.25 micron. Solar Phys., 74, 231-249.

Paltridge G.W. and Platt C.M.R. 1976 Radiative processes in meteorology

and climatology. Developments in atmospheric science, 5, Elsevier.

Ramanathan, V., Pitcher, E.J., Malone, R.C., and Blackmon, M.L., 1983, The

response of a spectral general circulation model to refinements in

radiative processes. J. Atmos. Sci., 40, 605-630.

Roberts, R.E., Selby, J.E.A., and Biberman, L.M., 1976: Infrared continuum absorption by atmospheric water vapour in the 8-12 μm window. Applied Optics, 15, 2085-2090.

Rothman, L.S., 1981: AFGL atmospheric absorption line parameters compilation: 1980 version. Applied Optics, 20, 791-795.

Rowntree, P.R., 1975: The representation of radiation and surface heat exchange in a general circulation model. Met O 20 Technical Note No. II/58, Meteorological Office, Bracknell.

Shine, K.P., Henderson-Sellers, A., and Slingo, A., 1984: The influence of the spectral response of satellite sensors on estimates of broadband albedo. Quart. J.R. Met. Soc., 110, 1170-1179.

Slingo A. 1982 Insolation calculations for a 360-day year. Met O 20 Technical Note II/184, Meteorological Office, Bracknell.

Slingo, A., 1984/1985: Simulation of the earth's radiation budget with the 11-layer general circulation model. Met O 20 Technical Note No. II/214, Meteorological Office, Bracknell. A slightly revised version appears in Met. Mag., 114, 121-141 (May 1985).

Slingo, A., and Schrecker, H.M., 1982: On the shortwave radiative properties of stratiform water clouds, Quart. J.R. Met. Soc., 108, 407-426.

Slingo, A., and Wilderspin, R.C., 1984b: Development of a revised longwave radiation scheme for an atmospheric general circulation model. Dynamical Climatology Technical Note No. 14, Meteorological Office, Bracknell.

Slingo, J.M., 1982 A study of the earth's radiation budget using a general circulation model. Quart. J.R. Met. Soc., 108, 379-405.

Somerville, R.C.J., and Remer, L.A., 1984: Cloud optical thickness feedbacks in the CO_2 climate problem. J. Geophys. Res., 89, 9668-9672.

Stephens, G.L., 1984: The parametrization of radiation for numerical weather prediction and climate models. Mon. Wea. Rev., 112, 826-867.

Walker J.M. 1977 Interactive cloud and radiation in the 11-layer model.

    Part I: Radiation Scheme. Met O 20 Technical Note II/91,

    Meteorological Office, Bracknell.

Welch, R.M., Cox, S.K., and Davis, J.M., 1980: Solar radiation and clouds.

    Amer. Met. Soc., Met. Mon., 17, No. 39.

Wilson, M.F., 1984: The construction and use of land surface information

    in a general circulation climate model. Ph.D. Thesis, University of

    Liverpool.

Wilson, M.F. and Henderson-Sellers, A., 1985: A global archive of land

    cover and soils data for use in general circulation climate models.

    J. Climatology, 5, 119-143.

SIGMA LAYER
BOUNDARIES

SIGMA LEVELS

0·0	0·02207
0·060	0·08856
0·125	0·15741
0·195	0·23047
0·270	0·31738
0·370	0·43626
0·510	0·57717
0·650	0·71772
0·790	0·84380
0·900	0·93701
0·975	0·98744
1·000	

H

M

C

L
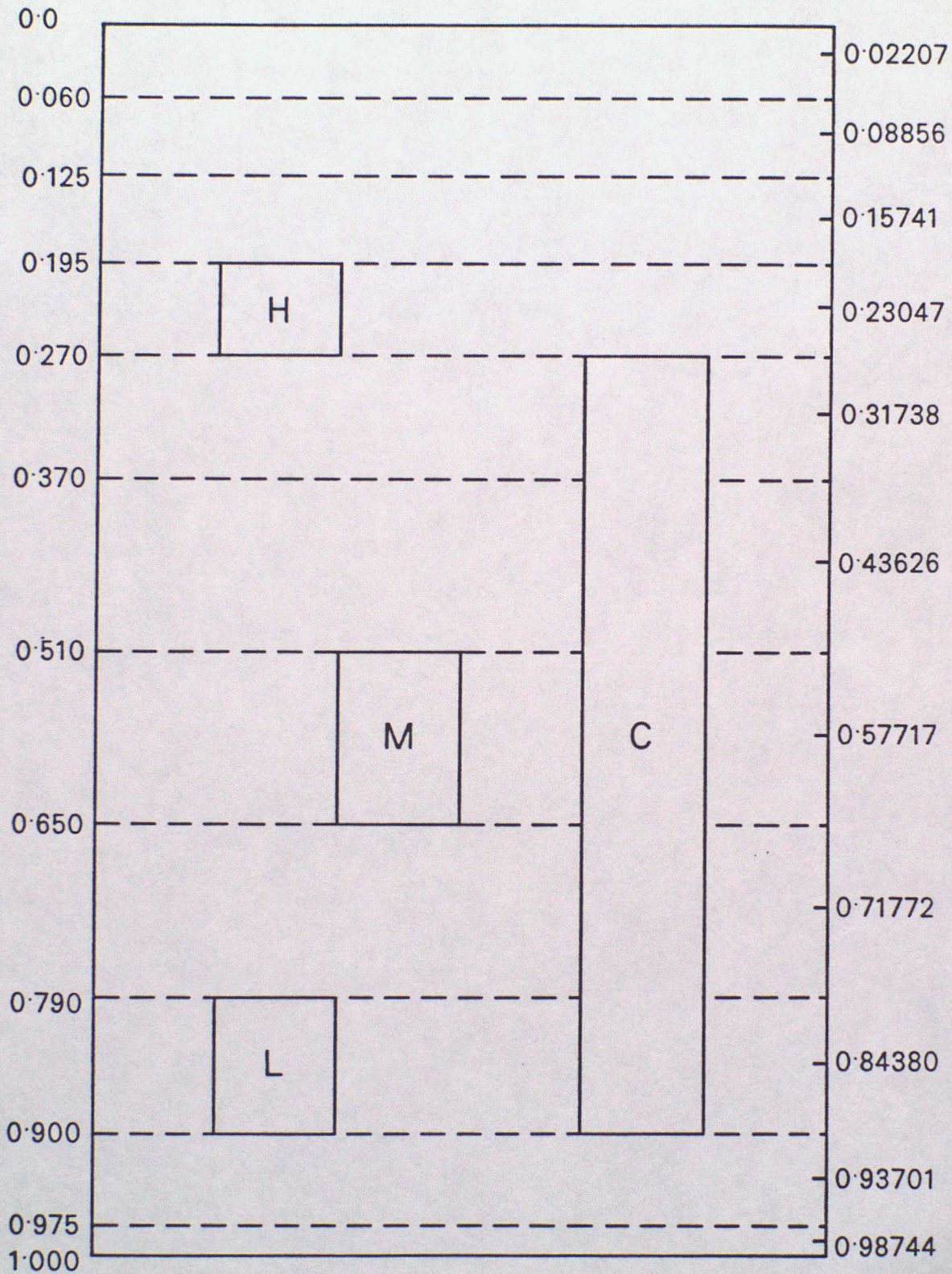
Figure 1.1 Vertical resolution of the 11-Layer Model. A possible
configuration of the High (H), Medium (M) and Low (L) layer
clouds and the convective tower (C), as used in the interactive
radiation scheme, is also shown.
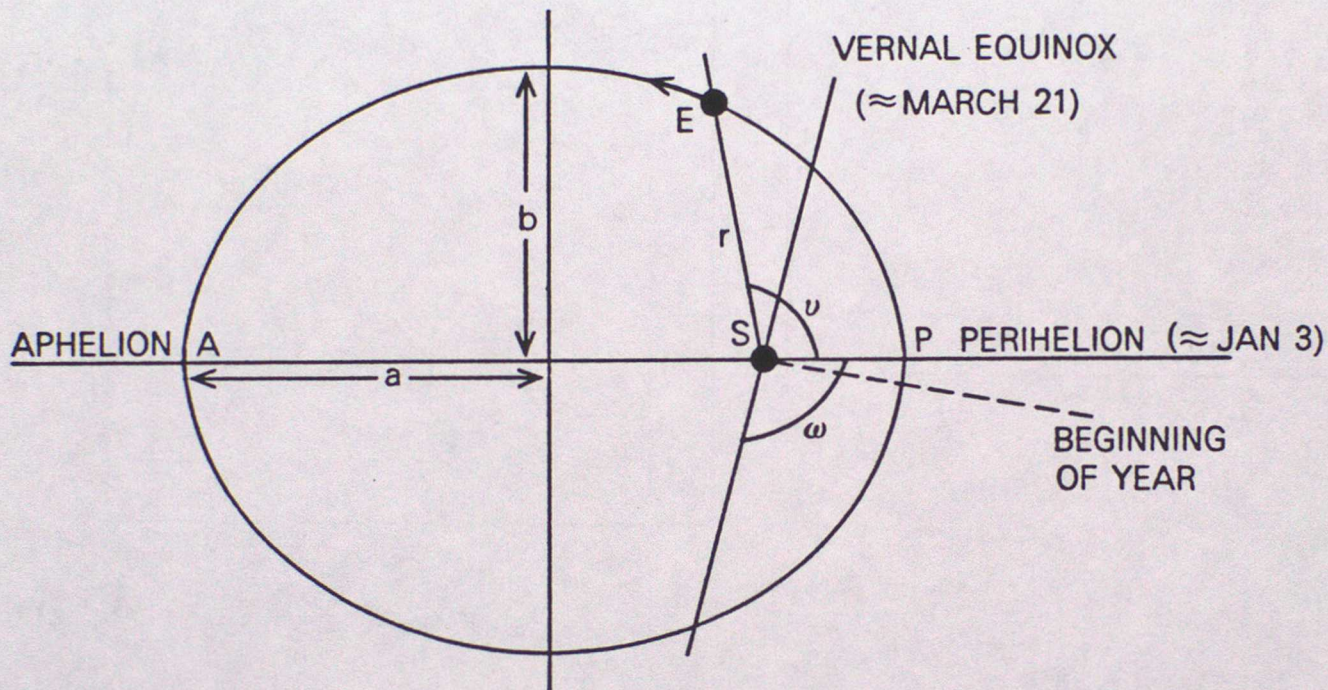
Figure 4.1 Schematic diagram of the earth's orbit. The meaning of the

symbols is as follows;

S   Sun

E   Earth

A   Aphelion (Earth furthest from Sun)

P   Perihelion (Earth closest to Sun)

a   Semi-major axis

b   Semi-minor axis

r   Length of radius vector SE

w   Longitude of perihelion. Note that this is defined such

     that the angle between perihelion and the vernal equinox is

     $(\pi - w)$.

v   True Anomaly, which is the angle around the orbit from

     perihelion.
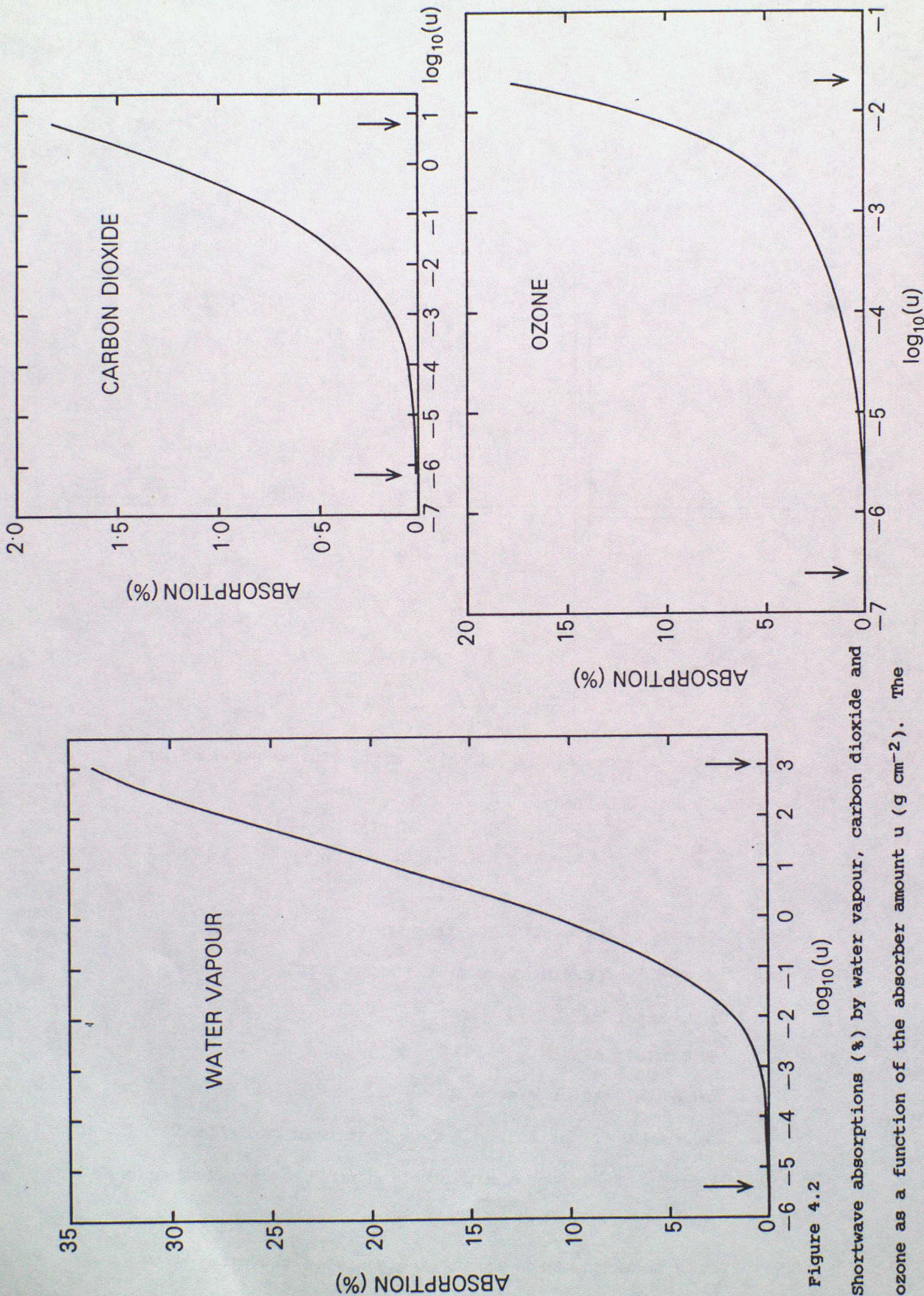
Figure 4.2 Shortwave absorptions (%) by water vapour, carbon dioxide and ozone as a function of the absorber amount u (g cm^{-2}). The vertical arrows denote the first and last entries in the look-up tables stored in the program.
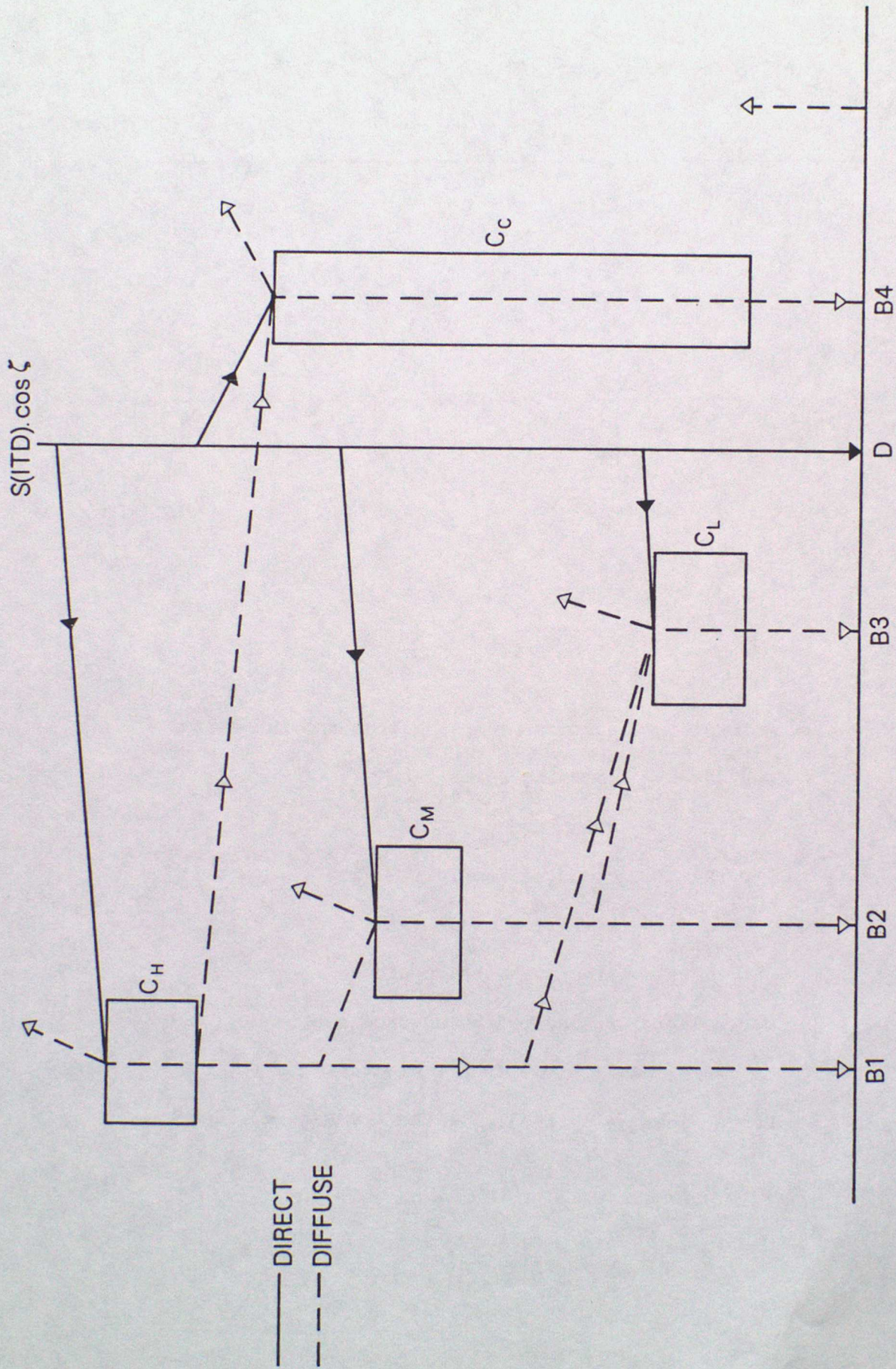
Figure 4.3 Division of the solar beam during its passage through a cloudy atmosphere.

CLOUD

$cR\alpha S$ $C^2R^2\alpha^2 S$ $C^3R^3\alpha^3 S$

S αS $cR\alpha^2 S$ $C^2R^2\alpha^3 S$

SURFACE

$(1-\alpha)S$ $(1-\alpha)CR\alpha S$ $(1-\alpha)C^2R^2\alpha^2 S$ $(1-\alpha)C^3R^3\alpha^3 S$
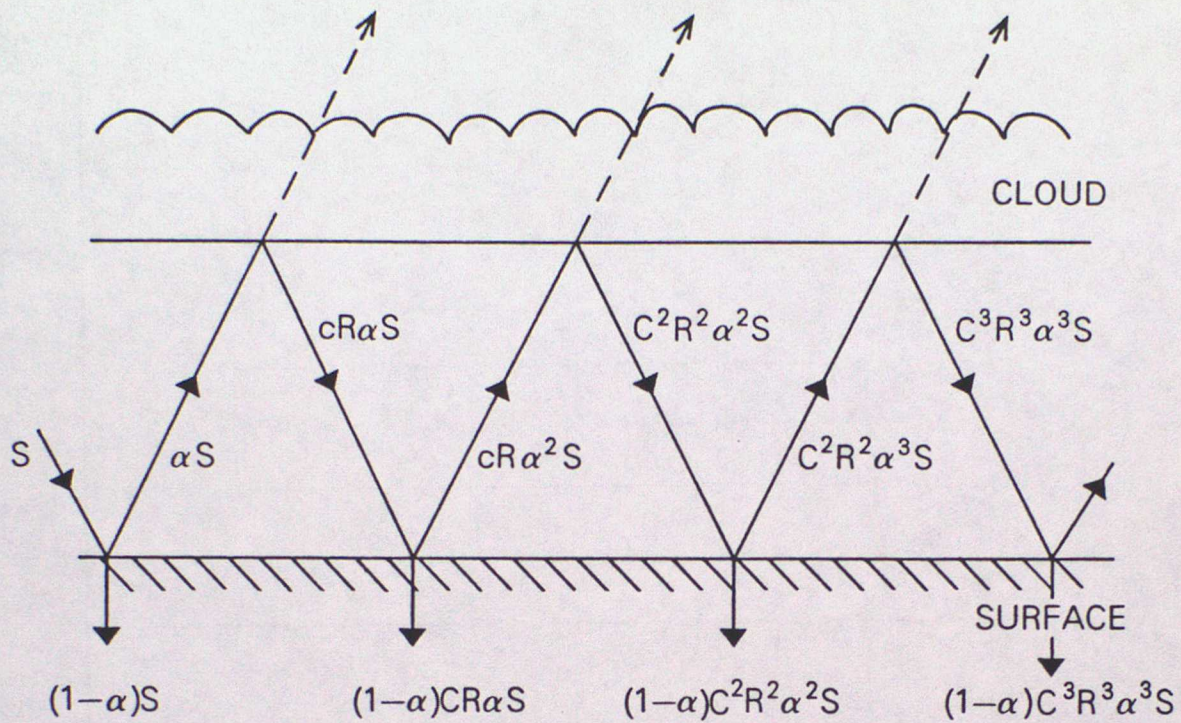
Figure 4.4 Multiple reflections between clouds and the surface.

Let S = incoming solar flux

    C = cloud amount

    R = cloud reflectivity

    α = surface albedo

    α_{eff} = effective surface albedo

Net solar flux absorbed by surface $= (1 - \alpha_{eff})S$

$$= (1-\alpha)S + (1-\alpha)\, CR\alpha S + (1-\alpha)C^2R^2\alpha^2 S + \ldots$$

Hence $(1-\alpha_{eff}) = (1-\alpha)\,(1 + CR\alpha + C^2R^2\alpha^2 + \ldots)$

$$= \frac{(1-\alpha)}{(1 - CR\alpha)}$$

Thus α_{eff} $= \dfrac{\alpha\,(1 - CR)}{(1 - \alpha CR)}$

Figure 4.5 Snow-free surface shortwave albedos (%) used in the model when
integrated on the 2.5 x 3.75 degree latitude-longitude grid.
In this dataset sea-ice is ignored, so all sea points are
allocated the value 6%.

ALBEDOS USED IN 5x7.5 GCM BY ROW/COLUMN

Figure 4.6   Same as Figure 4.5 for the 5 x 7.5 degree grid.
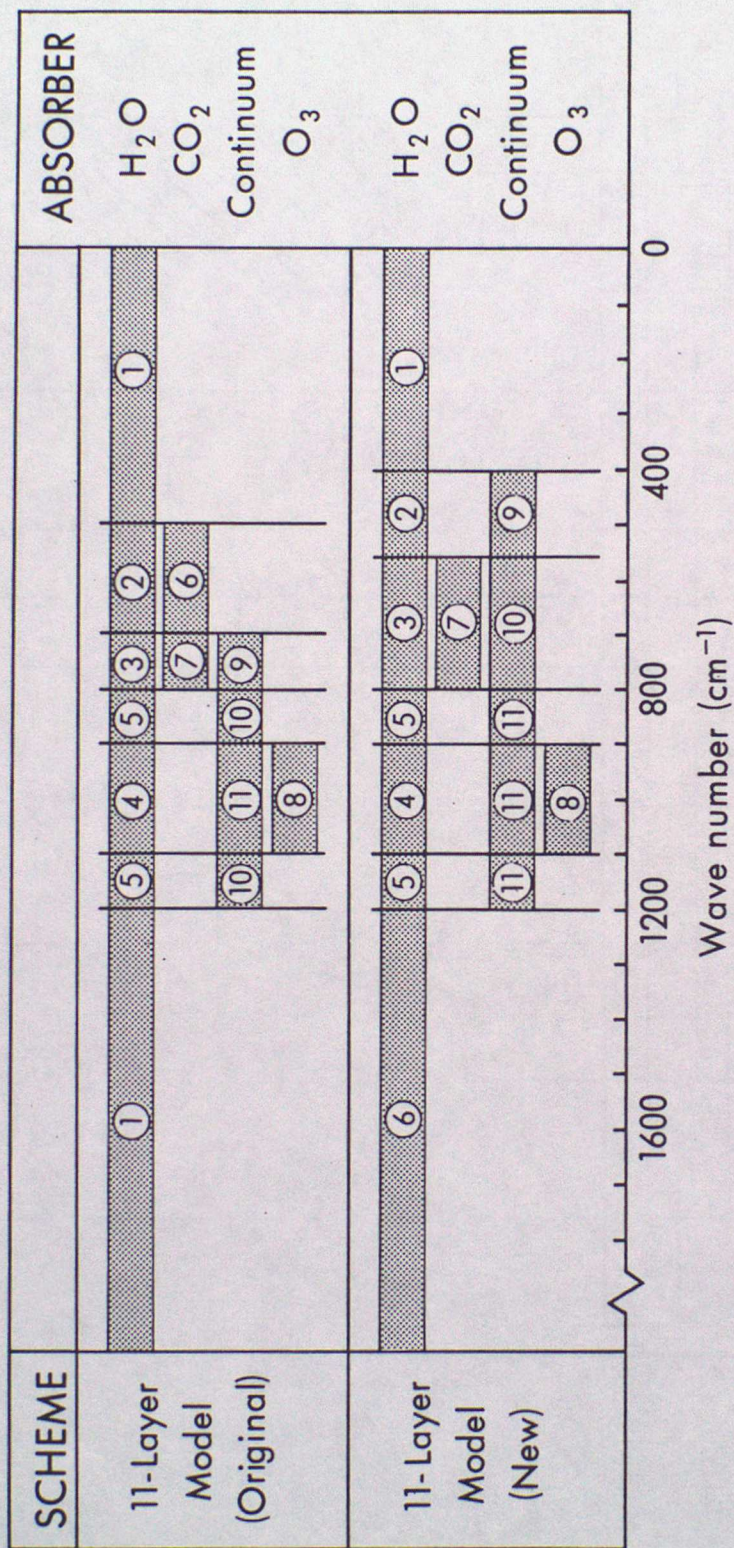
Figure 4.7 Band limits and absorbers taken into account in the original
and new versions of the 11-Layer Model longwave radiation
scheme. The numbers identify the separate contributions to the
total flux from each of the absorbers listed on the right.

CLEAR   CLOUDY

12 (T.O.A.)

B_{12}— —   11

B_{11}— —   10

B_{10}— —   9

B_9— —   8

B_8— —   7

B_7— —   *   *   +   6

*   5

B_6— —   *   NOTATION

B_5— —   4

B_4— —   + $dB(p')$ p'

                                        3

                              $a(p',p)$

B_3— —   2

B_2— —   p

                    *

$B_1 = B(p_S)$ 1 (SURFACE)

PLANCK   FIRST   INTEGRAL   HELIOS
FLUX   TERM   LEVEL
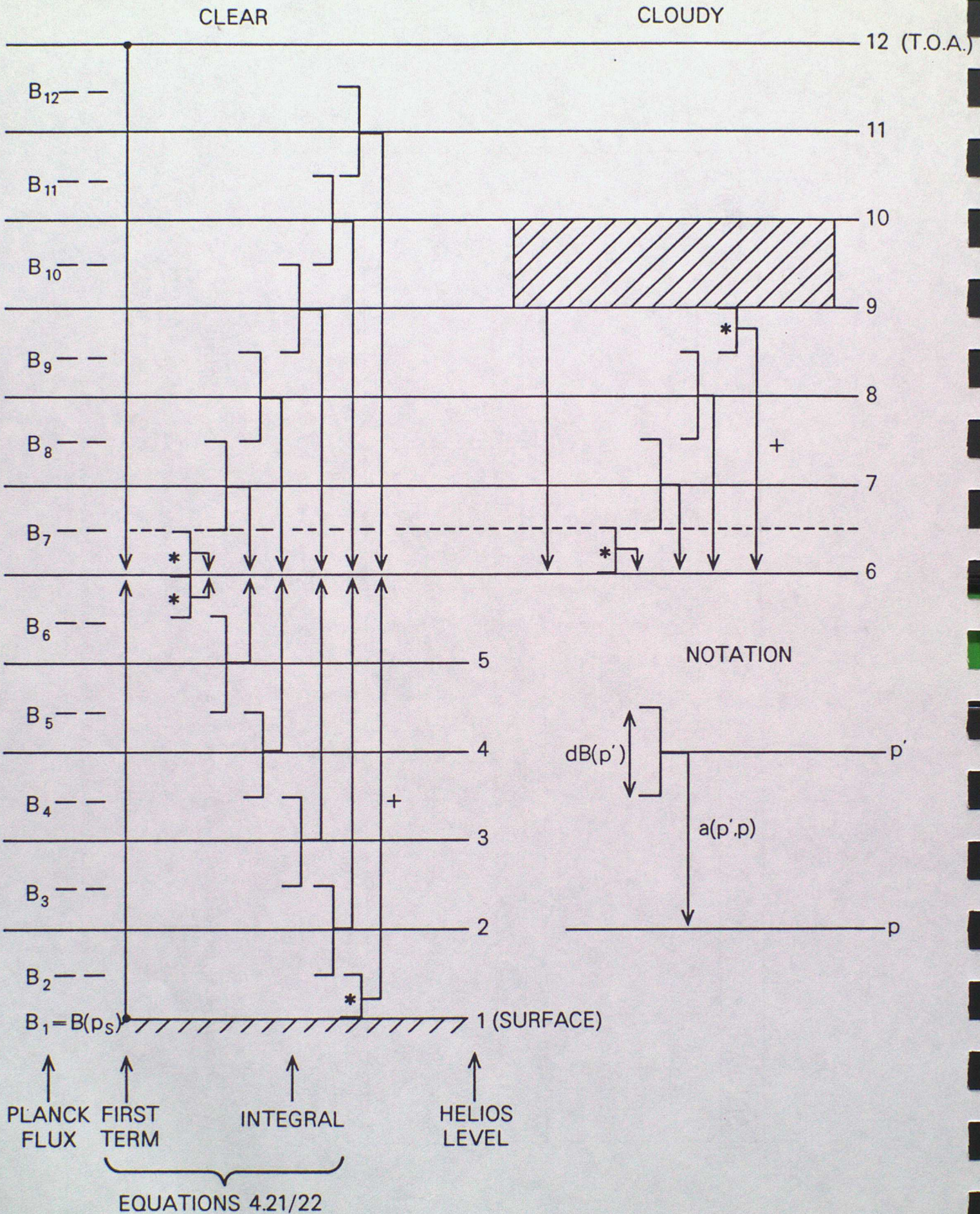
EQUATIONS 4.21/22

Figure 4.8   Illustration of how the contributions to equations 4.21 and

4.22 from each layer are added.   See text for discussion.
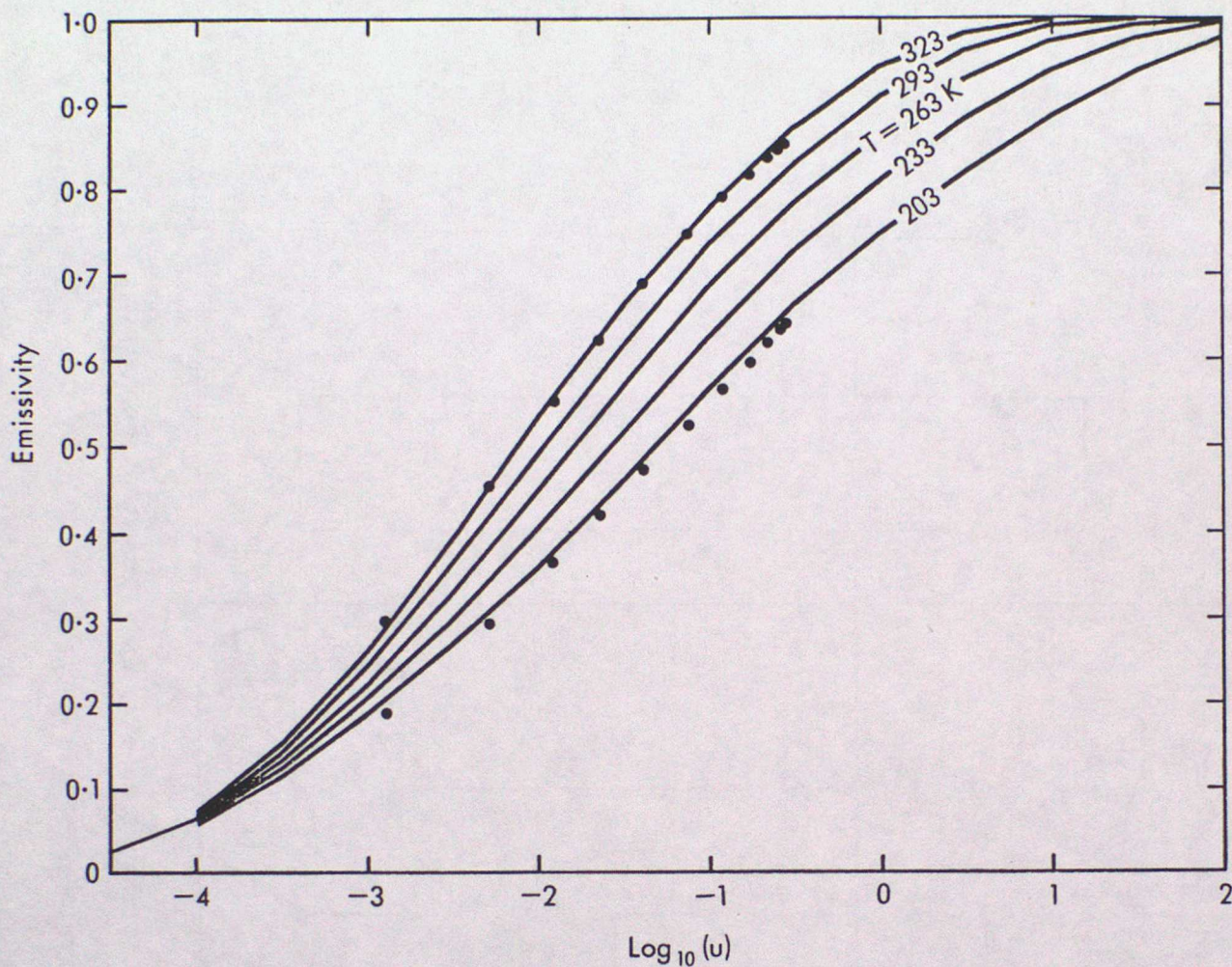
Figure 4.9 Normalized CO_2 emissivity for 560–800 cm^{-1} for various

temperatures as a function of the absorber amount u (in g

cm^{-2}). Emissivities at 203K and 323K obtained from the 263 K

data by scaling the absorber amounts according to equation

4.29 are shown as the dots.
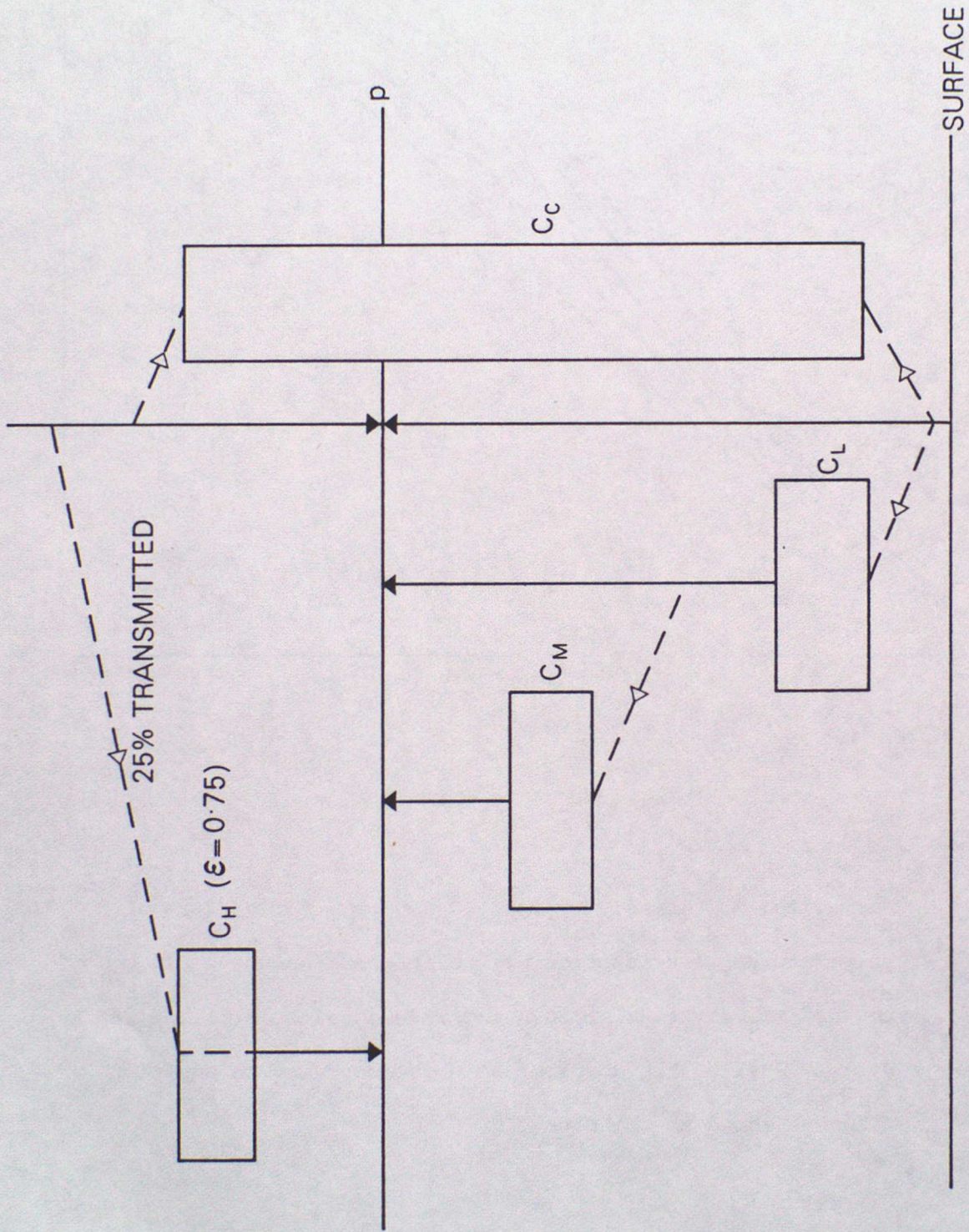
Figure 4.10 Longwave fluxes at pressure level p in a cloudy atmosphere.

Unless stated otherwise, the fluxes incident on each cloud

(shown dashed) are assumed to be absorbed totally by the cloud.

.nj

Advanced Lecture 10

Sea ice models for climate research

10.1 Introduction
            Sea ice is, of course, an integral part of the
climate system so that, with the development of global ocean and
coupled ocean-atmosphere models, it becomes necessary to include
representations of sea ice which can respond to changes in values of
the oceanic and atmospheric variables predicted within the models
themselves. Sea ice is affected (Figure 10.1) both by dynamical
processes (wind stress, water stress, sea surface slope) and
thermodynamic processes (in particular the vertical oceanic heat flux
and the surface radiation balance). These affect both the ice motion
and the amount of freezing and melting which can take place and
which,in turn, determine the thickness and extent of the ice itself.
Sea ice has a number of effects both on the climate of the polar
regions and globally, which lead to feedbacks on the ice itself. By
its presence on the sea surface, it substantially increases the
albedo of the oceanic regions where it forms, raising it from values
of 0.06 to 0.8 or more where the ice is snow covered. It also provides
a barrier to direct exchange of sensible heat and moisture between the
ocean surface and the atmosphere in polar regions and allows much
lower surface temperatures to be attained during the winter than would
otherwise be achieved, modifying both the atmospheric boundary layer
structure and the outgoing longwave flux.

        As part of the process of freezing, ice also exudes salt, so
that, for example, sea water with a salinity of 34 parts per thousand
(ppth) may freeze to give ice with a salinity of only 4 ppth. This
salt passes into the oceanic mixed layer where it enhances convection
and can lead to mixed layer deepening. During ice melt, relatively
fresh water is deposited onto the surface layer of the ocean, often in
areas far removed from the original locations of ice growth, modifying
the mixed layer structure. Both of these processes may substantially
influence the regions where deep convection may occur in the ocean.
The presence of sea ice may also markedly influence the energy
available for mixing as the ice and water move, due to friction with
the bottom surface of the ice. As illustrated in Figure 10.1, the ice
may, of course, also have a wider influence on atmospheric and oceanic
systems and, as noted above, all of these influences may result in a
variety of feedbacks between the ice and the climate system itself.

10.2 Representation of sea ice in atmospheric general circulation
models
        Global atmospheric general circulation models have, so far, only
required a relatively simple treatment of sea ice whereby it
is represented as a single slab of order a few metres constant
thickness, whose seasonally varying extent is prescribed, together
with the globally varying sea surface temperatures at the lower
boundary of the model. The Meteorological Office 11 layer AGCM, for
example, assumes (Figure 10.2) the ice to be 2m thick everywhere, with
the evolution of temperature, T_s, of the ice surface determined by the
solution of a heat balance equation of the form:

$$C_* \partial T_s / \partial t = (1-\alpha)S_o + F_L - \epsilon_L \sigma T_s^4 + H + LE + F_g \qquad (10.1)$$

Here:

$C_* \partial T_s / \partial t$ represents a heat capacity term (see lectures 2/3);

$(1 - \alpha)S_o$ is the net incoming solar radiation at the surface;

F_L, $\epsilon_L \sigma T_s^4$ represent incoming and outgoing longwave radiation respectively;

H, LE are the sensible and latent heat fluxes (taken here as positive into the surface),

and F_g represents the conduction of heat through the slab from unfrozen water at temperature T_B below. Consistent with the assumption of constant ice thickness, this takes the form

$$F_g = \frac{k_i}{h}(T_B - T_s) \qquad (10.2)$$

where k_i is the conductivity of ice and h is the ice thickness If T_s rises above the melting point of 273K, then, in the model, it is simply reset to that value.

The effects of snow cover on the ice surface are generally ignored, except through the specification of the surface albedo, , which is fairly simply specified. The Meteorological Office model takes:

$\alpha = 0.8$ for $T_s < 268K$

$\alpha = 0.5 + 0.3(273 - T_s)/5$ for $268K < T_s < 273K$ (10.3)

In essence, this is intended to represent the decrease in albedo over a grid square as melting is preferentially induced, for example, on, in the northern hemisphere, south facing ridges, with a value of 0.5 at the melting point to model the presence of melt pools on the surface. Such a representation may be less than representative for Antarctic sea ice, (Andreas and Ackley, 1982), where, in fact, melt ponds are rarely observed.

10.3 Elements of a sea ice model

In constructing a sea ice model suitable for interactive coupling to atmosphere and ocean models, a number of considerations need to be taken into account, depending on the degree of sophistication required. We list below the basic elements required to build a full sea ice model (Hibler, 1985):

1. Momentum balance

Newton's second law F = ma

$$\tau_a + \tau_w - mg \nabla H + F - mfkxu = mDu/Dt \qquad (10.4)$$

air   water   sea   internal   Coriolis

stress   stress   surface tilt   ice force   force

2. Additional components

B. Thermodynamic code + equations describing the evolution of ice thickness due to dynamic + thermodynamic effects

$$(\partial h/\partial t) = -\nabla \cdot (\underset{\sim}{u}h) + S_h \qquad\qquad (10.5)$$

$$(\partial A/\partial T) = -\nabla \cdot (\underset{\sim}{u}A) + S_A \qquad\qquad (10.6)$$

C. Ice strength – equations relating ice strength as a function of the ice thickness distribution

$$P = P_* h \exp(-C(1-A)) \qquad\qquad (10.7)$$

D. Ice rheology – equations relating ice stress to ice deformation and strength.

In the above, $\underset{\sim}{u}$ = ice velocity; P = ice strength; P_*, C are ice strength constants; h = average ice thickness per unit area; A = ice compactness; S_h, S_A are thermodynamic source and sink terms.

For climate studies, sea ice models capable of seasonal simulations over large regions are needed. As noted in WCP-26, three types of such sea ice models presently exist. They are:

(i) one dimensional thermodynamic sea ice models (Washington et al., 1976; Manabe et al., 1979), largely based on Semtner's (1976) simplification of Maykut and Untersteiner's (1971) thermodynamic model of a multiyear floe; this one dimensional model is the most commonly used model in climate studies.

(ii) Ad-hoc parametrizations of leads and possibly ice transport by simple adjustment of ice motion to avoid too much convergence. (Bryan et al., 1975; Parkinson and Washington, 1979).

(iii) Dynamic-thermodynamic sea ice models (Hibler, 1979, 1980) in which ice deformation and thickness characteristics are related to the internal stresses in the ice cover by a well defined non-linear rheology.

10.4 Thermodynamic sea ice models

Maykut and Untersteiner's (1971) model represents the most complete treatment to date of the one-dimensional thermodynamics of perennial sea ice. The model includes the effect of snow cover, the effects of salinity in determining the specific heat and conductivity of the ice, and internal heating due to penetration of solar radiation during periods when the surface is snow free. Finite difference diffusion equations govern heat transport within the ice and snow using a grid spacing in the vertical of 10 cm. The model is driven by specifying the incoming radiative and turbulent heat fluxes, oceanic heat flux, ice salinity,

snowfall and surface albedo as a function of time. Figure 10.3
compares the equilibrium temperature field (depth against time) from
the model with observed values from IGY Station Alpha during 1957-58.
Note the displacement of the time axis on the two sections. The
seasonal variation of the temperature structure is well represented as
is the overall thickness of the ice, summer ablation and thickening of
the ice layer during winter and early spring.

Whilst Maykut and Untersteiner's model gives a fairly
comprehensive representation of the thermodynamics of sea ice, it
requires substantial simplification for effective use in climate GCMs,
where storage and run time are prime considerations. Such a
simplification was developed by Semtner (1976) who showed (Figure
10.4) that the number of layers could effectively be reduced to three
(one in the snow and two in the ice, with special treatment for thin
ice (< 25 cm.) and shallow (< 15 cm.) snow layers. Temperatures in the
layers and thicknesses of the snow and ice are predicted on the basis
of fluxes across internal and external boundaries by application of
heat diffusion equations. Like Maykut and Untersteiner's model, the
surface temperature is determined by solution of the surface heat
balance equation for specified incoming fluxes such that if the
surface temperature is predicted to be greater than the melting point
(273K), it is reset to that value and surface ablation reduces the
thickness of the upper layer of snow over timestep t by an amount:

$$\Delta h_s = \frac{\Delta t (F_A - F_s)}{q_s} \qquad (10.8)$$

where F_A is the net heat flux at the surface (sum of the net solar and
l ong wave fluxes and the sensible and latent heat, F_s is the internal
heat flux in the snow layer and q_s is the latent heat of fusion of
snow. If the upper surface is snow-free, the treatment is similar,
except that a fraction I_o of the incoming solar radiation is allowed
to penetrate the ice where it is stored in "brine pockets"
(essentially as a simple heat reservoir) to be released during
freezing to keep T_s at -0.1C until the reservoir is exhausted.

At the bottom of the ice, ablation or accretion occurs,
depending on whether F_g is greater or less than F_2. The oceanic heat
flux F_g must be specified or, in coupled ocean- sea ice integrations
determined from the top layer temperature of the ocean model by, e.g,
a simple diffusion-type formula. For Semtners intercomparisons with
Maykut and Untersteiners model, which were characteristic of perennial
Arctic sea ice, a constant value of 2 Wm^{-2} was used.

Comparison of the results of the Semtner model with that of
Maykut and Untersteiner shows, for the same prescribed forcing, good
agreement in the overall description of ice characteristics. Whilst
the Semtner model does not, of course, resolve the detailed
temperature structure within the ice, surface temperatures compare
well with the Semtner model, lying closer to the Maykut and
Untersteiner model than the latter does to observed surface values,
without substantial tuning (Figure 10.5a). The predicted equilibrium
seasonal cycle of ice thickness is shown in Figure 10.5b, where Maykut
and Untersteiner's model is compared with Semtner's 3-layer model and
a simpler version, the so-called zero layer model, in which the snow
and ice layers are treated as a single slab. The figure also shows the
sensitivity of the models to prescription of the fraction of incoming
solar radiation, I_o, allowed to penetrate the bare ice surface.
Reduction of I_o from 17% to zero reduces the ice thickness by about 40

cm. overall.

In fact, when forced non-interactively, the thermodynamic models show substantial sensitivity in a number of respects. Table 10.I shows results of some non-interactive tests of Semtner's zero layer model carried out by Bottomley (1984). Here the so-called standard integration employs essentially the same external seasonally varying forcing as Maykut and Untersteiner (1971). However, both Maykut and Untersteiner and, for comparison purposes, Semtner (1976), used a value of Stefan's constant 2% higher than the accepted value. In non-interactive integrations like these, this has a substantial impact on the degree of summer melt and hence on the modelled equilibrium mean ice thickness with the result that, to retain ice depths characteristic of perennial ice in the Arctic the prescribed oceanic heat flux had to be reduced from 2 Wm^{-2} in the control integration to zero, which also gives an indication of the sensitivity of the model to this parameter.

Overall, the model (Table 10.I) shows little sensitivity to prescribed snowfall, but use of the Meteorological Office 5-layer model albedo formulation in which an albedo of 0.8 is reduced to 0.5 when the top surface is melting , substantially reduces the mean ice thickness. The standard forcing has albedos dependent on season, ranging from 0.85 or so in spring and autumn, reducing to 0.64 in July and for bare ice surfaces. There is also marked sensitivity to the imposed external surface fluxes. The 5-layer model sensible and latent heat fluxes compare well with the Maykut and Untersteiner values. However, values of incoming longwave radiation over the Arctic tended to be too low in this model, as did peak summertime values of incoming solar rasiation. As a result, use of these fluxes showed large values for ice thickness which had not come to equilibrium, even after 50 years of integration.

10.5 Interactive integrations and simple representation of ice dynamics

The sensitivity, in fact, appears to be substantially reduced when the models are run interactively. Seasonally varying coupled ocean-atmosphere-sea ice models have been run at GFDL by Manabe et al. (1979), at NCAR by Washington et. al (1980) and by Pollard (1982) at Oregon State University. All used simple thermodynamic representations of sea ice of the Semtner type, though Manabe et al. attempted to introduce a simple ice rheology based on an equation for the evolution of ice thickness of the form:

$$\frac{\partial h}{\partial t} = -\nabla(\delta_{I}\underline{V}h) + A_{h}\nabla^{2}h + \left(\frac{\partial h}{\partial t}\right)_{thermodynamic}$$ (10.9)

Here $\underline{V}$ is the predicted ocean surface current and

$$\delta_{I} = 1 \quad h < 4m$$

$$\delta_{I} = 0 \quad h > 4m$$ (10.10)

δ_{I} therefore parametrizes ice jamming which occurs when ice builds up to a given thickness. The horizontal diffusion term is included for reasons of numerical stability.

The results of all of the integrations mentioned above show similar characteristics, illustrated in Figure 10.6 by results from the paper of Washington et al. (1980). Ice thickness tends to be too low in the northern hemisphere, but with the simulated ice extent fairly well represented. An exception is the winter ice extent in the Greenland Sea which shows a substantial error. Southern hemisphere ice extents are far too low. Washington et al. put this down to the high coefficients for diffusion of heat necessary for their course resolution (5° latitude/longitude grid) ocean model, which prevents a sharp discontinuity in temperature from existing, as it does in the southern oceans, equatorwards of the ice pack. The Arctic sea ice simulation is better due to its relative isolation from the warmer seas. The Greenland Sea ice anomaly may, in fact, be due to a lack of representation of the advection of warm Atlantic water by the model in this region.

10.6 Tests of a simple representation of leads

Both Semtner's and Maykut and Untersteiner's models have the disadvantage that they do not include a representation of areas of open water (leads) in the pack and tend to become unrealistic in regions where the ice is very thin. Figure 10.7 shows results from an non-interactive integration carried out at the Meteorological Office (Cattle, 1986), of a representation of ice thermodynamics due to Hibler (1979) which has a simple representation of leads in which any ice forming in the leads themselves is assumed to instantaneously coalesce to form ice of minimum thickness to which the Semtner slab thermodynamics can reasonably be applied. Figure 10.7 shows values of grid square average ice thickness in metres and of ice compactness, the fraction of a grid square covered by ice as a function of latitude and time. A 68m constant depth mixed layer was assumed at grid points which are entirely ice free. For grid points at which ice cover is present, the ocean temperature was assumed to be at freezing point and any net heating of the leads assumed to contribute to ice melt. Net cooling of the leads results in ice formation in the manner already described. The model was forced by specifying the annual cycle of surface air temperature, humidity and wind, together with climatological values of cloudiness from which the surface forcing was calculated with reference to the predicted surface temperature in the model using bulk formulae for the turbulent transfers and the simple radiative parametrizations of Budyko (1974) and Beryland and Beryland (1952) for solar and longwave fluxes respectively. The model was forced at 2.5 degree latitude intervals, the latitudinal resolution of the Meteorological Office 11 layer AGCM. Also shown on Figure 10.7 is the ice edge from a run of the Semtner model alone (i.e. without the leads representation). In the leads model the ice edge retreats further in summer due to increased absorption of solar radiation, leading to additional ice melt, which takes place in the leads. The winter ice edge is the same in both models, primarily due to enhanced transfers of sensible and latent heat through the leads during autumn cooling. Caution must be exercised in the interpretation of these results, however, as the wintertime ice edge is largely controlled by the 0C contour in the air temperatures used to force the model.

The ice thickness contours of Figure 10.7 also show a characteristic of thermodynamic models, which tend to have the ice thickness contours increasing towards the pole. This is shown more markedly in Figure 10.8, which illustrates results from a thermodynamics only integration due to Hibler (see Hibler, 1979). By contrast the observed contours (Figure 10.9) show a marked asymmetry with respect to the pole in the Arctic Basin, with values increasing

across the basin to maximum values off the Greenland coast and Canadian archipelago. The reason for the failure of the thermodynamic models to correctly simulate this feature is, of course, the lack of a representation of ice dynamics, which are also important in the Antarctic where the pack is largely divergent.

10.7 Dynamical models - brief outline

In fact, to fully represent the asymmetry of the Arctic ice thickness field, as well as the divergence of the Antarctic ice pack, one has to go to the other end of the spectrum, away from the relatively simple models discussed so far, where all of the elements outlined in Section 10.3 above are combined. The potential of such models is illustrated in Figure 10.10a & b which shows results from an integration by Hibler (1985) which contains a comprehensive representation of the ice interaction terms in the equations of motion. Figure 10.10a shows the annual mean ice motion and 10.10b the end of December ice thickness. Note that the desired increase in ice thickness across the basin towards the Greenland coast is well represented as is the transpolar drift of ice and its exit via the Fram Strait into the Greenland Sea. Hibler's ice model and its derivatives represent the state of the art in sea ice modelling at present. Whether the quality of the forcing from existing low resolution ocean models and in coupled ocean-atmosphere models matches the degree of sophistication of the models is perhaps doubtful. The potential of Hibler's model for use in coupled model integrations has, however, been demonstrated in a coupled run of the model with a limited area version of Bryan's ocean model (Hibler and Bryan, 1984). Figure 10.11 compares the simulated ice edge for the Greenland Sea for the fully coupled model, compared to a run in which the ice model is used with a simple constant depth (slab) mixed layer model of the ocean. Note that use of the slab model results in a winter ice edge substantially further south than observed. Use of the full ocean model gives a better representation of the ice edge, which compares well with observation. The ice edge is further polewards in this integration because use of the full ocean model allows convection to take place between the surface and the deeper layers below.

A simpler dynamic-thermodynamic model than Hibler's, which includes a somewhat more sophisticated representation of leads, is that of Parkinson and Washington (1979). This model contains, however, only a very simplified account of ice interaction and so tends not to fuuly represent the features described above. As yet, this model has not been run in coupled mode with either 3-dimensional atmospheric or ocean models. Figure 10.10c & d (from Hibler, 1985) demonstrates the dangers of using simple free drift representations of ice dynamics. Such an approach appears to work quite well from the point of view of simulation of ice motion. However, as Figure 10.10d shows, use of such a model results in very high accumulation of ice in off the north Greenland coast after only one year of simulation.

10.8 Film

This presentation ends with a brief film of Hibler's model run through an annual cycle. The film was made by Ruth Preller at NORDA, the U.S. Navy Oceanographic Research and Development Agency to illustrate the potential of this model for a Polar Ice Prediction System (PIPS) for the U.S. Navy.

.nj

Advanced Lecture 10 - References

Andreas, E.L., and S.F. Ackley, 1982, On the difference in the
ablation seasons of Arctic and Antarctic sea ice. J. Atmos. Sci., 39,
pp 440-447.

Beryland, M.E. and T.G. Beryland, 1952, Determining the net long wave
radiation of the earth with consideration of the effect of cloudiness.
Izv. Acad. Nauk. SSSR ser Geofiz. No. 1.

Bottomley, M., 1984, The response of a simple thermodynamic sea ice
model to GCM forcing appropriate to perennial sea ice. Met. O 20
Tech. Note, DCTN 3.

Budyko, M.I., 1974, Climate and life. Academic Press, New York and
London.

Bryan, K., S. Manabe and R.L. Pacanowski, 1975, A global
ocean-atmosphere climate model. Part II The oceanographic circulation.
J.Phys. Oceanogr., 5, pp 30-46.

Cattle, H., 1986, (Editor) Tests of an ice model with leads and the
impact of ice boundary changes on the atmospheric circulation - a
poster presentation. Met. O 20 Internal Note 43.

Hibler, W.D. III, 1979, A dynamic-thermodynamic sea ice model.
J.Phys.Oceanogr., 9, pp 815-846.

Hibler, W.D. III, 1980, Modelling a variable thickness sea ice cover.
Mon. Wea. Rev., 108, pp 1943-1973.

Hibler, W.D. III, 1985, Sea ice models and remote sensing. Proceedings
of a conference on the use of satellite data in climate models,
Alpbach, Austria, 10-12 June 1985. European Space Agency, ESA SP-244,
pp 87-94.

Hibler, W.D. III and K. Bryan, 1984, Ocean circulation: its effect on
seasonal sea ice simulations. Science, 224, pp 489-492.

Manabe, S., K.Bryan, and M.J.Spelman, 1979, A global ocean-atmosphere
climate model with seasonal variation for future studies of climate
sensitivity. Dyn. Atmos. Ocean., 3, pp 393-426.

Maykut G.A., and N. Untersteiner, 1971, Some results from a
time-dependent thermodynamic model of sea ice. J.Geophys. Res., 27, pp
315-330.

Parkinson,C.L. and W.M. Washington, 1979, A large-scale numerical
model of sea ice. J.Geophys. Res., 84, pp 311-337.

Pollard, D., 1982, The performance of an upper ocean model coupled to
an interactive atmospheric general circulation model. Report No. 31,
Climatic Research Institute, Oregon State University, Corvallis.

Semtner, A.J. Jr., 1976, A model for the thermodynamic growth of sea
ice in numerical investigations of climate. J.Phys, Oceanogr., 6, pp
379-389.

Washington, W.M., A.J. Semtner, C.L. Parkinson and L. Morrison, 1976, On the development of a seasonal change sea ice model. J.Phys. Oceanogr., 6, pp 679-685.

Washington, W.M., A.J. Semtner Jr., G.A. Meehl, D.J. Knight and T.A. Mayer, A general circulation experiment with a coupled atmosphere-ocean-sea ice model. J. Phys Oceanogr., 10, pp 1887-1908.

WCP-26, 1982, Report of the WMO/CAS-JSC-CCCO meeting of experts on the role of sea ice in climatic variations (Geneva, 24-29 June 1982). ICSU/WMO.

****

Integration	Annual Mean Ice and Snow Depth (Year 50)			
	$F_B = 0.0$ Wm^{-2}		$F_B = 2.0$ Wm^{-2}	
Standard	2.30	(0.22)	1.36	(0.22)
Standard + 5LM Snow Row 1	2.59	(0.07)	1.99	(0.07)
Standard + 5LM Albedo	0.90	(0.05)		
5LM Forcing (Row 1) + Semtner Albedo	21.73[1]	(0.11)		
5LM Forcing (Row 1) + 5LM Albedo	13.04[1]	(10.48[1])		
5LM Forcing (Row 54) + 5LM Albedo	6.28[1]	(34.36[1])		

Table 10.I For explanation, see text Section 10.4.

PROCESSES CONTROLLING
SEA ICE

PROCESSES INFLUENCED
BY SEA ICE
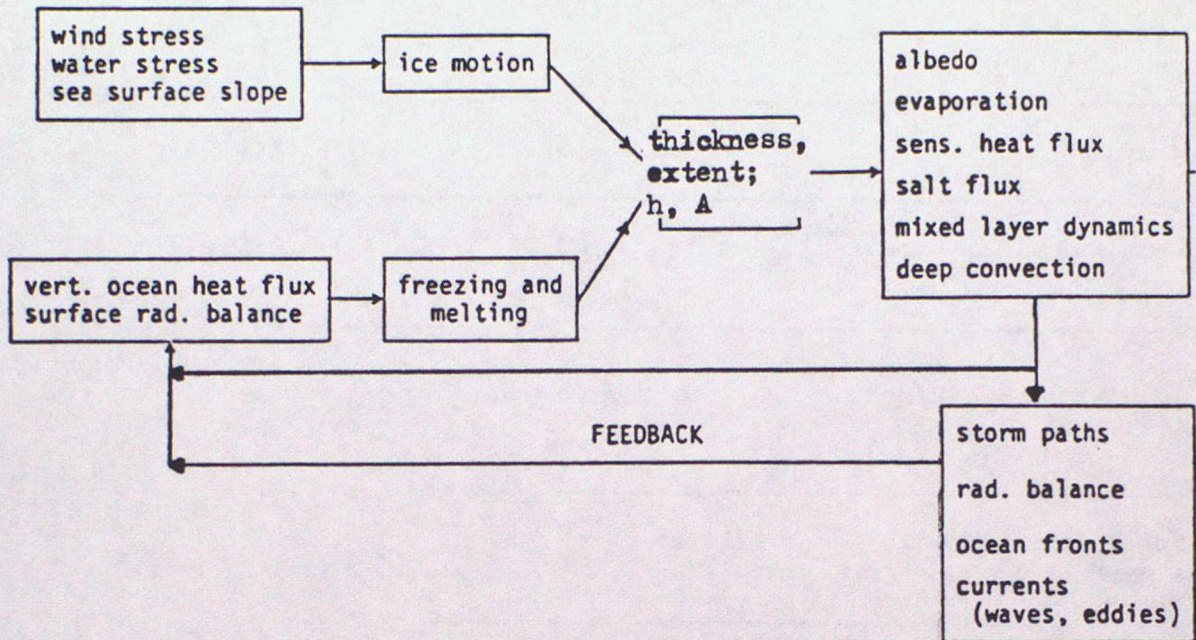
Figure 10.1 Schematic illustration of sea ice processes.
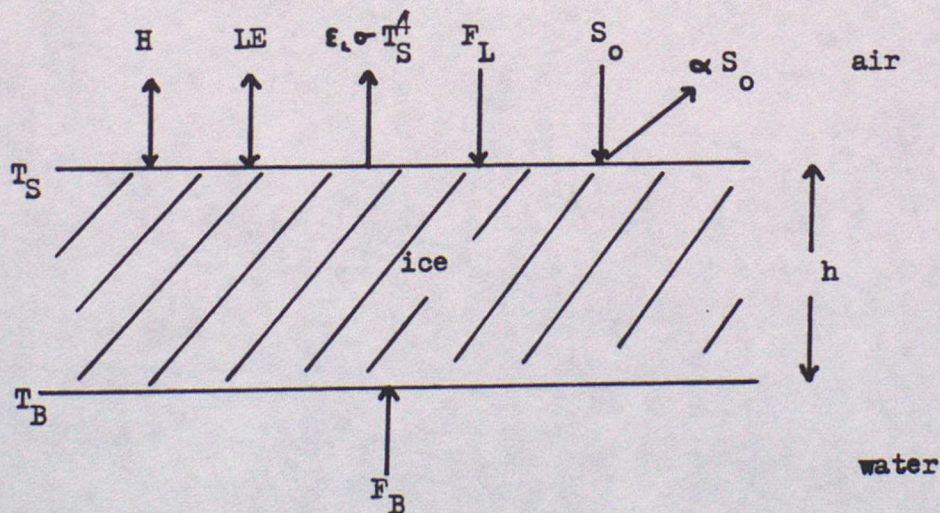
Figure 10.2 Schematic illustration of the sea ice representation in the Met O 20 AGCM.
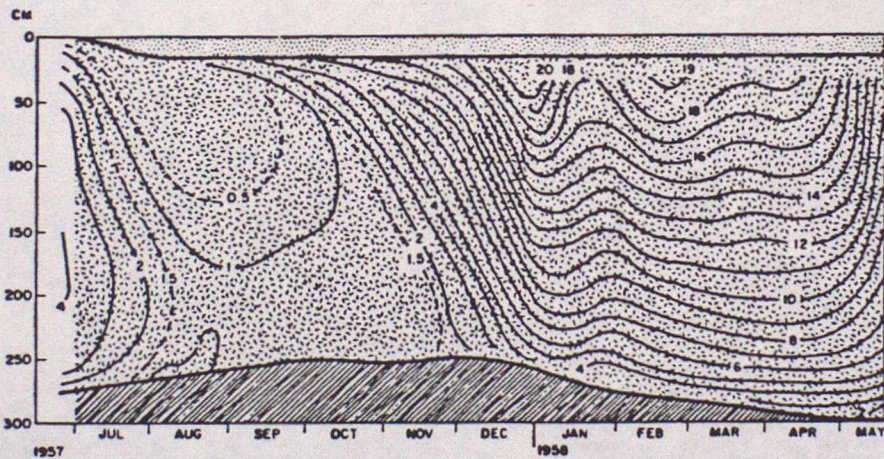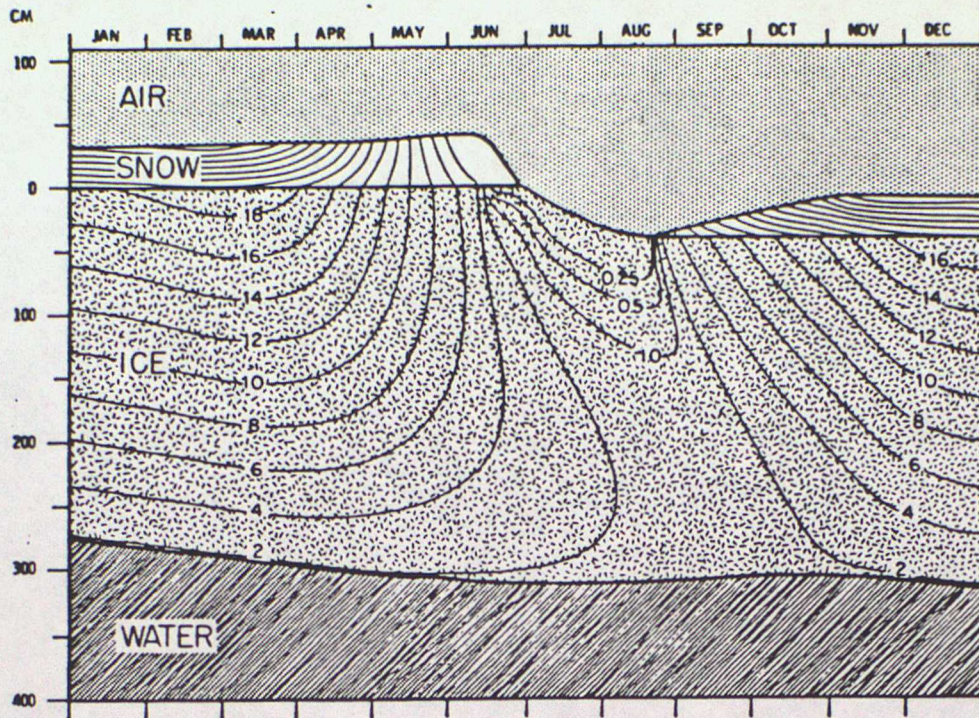
Figure 10.3 Predicted values of equilibrium temperature and thickness
for sea ice (above) and observed values below at IGY station alpha,
1957-1958.   Isotherms in the ice are labelled in negative degrees
Celsius; isotherms in the snow (unlabelled) are drawn at 2C intervals.
To distinguish between movements of the upper and lower boundaries,
they are drawn without regard to hydrostatic adjustment. The vertical
coordinate therefore corresponds to ice thickness only before the
onset of ice ablation at the upper surface (from Maykut and
Untersteiner, 1971).
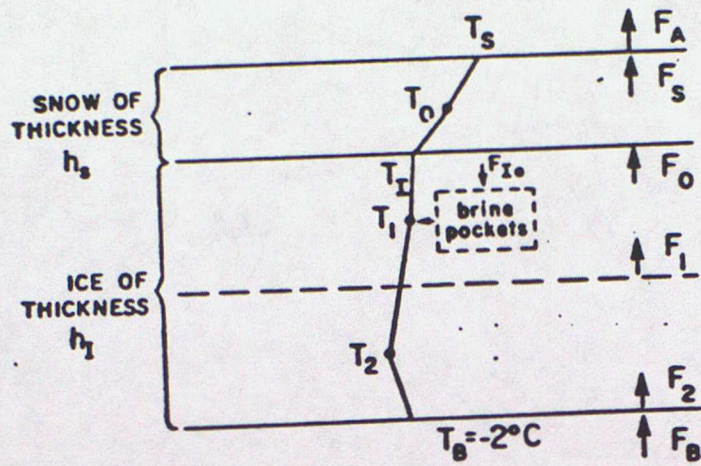
Figure 10.4 Schematic diagram of Semtner's (1976) 3-layer model.
Temperatures in the layers and thicknesses of the snow and ice are
predicted on the basis of fluxes across internal and external
boundaries. Energy of penetrating radiation is stored in brine pockets
and released during freezing (from Semtner, 1976).
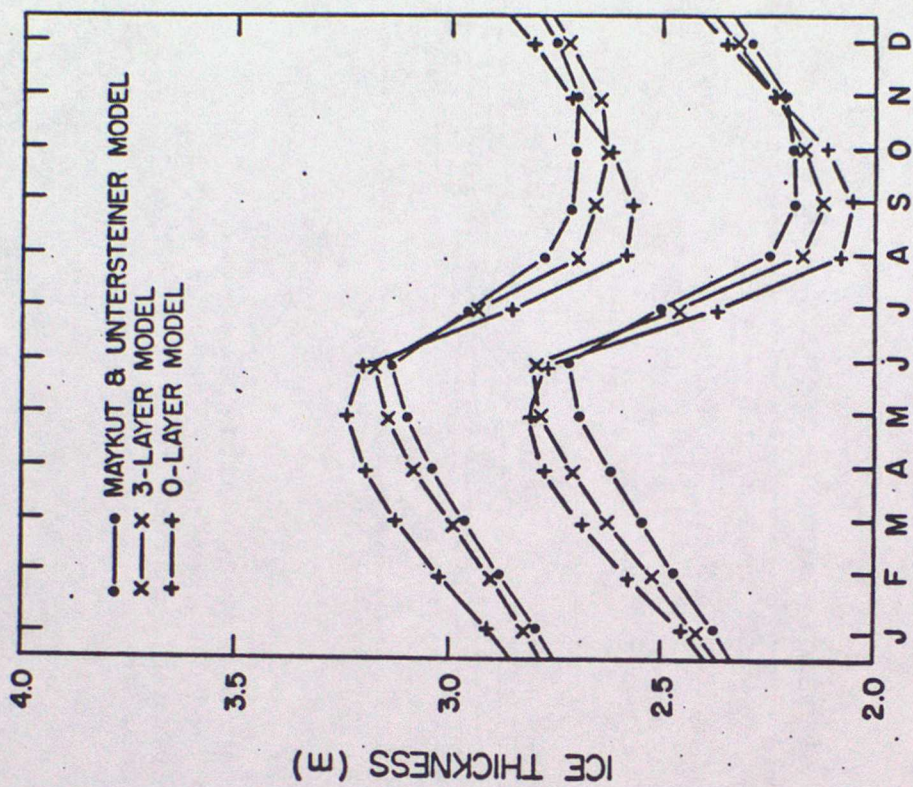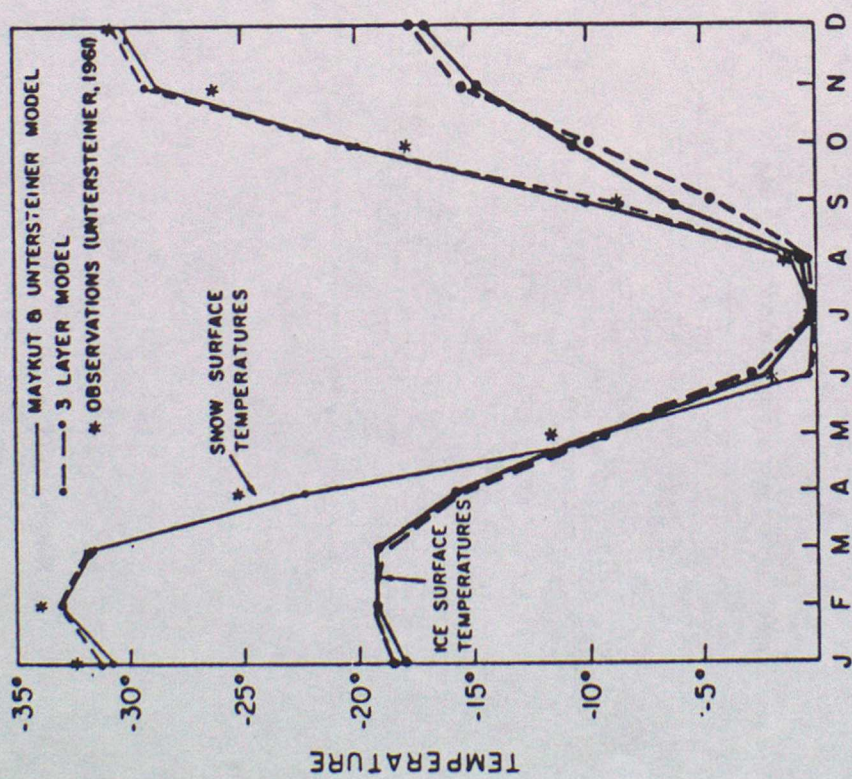
Figure 10.5 Comparison of the seasonal cycle of (a) the temperatures at the snow and ice surfaces and (b) the ice thickness, as predicted by the Maykut and Untersteiner (1971) and Semtner (1976) models for "standard" forcing. The upper set of curves of (b) are for the fraction of penetrating short wave radiation, I_0, =17% and the lower set for I_0 = 0% (from Semtner, 1976).

Figure 10.6 Computed and observed ocean surface temperature and sea
ice limits for January and July. Observed values are from Alexander and
Mobley (1976). Large stippled pattern represents extent of sea ice.
Sea ice thickness contours on computed maps are in metres (from
Washington et. al., 1980).
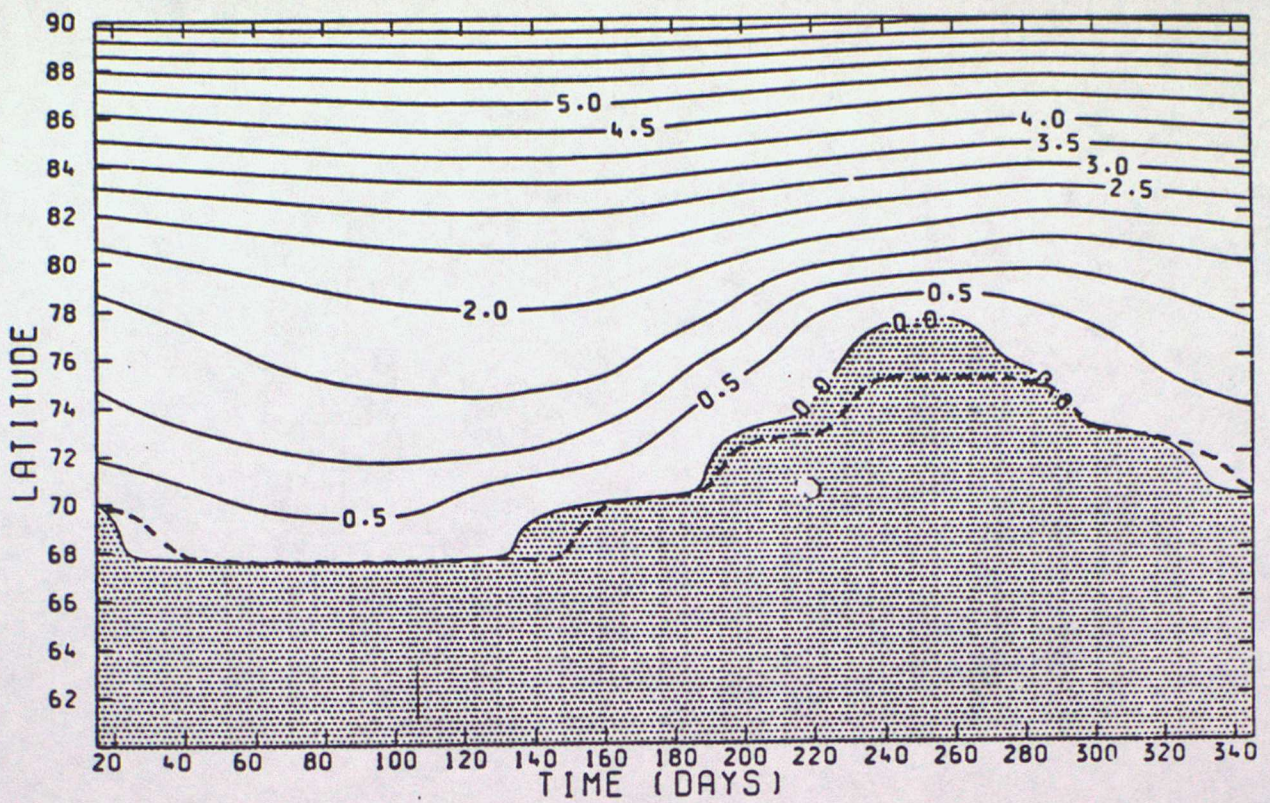
Ice thickness.   Contours are at 0.5 m intervals.
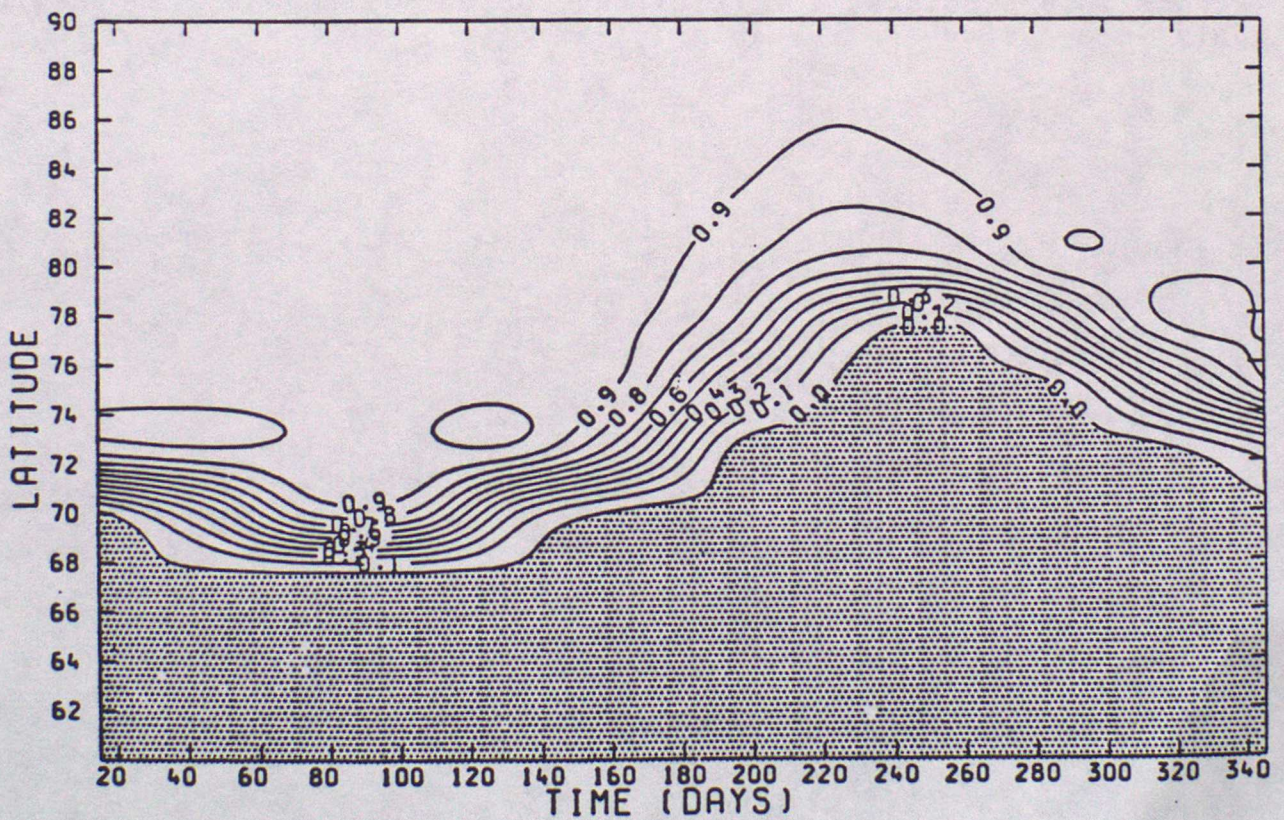
Ice compactness, A. Contours at intervals of 0.1.

Figure 10.7 Ice thickness and ice compactness from a model including a simple representation of leads due to Hibler (1979) (from Cattle, 1986).
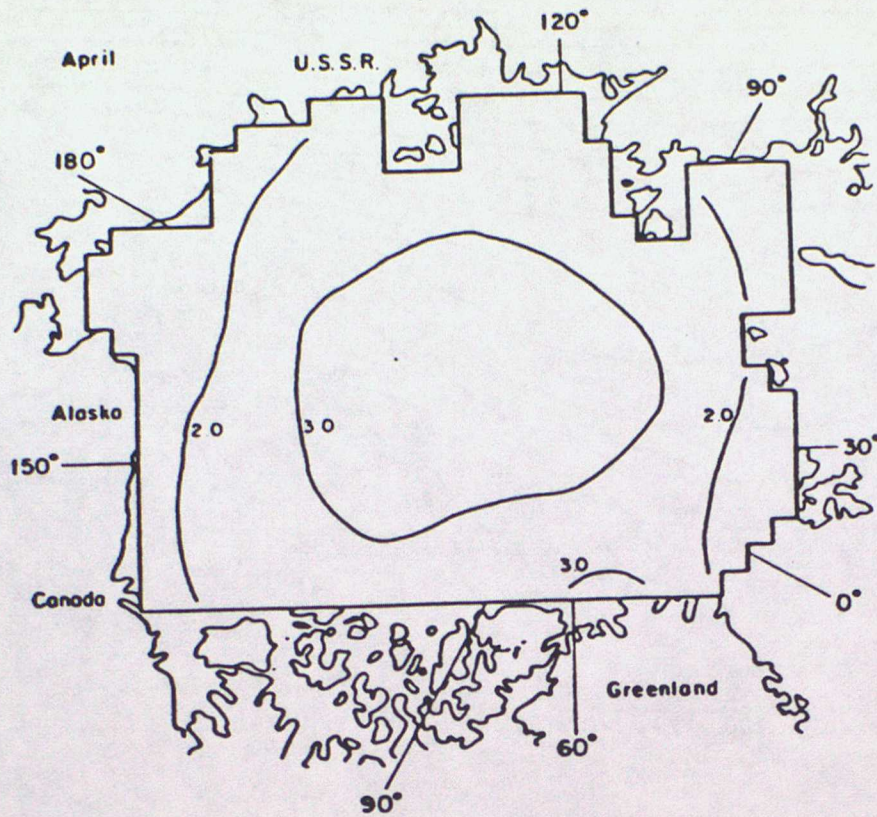
Figure 10.8 Simulated ice thickness contours from a thermodynamics only integration due to Hibler (1979).
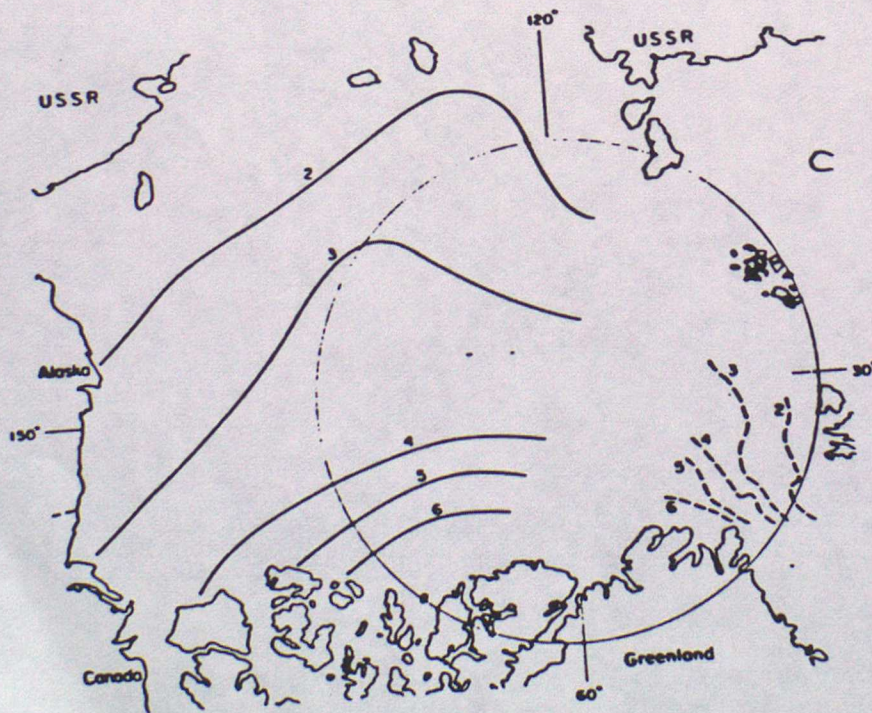

Figure 10.9 Observed ice thickness contours from submarine data. For details see Hibler (1979).
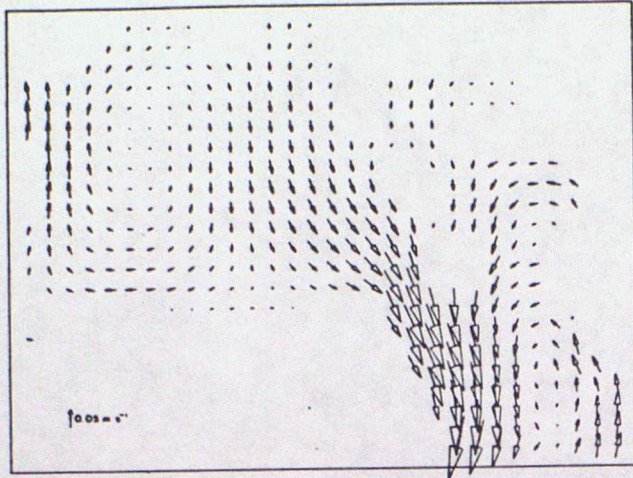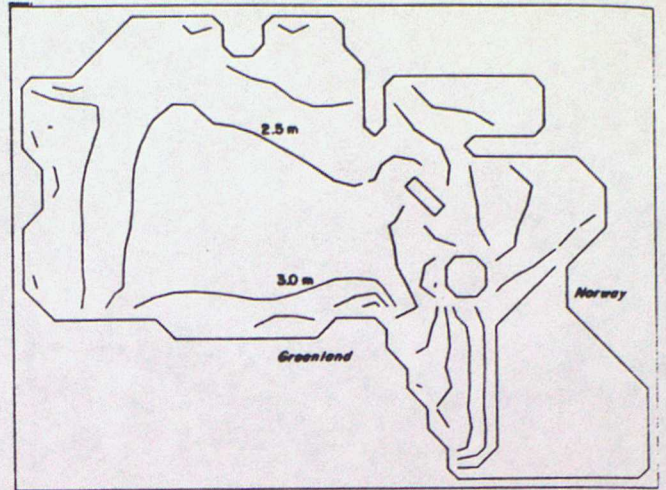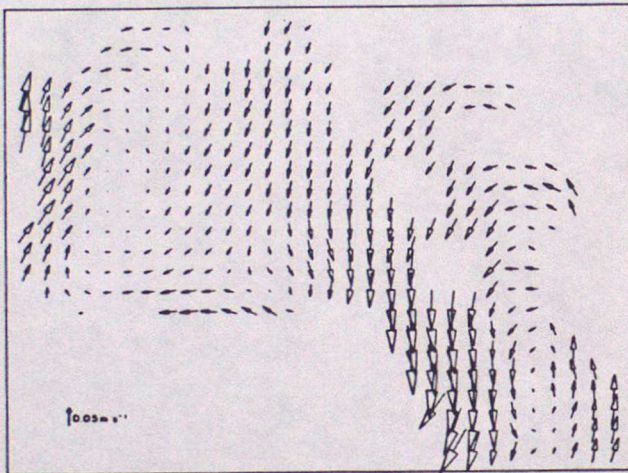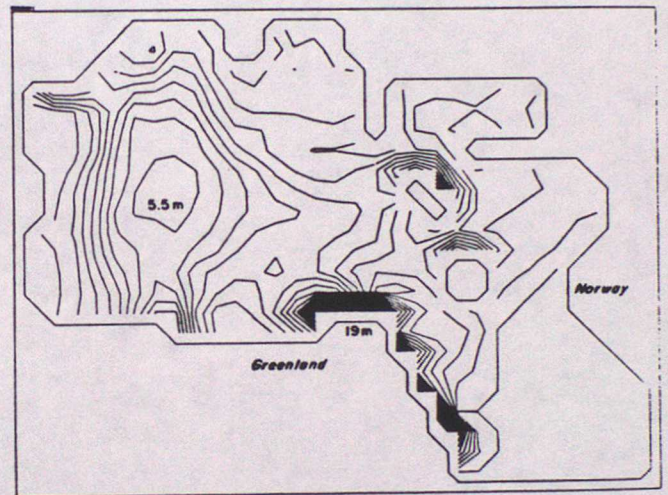
Figure 10.10 Simulated annual average ice velocities and ice thickness
for the end of December for a "plastic" ice rheology (a & b) versus a
free-drift model (c & d) (from Hibler, 1985).